NAGOYA INSTITUTE OF TECHNOLOGY

Doctoral thesis

# A Study of Statistical Characterization of Strength and Fatigue Lifetime for Silicon and Polysilicon Structures in MEMS

MEMS 構造材料としてのシリコンおよびポリシリコンを

対象とした強度と疲労寿命の統計的性質に関する研究

**VU LE HUY**

**2013**

# Abstract

Silicon and polysilicon are the most common structural materials for micro electro-mechanical systems (MEMS). Since the end of the last century, many evidences have been found that they are susceptible to fatigue. The strength of structures made of silicon has also been found to be strongly dependent on the fabrication process of structures such as etching. Designing MEMS with quantitatively evaluated long-term mechanical reliability is indeed one of the most important and urgent issues in order to push them through further development for future applications requiring higher levels of reliability. This thesis describes the development of evaluation and design scheme for the strength and fatigue lifetime of silicon and polysilicon materials in MEMS.

Firstly, from a statistical point of view, polysilicon thin films were examined whether their fatigue behavior can be formulated uniquely on the basis of initial defects which determine their strength distribution. The fatigue process determining the lifetime is modeled with the well-known Paris law as the fatigue crack extension process from the initial defects, whose equivalent crack lengths were evaluated from the initial strength distribution described by the Weibull distribution. The parameters in Paris' law were fit to the results of tensile fatigue tests with constant stress amplitudes performed on three groups of polysilicon thin film specimens patterned using different etching conditions leading to different etching damage. The results support a possibility that the fatigue behavior is independent of etching condition and that therefore the fatigue lifetimes can be practically predicted from their strength distributions by using the same values of the parameters in Paris' law.

The above theory was then extended to evaluate the strength distribution and fatigue behaviors of polysilicon thin film specimens patterned by etching into arbitrary shapes. The results show that the fracture and fatigue behaviors of the specimens can be described on the basis of local characteristics determined again by using the same set of parameters despite the different stress distribution. This means that the local characteristics of etching damage and the subsequent damage accumulation under fatigue loading were independent also of the shapes and the stress distributions. Therefore, the theory enables prediction for fracture strength and fatigue lifetime and thus designing silicon thin film structures.

For the case of very long fatigue lifetime, by the way, experiment may have to be stopped before failure when the number of cycles exceeds an affordable time limit. To overcome this hurdle, a new experimental method was proposed in order to estimate the fatigue behavior of polysilicon thin films by using cyclic loading with gradually increasing stress amplitude. The results show that the parameter values are the same as those obtained from the fatigue tests with constant stress amplitude, and that the new experimental method can be used to predict the fatigue lifetime in a more efficient manner.

Finally, a scheme for predicting the strength of thick structures patterned into arbitrary shapes by deep reactive ion etching of silicon wafer was also proposed. The scheme is based on the inhomogeneous defect distribution on the etched surfaces. Distributions of the fracture strength were described using two-parameter Weibull statistics, where the two parameters are defined as functions of the etching depth representing the inhomogeneity of the damage on the etched surface in the etching direction. The results showed that the fracture strength of arbitrarily-shaped structures can be predicted with statistical significance on the basis of the information obtained from a set of reference specimens, by taking into account the characteristics of etched surface, i.e., the inhomogeneous damage.

After accumulating these new findings, the fracture strength and fatigue lifetime of silicon structures in MEMS becomes predictable, and therefore they enable designing silicon MEMS structures with a specified level of mechanical reliability. This will help to save the time and expenses in the development of MEMS structures.

# Table of Contents

**Chapter I**

**Introduction ..... 1**

1.1. Background ..... 2

1.2. Overview of the thesis ..... 6

**Chapter II**

**Statistical Characterization of Fatigue Lifetime of Polysilicon Thin Films with Uniform Stress Distribution ..... 11**

2.1. Introduction ..... 12

2.2. Specimens and experiment ..... 12

2.3. Statistical analysis ..... 19

*2.3.1. Static strength test ..... 19*

*2.3.2. Fatigue test ..... 20*

2.4. Calculation and discussion ..... 27

*2.4.1. Estimation of optimum parameters in Paris' law ..... 27*

*2.4.2. Fatigue lifetime distribution ..... 33*

2.5. Conclusion ..... 38

**Chapter III**

**Estimation of Fracture Strength and Fatigue Lifetime of Arbitrarily-Shaped Polysilicon Thin Films ..... 39**

3.1. Introduction ..... 40

3.2. Statistical analysis ..... 41

*3.2.1. Static strength test ..... 41*

*3.2.2. Fatigue test ..... 43*

3.3. Evaluation of the strength and fatigue behaviors of specimens fabricated under the same conditions ..... 46

*3.3.1. Specimens and experiment ..... 46*

*3.3.2. Estimation of parameters ..... 51*

3.3.2.1. Static test ..... 51

3.3.2.2. Fatigue test ..... 52

*3.3.3. Discussion ..... 54*

3.4. Prediction of fatigue lifetime of specimens fabricated under different etching conditions ..... 60

*3.4.1. Specimens and experiment* ..... *60*
*3.4.2. Static strength evaluation* ..... *65*
*3.4.3. Fatigue lifetime prediction and discussion* ..... *67*
3.5. Conclusion ..... 70
**Chapter IV**
**A Novel Fatigue Test with Ramping Stress Amplitude to Evaluate Fatigue Behavior of Polysilicon Thin Films ..... 72**
4.1. Introduction ..... 73
4.2. Uniform stress distribution ..... 74
*4.2.1. Statistical analysis* ..... *74*
*4.2.2. Specimens and experiment* ..... *75*
*4.2.3. Results and discussion* ..... *76*
4.3. Arbitrary stress distribution ..... 80
*4.3.1. Statistical analysis* ..... *80*
*4.3.2. Specimens and experiment* ..... *81*
*4.3.3. Results and discussion* ..... *82*
4.4. Conclusion ..... 84
**Chapter V**
**A prediction Scheme of Static Fracture Strength of Thick Single-Crystal Silicon Structures Based on the Characterization of Damage Distribution on Processed Surface ..... 85**
5.1. Introduction ..... 86
5.2. Specimens ..... 87
5.3. Experiment ..... 89
5.4. Statistical analysis ..... 94
*5.4.1. Weibull analysis of the fracture strengths* ..... *94*
*5.4.2. Advanced method of strength prediction with inhomogeneous local strength* ..... *97*
5.5. Strength prediction and discussion ..... 98
5.6. Conclusion ..... 102
**Chapter VI**
**Conclusions ..... 104**
6.1. Summary of findings ..... 105
*6.1.1. Static strength* ..... *105*

*6.1.2. Fatigue behavior* ..... *105*
*6.1.3. General* ..... *106*
6.2. Applications ..... 107
*6.2.1. Strength and fatigue lifetime prediction* ..... *107*
*6.2.2. Designing MEMS structures* ..... *108*
6.3. Future works ..... 109
**Appendix 1**
**Fractographic Analysis for Polysilicon Thin Films ..... 111**
A1.1. Introduction ..... 112
A1.2. Overview of fracture site ..... 112
A1.3. Static fracture ..... 112
A1.4. Fatigue fracture ..... 115
A1.5. Conclusion ..... 118
**Appendix 2**
**EBIC Observation of Defect Growth Inside Silicon Under Fatigue Loading .... 119**
A2.1. Introduction ..... 120
A2.2. Specimen and experimental setup ..... 120
A2.3. Results and discussion ..... 123
A2.4. Conclusion ..... 124
**References ..... 126**
**Acknowledgements ..... 137**

# Chapter I

# Introduction

## 1.1. Background

Microelectromechanical systems (MEMS) are devices with highly miniaturized mechanical components fabricated using batch processing techniques inspired by integrated circuit (IC) technologies, which have been among the fastest growing technologies, opening new frontiers of microtechnology [1,2]. They have already been applied to various fields such as medical treatment and aerospace equipment where the reliability of MEMS structures is of serious concern. The mechanical reliability of MEMS has recently been attracting more and more interest.

Silicon is a popular structural material in MEMS. Silicon structures are commonly patterned into a broad variety of shapes by etching processes. It was reported that the damage induced by etching steps during fabrication of silicon structures determines the static strength [3,4] which is the maximum stress on the structures at the moment of fracture under monotonically increasing load. Their static strength distributions are well described using the two-parameter Weibull distribution [5,6,7-13]. On the other hand, silicon is typically brittle but was found to be susceptible to fatigue [7,14-17]. Many MEMS devices are often operated at high frequencies and relatively large stress levels, so that the fatigue lifetime of MEMS structures is a most serious concern for their long-term reliability. The mechanical properties of silicon such as its fracture strength and fatigue lifetime have been extensively reported [3-27]. Many studies surveyed the fracture and fatigue properties of silicon by using specimen shapes and loading configurations resulting in non-uniform stress distributions in the specimens [6,15,18,19,22-24,27]. However, stress distribution as well as damage distribution on the etched surfaces has not yet been included in the predictions of the strength and fatigue lifetime of silicon structures.

From the view point of engineering, fatigue lifetime prediction is important issue, but lifetime of silicon is at the moment hardly predictable. Lifetime prediction should stand on fatigue damage mechanisms of materials, and of course, the methods of prediction will be different corresponding to the viewpoint of the fatigue mechanisms. Up to now, the most commonly accepted model of fatigue process has been the reaction layer model [16,28,29], where the surface oxide layer is thickened with cyclic stress and subjected to corrosion cracking. Owing to the development of resonating structures to be used as specimens for fatigue tests at high frequencies

[15,28,30], a considerable amount of data was successfully accumulated. Most of them were operated with the stress ratio $R = -1$ [16,31-36], which is the ratio of minimum to maximum stress. Oxide layers as thick as several tens of nanometer were eventually observed on the test structures where oxidation may occur due to localized large stresses along the sidewalls [36]. This model was also supported by an evidence that fatigue lifetime was markedly extended in less humid environments [31-33]. However, this theory could not explain for the case of low-cycle fatigue [34,36], where the time was not enough for oxygen to diffuse into silicon. In contrast, however, it was also claimed that the thickening of a surface oxide layer due to cyclic stress was not observed until fatigue fracture on polysilicon devices with 3 nm thin native oxide [37] showing a counter evidence against the reaction layer model.

One advantage of resonating structures is that their resonating frequencies are sensitive to damage accumulation [14,16]. By monitoring the change in resonating frequency, it was found in an early study [14] that damage accumulation rate was insensitive to the applied stress level and thus the stress intensity factor at the tip of fatigue crack. The authors speculated that the fatigue process was controlled possibly by time dependent process such as oxygen diffusion. The influence of the testing frequency was also surveyed; it was recently reported that the fatigue lifetime in number of cycles increased when the frequency was increased from 4 kHz to 40 kHz [34]. However, for the case of the low frequency range, no distinct frequency effect on fatigue cycles from 50 Hz to 6000 Hz was observed [35].

Besides that, the effect of stress ratios other than $R = -1$ was also investigated [30,27,38]; it was commonly found that compressive stress accumulates the damage more efficiently. For example, the fatigue lifetime of polysilicon films tested under stress ratios ranging from –0.33 to –0.26 was much shorter than that under $R = 0$ [30]. It was recently observed that damage accumulation starts being considerable only after about $10^5$ to $10^6$ cycles during the fatigue tests with the stress ratio in a range from –0.5 to –0.4 [39], where the accumulation of damage was surveyed through the change of stiffness of the test structure which, of course, leads to the change in resonance frequency. Such a behavior was not observed in the previous studies [28,29,34] where the damage accumulation was observed through the change of resonance frequencies in the fatigue tests with the stress ratio $R = -1$. The experiment where no distinctive effect of frequency was found [35] as mentioned above was

performed with $R = 0$. These facts may also suggest that a time dependent reaction is not always dominant depending on the mechanical conditions [34]. A simple subcritical cracking model was also proposed to explain such results, where fatigue crack extends with wedging effects of asperities on the crack surfaces [27,38,40]. As briefly summarized above, the current state of discussion around the fatigue issues in silicon and polysilicon is still controversial despite many researchers' intensive efforts.

One possible explanation of fatigue which has not been considered among the recent arguments on fatigue mechanisms is dislocations. Dislocations may not be a candidate of fatigue failure mechanisms for glasses and untoughened ceramics which are expected to be immune to cyclic stress fatigue [41,42]. Plasticity of silicon was studied in the beginning of 1950s, and bulk silicon was reported to be ductile above the brittle-ductile transition temperature of about 700 °C [43-45]. In the past, dislocations were believed to emanate in silicon only at high temperature where they were observed in the bulk silicon material at temperature above the brittle-ductile transition temperature [45-58]. However, many recently reported results have suggested that dislocations would move even at room temperature especially in small scale structures [59-66]. For example, steps approximately 5 nm in height indicating dislocation slip lines were observed on the surface of 200 nm wide doubly supported beams made of single crystal silicon when bent with an atomic force microscope at 373 K [59]. Ductile behavior of nano-scale silicon at room temperature was also observed in other studies [60,61,66]. The fracture toughness of single crystal silicon films with 4 μm thickness was also reported to sharply increase above 70 °C from 1.3 to 2.5 $MPam^{1/2}$ [63]. In other words, the increase of fracture toughness of single crystal silicon films at room temperature corresponds to the decrease of specimen thickness. This suggested that the increase in the dislocation mobility is related to the thickness reduction [64]. Dislocations emitted from the fracture surface created at room temperature in 1-μm-thick specimen were also directly observed with a transmission electron microscope [64]. The change of fracture toughness of 1-μm-thick silicon film was observed recently to be between –20°C and –50°C [65]. These studies suggest that the behavior of silicon changed from brittle to ductile at room temperature might be because of the decrement of the specimen size. In other words, the brittle-ductile transition temperature decreases with the decrement of size-scale of silicon structures. Micro-scale silicon samples could be at the transition between

brittle and ductile properties, which would lead to an ambiguity in the fatigue mechanism of silicon.

Dislocations created at high temperature were deeply surveyed but they are something different from those may be created at far lower temperature. There are glide-set and shuffle-set dislocations known in silicon. At a temperature higher than the brittle-ductile transition (BDT) temperature, glide-set dislocations were always observed. At a lower temperature, however, shuffle-set dislocations would be activated [67]. Those at room temperature should be shuffle set which is far less surveyed and different from glide set which was far more deeply surveyed. In addition, it was recently calculated that the activation energy for shuffle-set dislocation emission could be considerably decreased even by 2 eV with compressive stress applied in addition to shear stress [67]. This fact may clearly explain the effect of compressive stress shortening the fatigue lifetime [30] as mentioned above. Since dislocations are observed in specimens with the dimensions from nano- to micrometer-scale under static load [59-66], they can be expected to also emanate in micro-scale specimens under cyclic load. Very recently, fatigue tests with monotonically increased stress amplitude, which is a novel fatigue test method developed in this thesis, were performed in inert nitrogen gas environment and they showed that silicon thin film specimens were fractured at the stress level smaller than their static strength [68]. It was suggested that fatigue damage was introduced by repeated loading even under an inert environment, and that fatigue was induced by dislocation activities. This conclusion is supported by observations of dislocations generated by fatigue at room temperature in silicon [69].

When dislocations are considered as the source of damage accumulation during fatigue cycles in micro-scale silicon, it is naturally expected that the process can be modeled with the well-known Paris law which controls a fatigue crack extension law commonly applied to metallic materials [70-73]. The fatigue lifetime of silicon under different stress levels was already reported to follow the trend expected from Paris' law [74]. In addition, silicon MEMS structures are usually patterned by etching processes, whereupon damage is introduced into the material, considerably reducing the initial strength even before cyclic stress is applied. The fatigue lifetime is then understood as the time it takes for the equivalent initial cracks, which determine the strength under the static stress, to extend to the critical length under the cyclic

applied stress. From this point of view, the fatigue lifetime distribution of polysilicon thin films was surveyed recently [75] in correlation to their static strength distribution by formulating the equivalent crack extension process to be controlled by Paris' law. However, this survey was performed with only one group of specimens. Due to a large scatter observed in both the static strength and fatigue lifetime, however, a further careful study was needed to determine whether the fatigue lifetime can be commonly described by Paris' law with a unique set of parameters inherent to the material when exposed to a given environment.

Furthermore, in industry, because of the mentioned characteristics, the fracture strength as well as fatigue lifetime must receive particular attention starting from the designing process in order to ensure the reliability of fabricated structures. However, since shapes and scales of MEMS structures are so diverse [1], it can be prohibitively costly and time-consuming to perform tests with all the different structures. Therefore, it seems preferable to establish a method to predict the fracture strength and fatigue lifetime of silicon structures in advance, before the actual fabrication of structures and without performing additional experiments for each new structure type.

## 1.2. Overview of the thesis

By considering the current situation of researches stated above, the goal of this study was set on the statistical characterization of the strength and fatigue lifetime for silicon and polysilicon structures in MEMS. This would supply fundamental knowledge to apply in design of MEMS structures. This thesis is constructed with 6 chapters and two appendices as follows:

**Chapter 1: Introduction**

This chapter describes the background and the overview of the thesis.

**Chapter 2: Statistical characterization of fatigue lifetime of polysilicon thin films with uniform stress distribution**

From a statistical point of view, polysilicon thin films were examined in this chapter whether their fatigue behavior can be formulated uniquely on the basis of initial defects which determine their strength distribution. This was not able to be

statistically confirmed with only one group of specimens obtained in the previous study [75]. The fatigue process determining the lifetime is modeled with the well-known Paris law as the fatigue crack extension process from the initial defects whose equivalent crack lengths were evaluated from the initial strength distribution. The parameters in the Paris' law were here fit to the results of tensile fatigue tests performed on three groups of specimens patterned using three different conditions leading to different etching damage. The results showed that the calculated behaviors using the same values of the parameters described well the distributions of the experimental data in spite of the difference of initial strength levels. They support a possibility that the fatigue fracture is caused by the accumulation of defects and that therefore the fatigue lifetimes can be practically predicted from their strength distributions by using the same values of the parameters in Paris' law.

**Chapter 3: Estimation of fracture strength and fatigue lifetime of arbitrarily-shaped polysilicon thin films**

The theory of statistical characterization in Chapter II is extended in this chapter for the silicon structures with arbitrary stress distributions. It is applied to evaluate strength distribution and fatigue behavior of polycrystalline silicon thin film specimens patterned into arbitrary shapes by etching. The static strength distribution of specimens is described by a two-parameter Weibull distribution applied to local points along the etched surface. The fatigue lifetime is formulated by applying Paris' law in the same way as a crack extension process presented in Chapter II, but for every local portions along the etched surfaces of the specimens. The parameters in the Weibull distribution and in Paris' law were fit to the results of tensile static strength and fatigue tests performed on the specimens with different shapes fabricated under not only the same conditions but also the different conditions. Parameter distribution ranges were analyzed to see how they are close to each other. The results show that the fracture and fatigue behaviors of the specimens can be described by using a unique set of parameters despite the different stress distribution. This means that the local characteristics of etching damage and subsequent damage accumulation under fatigue loading was independent of the stress distributions and thus of the shapes of specimens.

**Chapter 4: A novel fatigue test with ramping stress amplitude to evaluate fatigue**

**behavior of polysilicon thin films**

This chapter presents a new experimental method to estimate the fatigue behavior of polysilicon thin films by using cyclic loading with gradually increasing stress amplitude, which is here called ramping fatigue test. This method solves fundamental problems of conventional fatigue experiments with constant amplitude, which is here called normal fatigue test. Because of a large scatter in strength, it was difficult to evaluate fatigue behavior with the normal fatigue test when specimens broke before reaching the target stress amplitude. Furthermore, experiment may have to be stopped before failure when the number of cycles exceeds an affordable time limit. In the ramping fatigue test, the small stress amplitude in the beginning gives fatigue degradation of strength and the large stress at the final stage breaks all the specimens. The fatigue crack extension process determining fatigue lifetime was estimated by the well-known Paris law with two unknown parameters. These were fit to the results of two methods performed on specimens with two different situations of etching damage. It is shown that the new experimental method can be used to predict the fatigue lifetime in a more efficient manner.

**Chapter 5: A prediction scheme of static fracture strength of thick single-crystal silicon structures based on the characterization of damage distribution on processed surface**

Since bulk micromachining creates thicker structures than those thin film structures discussed up to the previous chapters, this chapter presents a scheme for predicting the strength of thick silicon structures patterned into arbitrary shapes by deep reactive ion etching. In this etching progress, distribution of the defects induced on the etched surfaces was not homogeneous in the direction perpendicular to the wafer surface and led to the change of local strength. Therefore, the scheme is based on the inhomogeneous defect distribution on the etched surfaces. Single-crystal silicon specimens with different shapes were subjected to four-point bending tests with monotonically increasing load. Distributions of the fracture strength were described using two-parameter Weibull statistics, where the two parameters are defined as functions of the etching depth. In order to estimate the distribution of the local strength determined by the damage, the etched surfaces of specimens without notch were tested in three different bending directions corresponding to three different

weight functions of the applied stress. The estimated values of the parameters were used to predict the fracture strength of four types of notched specimens with different notch tip radii. The results of comparison between the distributions of predicted strengths and experimental data showed that the fracture strength of arbitrarily shaped structures was predictable with statistical significance on the basis of the information obtained from specimens without notch, by taking into account the characteristics of etched surface, i.e., the inhomogeneous damage.

**Chapter 6: Conclusions**

This chapter summarizes all the results, conclusions and application scheme for engineering in the thesis.

**Appendix 1: Fractographic analysis for polysilicon thin films**

This appendix presents a fractographic study for the initial cracks and fatigue crack extension process in zero-tension cyclic stress test of polysilicon film specimens with notches. The initial cracks and their fatigue extension were speculated on the fracture surfaces observed in a scanning electron microscope. The fatigue crack extension process was quantitatively analyzed in detail using Paris' law on the basis of the parameters evaluated from static and fatigue test data. The observed and estimated crack lengths were compared to each other. The results suggest that the fatigue crack extend into the silicon itself but not in oxide layer. Therefore, they support the theory of lifetime estimation with Paris' law in this thesis.

**Appendix 2: EBIC observation of defect growth inside silicon under fatigue loading**

In order to support the theory on evaluation of fatigue lifetime estimated in this thesis, which was on the basis of Paris' law, this appendix presents the prelimilary results of a trial to observe the defect growth inside silicon under fatigue loading. Fatigue test was performed on single crystal silicon in an environmental scanning electron microscope. While the specimen was repeatedly subjected to compressive stress, electron beam induced current (EBIC) images were obtained to visualize damage evolution. The changes were successfully observed at the notch tip, which remained the same through the hydrofluoric acid treatment after the experiment. These facts suggest that damage evolved inside silicon crystal during the fatigue

loading process and that the contrast change was not due to an oxide layer thickened on the surface.

# Chapter II

# Statistical Characterization of Fatigue Lifetime of Polysilicon Thin Films with Uniform Stress Distribution

## 2.1. Introduction

According to the background stated in Chapter I, statistical characteristics of polysilicon thin films were newly surveyed in this chapter with the data of fatigue tests in addition to those already presented previously [75]. The experimental data were obtained from three groups of polysilicon specimens where those from two groups had been obtained in a previous study [76] and those from a third group were newly obtained here. The three groups had experienced different etching conditions and therefore had different strength levels. On the basis of the experimental results of a total of three different specimen groups, the distributions and confidence ranges of the parameters of Paris' law are examined. To perform these calculations, two parameter estimation methods are compared. One is the least squares method (LSM) minimizing the sum of squared deviations between the experimental lifetime observation and the lifetime distribution calculated using estimated parameters. This is the same method as was utilized in the previous studies [75,76]. The second method is the maximum likelihood method (MLM) in which the chi-square distribution helps to evaluate the confidence intervals of estimated parameters [77-79].

After clarifying the statistical characteristics of the parameters, practical differences in fatigue lifetime estimated with different sets of the parameters are investigated. The aim of this chapter is to demonstrate the applicability of Paris' law and to find statistically whether there is a unique set of the parameters controlling the fatigue process, which would then suggest accumulation of defects from the initial surface damage. As a consequence, the fatigue lifetime of polysilicon thin film structures fabricated under different etching conditions could then be predicted on the basis of their strength distributions alone by applying parameters inherent to the material and appropriate for the used conditions under which the structure is operated.

## 2.2. Specimens and experiment

The tensile test structure [80] shown in Fig. 2.1 was utilized for the experiment. It consists of a stationary outer frame and a movable inner frame connected by parallel springs. They were fabricated out of single-crystal silicon wafers. The springs are oriented along a <110> crystal direction. Each spring is

designed to have a width and length of 100 µm and 2000 µm, respectively. The outer and inner frames are separated by gaps of 400 µm and bridged by four specimens. Specimens were loaded when the inner frame was pushed by an actuator, as shown in Fig. 2.1.

Figure 2.2 illustrates briefly the fabrication process of the test structures. Specimens on the structures were made of a polysilicon thin film, which was deposited on silicon wafers by low-pressure chemical vapor deposition at a temperature of 625°C and then annealed at 1050°C for 1 hour. The film was patterned into the specimens after the annealing and the wafer was through-etched from the rear to produce the gaps. The details of the fabrication process have been reported in the referred paper [80].

Three groups of polysilicon thin film specimens were named Groups A, B and C with different strength levels due to different etching conditions: the specimens of Group A were etched by a reactive ion etching (RIE) process, while specimens of Groups B and C were structured using the same Bosch process for the deep reactive ion etching of silicon. The recipes of these etching processes are shown in Table 2.1. Groups B and C were fabricated at different times. Therefore the etching conditions were not exactly identical even though the same etching recipe was applied. As a consequence the strength levels of Groups B and C appeared as slightly different, as discussed below. The former two groups were tested in previous studies [75,76], while the experiment on the last group was newly performed in this study. All the specimens

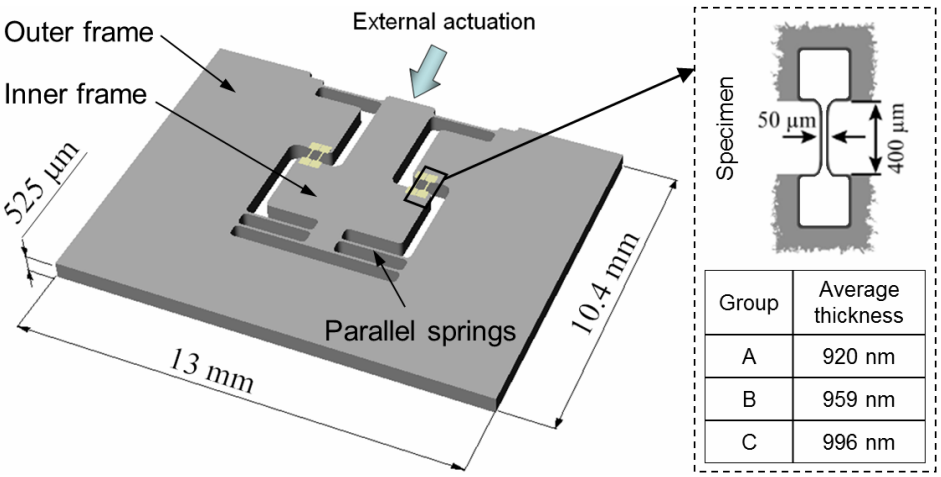


**Fig. 2.1** The test structure and specimens.

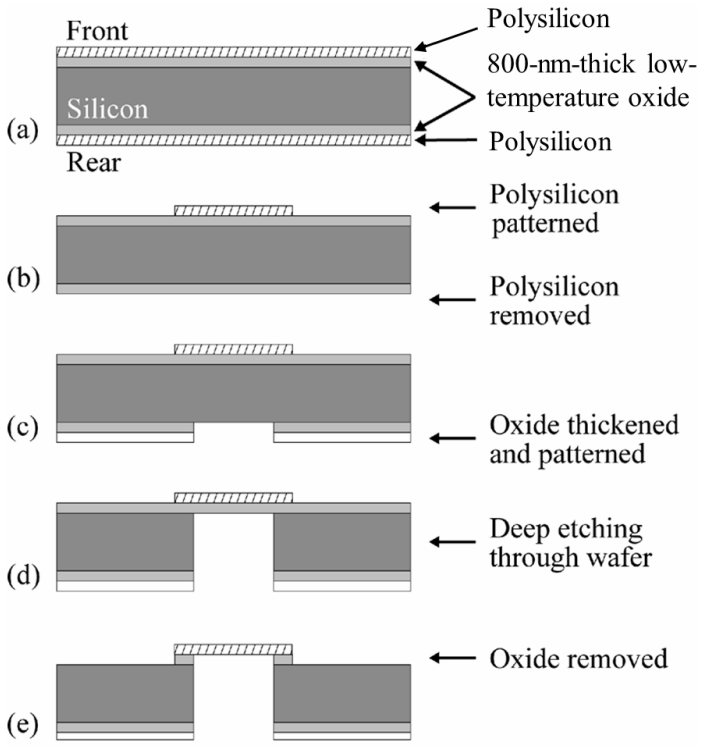


**Fig. 2.2** Fabrication process of test structure. (a) Deposition of oxide and polysilicon, and subsequent annealing; (b) polysilicon patterning on the front and removal from the rear; (c) deposition of thick oxide layer and patterning of oxide layers on the rear; (d) Silicon deep etching by Bosch process; (f) Buffered hydrofluoric acid etching.

here are designed to have the same parallel-sided shape shown in Fig. 2.1. Figure 2.3 shows the scanning electron microscope (SEM) pictures of a specimen used in the experiment and the micro texture of the polysilicon film taken from a specimen of Group C. Specimens are flat thin films with a width of 50 μm and a length of 400 μm. The average thicknesses of specimens in Groups A, B and C were 920 nm, 959 nm and 996 nm, respectively. The grain size of the films was observed to be in a range from 70 nm to 300 nm. The average roughness, i.e., the average height of the bumps on a surface, of the etching surfaces of the specimens of Groups A, B and C were measured to be about 130 nm, 60 nm and 90 nm, respectively. Figure 2 shows a scanning electron micrograph of the micro texture of the polysilicon film. The valleys on the etched surface act like mirco notches and should be the cause for fracture as etching damages. Since the specimens were long enough in the tensile stress direction and were designed with a stress concentration factor of 1.01, the stress field where the specimens were expected to break was assumed as uniform.

Figure 2.4 shows the entire and close-up view of the experimental setup. The test structure was maintained by a holder and actuated by a piezo-positioner (PI P-841.20, travel: 30 μm, resolution: 0.6 nm). The applied load was recorded by the load cell mounted on the tip of the actuator. The load cell used for the tests of specimens of Groups A and B had been of the type Kistler 9215 (resolution: 1 mN, sensitivity: 81 pC/N, maximum capacity: 200 N, stiffness: 140 N/μm). For Group C, it was the cell PCB Piezotronics 209C2 (resolution: 0.09 mN, average sensitivity: 538.9 mV/N, maximum capacity: 48.9 N, stiffness: 350 N/μm). A laser displacement sensor (Anritsu, KL1300B, resolution: 5 nm, sampling frequency: 64 kHz) was placed on the

**Table 2.1.** Recipes of etching process used to fabricate the specimens

| Parameters | | RIE process | Bosch process |
|---|---|---|---|
| Process pressure [mTorr] | | 5 | 5 |
| Etching | $SF_6$ [sccm] | 130 | 130 |
| | $O_2$ [sccm] | 20 | 13 |
| | ICP power [W] | 650 | 600 |
| | RIE power [W] | 16 | 12 |
| | Time [s] | 60 | 9 |
| Passivation | $C_4F_8$ [sccm] | - | 85 |
| | ICP power [W] | - | 600 |
| | RIE power [W] | - | 0.2 |
| | Time [s] | - | 6 |
| Etching rate [μm/min] | | 2 | 2 |
| Number of cycles | | - | 3 |

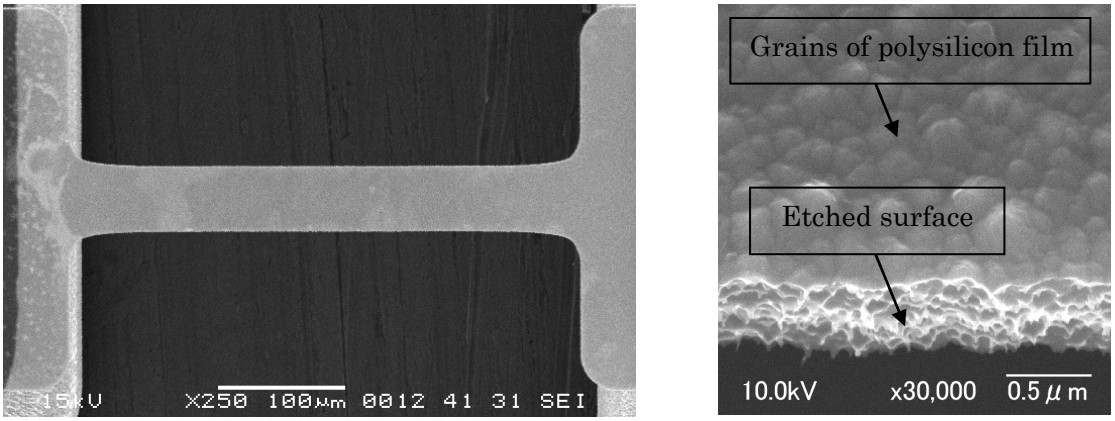


(a) (b)

**Fig. 2.3** SEM pictures of (a) a specimen used in the experiment and (b) a micro texture of the polysilicon film of Group C specimens.

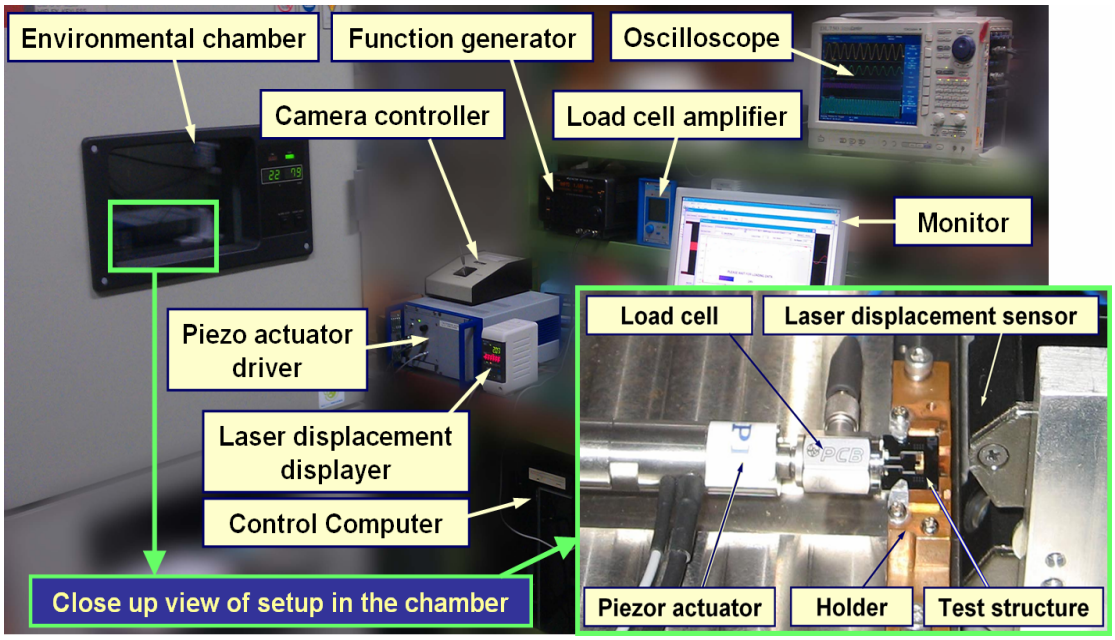


**Fig. 2.4** Experimental setup.

opposite side of the test structure to measure the displacement of the inner frame at its bottom edge. This setup was located in an environmental chamber (ETAC TH441HA) with temperature and humidity controlled within ±0.1°C and ±1%, respectively. All the equipment was driven from outside the chamber by a computer-controlled system which also logged all the data.

The static strength tests were performed with monotonically increasing load under lab-air conditions. Figure 2.5 shows an example of the load-displacement behavior of a static test, where the load drops correspond to the load applied to the specimens just before fracture. The static strength of a specimen was evaluated by dividing the applied load by the cross-sectional area of the specimen. If two or three specimens break at the same time, the load applied to one specimen was calculated by dividing the load drop by the number of these specimens. When two specimens break simultaneously in fatigue test, it is ambiguous whether the fracture of the second specimen occurred due to fatigue by coincidence at exactly the same number of cycle or simply due to overloading to the surviving specimens caused by the loss of a specimen. However, the frequency of this situation was around 10% in static test and was not observed in the fatigues test. With the high stiffness load cells used in this study, the uncertainly in the determination of the actual load applied to the specimens when fractured simultaneously was about 0.1%. It was therefore small enough to be ignored. A more detailed discussion of this situation can be found in previous papers [75,80].

The fatigue experiments were performed at 22°C and 80% of relative humidity.

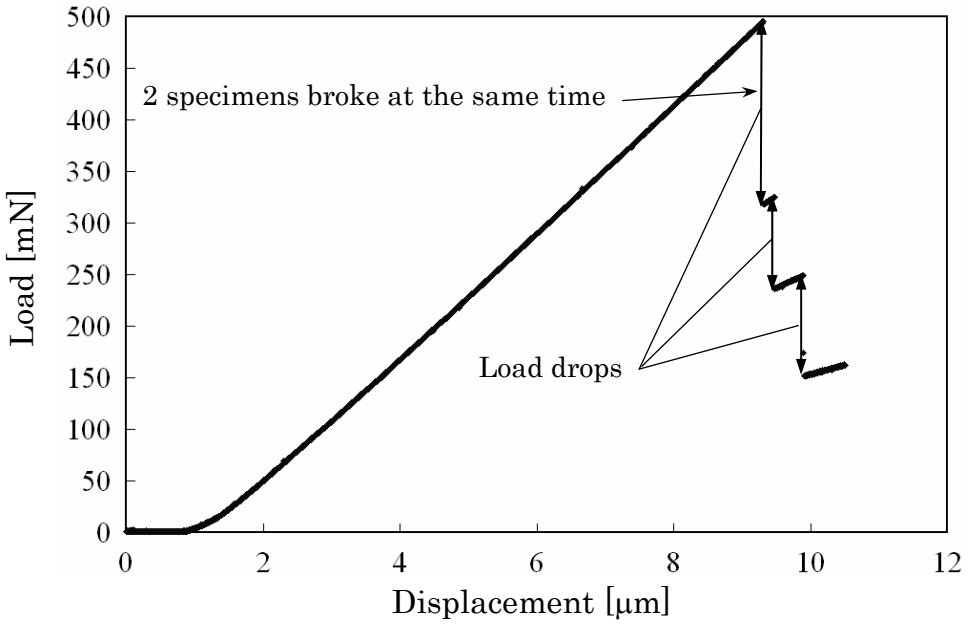


**Fig. 2.5** Load-displacement behavior in a static strength test.

This was to accelerate the experiments, knowing that fatigue lifetime of silicon is markedly shortened by humidity in the atmosphere [31,32,34,36,81] although the responsible mechanism has not yet been directly clarified, as discussed in the Introduction. All the specimens were cyclically loaded between a common minimum of zero and maximum stress levels varied on purpose from test chip to test chip. The common minimum implies that the stress ratio was zero for all the specimens. Figure 2.6 shows a typical load record applied to a structure in the fatigue tests, where the load drop corresponds to the amplitude of the load applied to one specimen. The applied stress amplitude was calculated by dividing the load drop by the cross-sectional area of the specimen. Specimens of Groups A, B and C were loaded with different frequencies of 100, 250 and 500 Hz, respectively. Because the effect of frequency on fatigue behavior was reported to be unmarked within the range from 50 to 6000 Hz [35], the frequency of the tests in this study was increased with the aim to speed up the experiments and thus increasing the number of data points. The effect is discussed in Section 2.4.2 based on the actual data. The number of fatigue test data of Groups A, B and C is 10, 22 and 37, respectively.

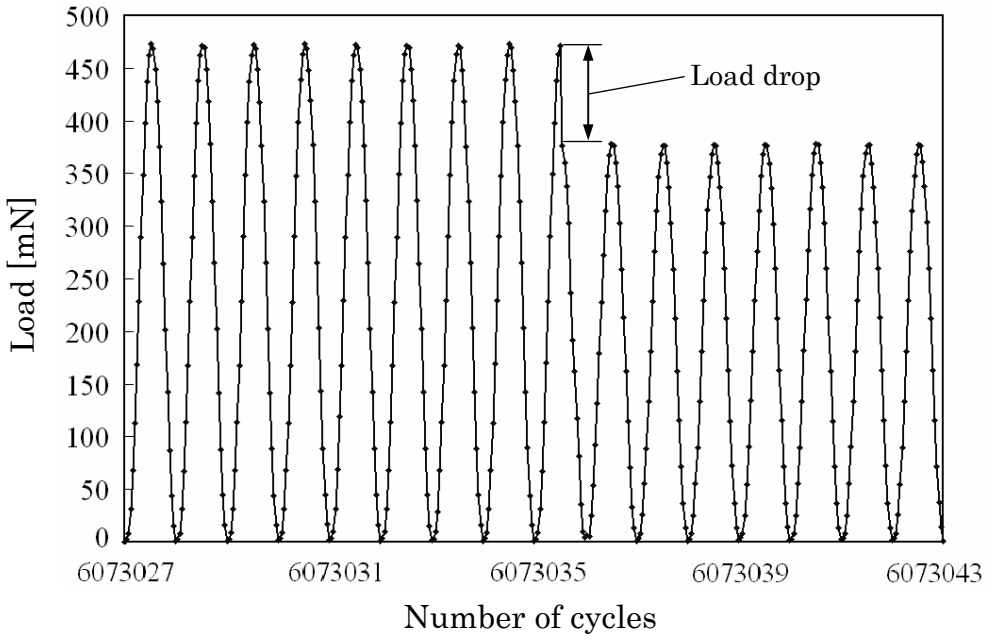


**Fig. 2.6** Load drop observed when a specimen broke on a test structure in a fatigue test.

## 2.3. Statistical analysis

### *2.3.1. Static strength test*

It is known that the strength of brittle materials such as silicon shows large scatters, which is well described using the Weibull distribution [7,8,82,83]. In the two-parameter Weibull distribution [8], the cumulative fracture probability $F$ of the specimens is defined as

$$F = 1 - \exp\left[ -\left( \frac{\sigma}{\sigma_0} \right)^m \right], \tag{2.1}$$

where $m$, $\sigma_0$ and $\sigma$ denote the Weibull modulus, the scale parameter and the fracture stress, respectively. The Weibull modulus, also termed shape parameter, represents the data scatter, while $\sigma_0$ is related to the average strength.

On the other hand, the cumulative fracture probability $F$ of experimental data was evaluated by the mean rank method as

$$F = \frac{i}{I+1}, \tag{2.2}$$

where $i$ is the number of a specimen among its group ranked by fracture stress and $I$ is the total number of tested specimens of the group. Static test data were ranked here from the weakest to the strongest sample in each group.

Symbols in Fig. 2.7 show the static strength test results of the three groups, where the abscissa and ordinate indicate the fracture stress $\sigma$ and the cumulative fracture probability $F$, respectively. Optimum values of the parameters $\sigma_0$ and $m$ were obtained by applying the LSM minimizing the sum of $\Delta F_i^2$, where $\Delta F_i$ denotes the deviation between the cumulative fracture probabilities from experiment and model. Thus, the optimum values of $\sigma_0$ and $m$ listed in Table 2.2 for each group of specimens were obtained. The curvilinear lines in Fig. 2.7 indicate the results of fitting. Figure 2.7 clearly shows the different levels of static strength of the three groups depending on their state of damage due to the different etching processes. As has been suggested, the static strength of thin film MEMS structures under monotonically increasing load may be completely determined by the initial damage induced by the fabrication process, especially the damage on the side walls due to the etching process to pattern

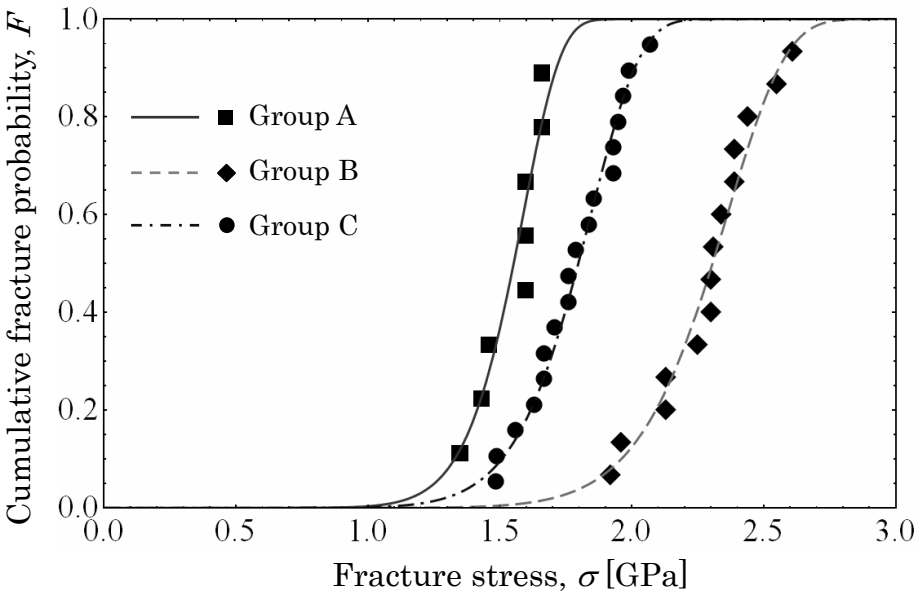


**Fig. 2.7** Static strength test results. The solid symbols show the experimental data and the curvilinear lines show the fit of Weibull distribution.

**Table 2.2.** The optimum values of $\sigma_0$ and $m$

| Parameters | Group A | Group B | Group C |
|---|---|---|---|
| $\sigma_0$ [GPa] | 1.60±0.05 | 2.38±0.06 | 1.86±0.04 |
| $m$ | 12.1±3.9 | 11.6±2.8 | 10.7±2.3 |

the films; the static strength is thus quite sensitive to the etching conditions in the fabrication process [3-5,18,21,83].

### *2.3.2. Fatigue test*

The raw fatigue test data distributions of three groups of specimens are shown in Fig. 2.8 with different symbols for the three specimen groups. Each symbol shows the applied stress amplitude and fatigue lifetime in terms of cycles of a specimen. There were 6 specimens fractured at the first cycle during the first increment of applied stress before the intended stress amplitude value was reached. In this case, the fracture event corresponds to the static fracture test. However, the data obtained from

these specimens did not fully reflect the static strength distribution, because the applied load level was limited within the range of the stress amplitude applied in the fatigue test. Therefore, they were excluded from the analysis. Since the static strength distribution was already obtained by static tests and fully characterized by the parameters $m$ and $\sigma_0$, this exclusion does not bias any statistical properties. The dashed lines show the regions within which the tested data of the groups lie. They help to distinguish the experimental data distributions of the groups.

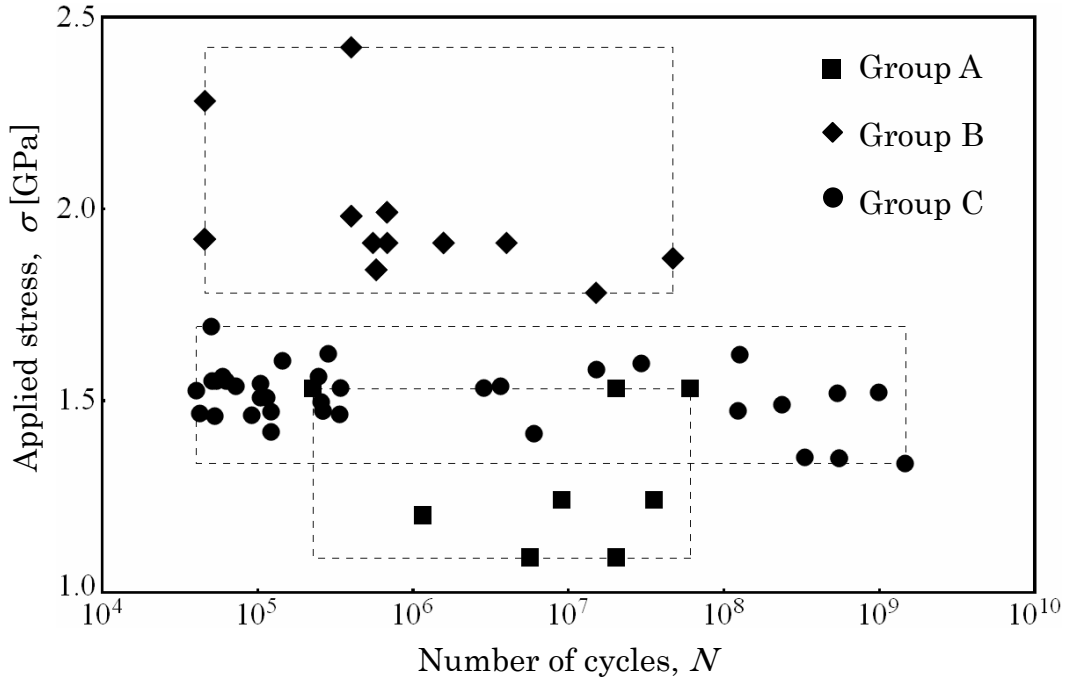


**Fig. 2.8** Raw data distribution of fatigue tests performed at 22°C and 80%RH.

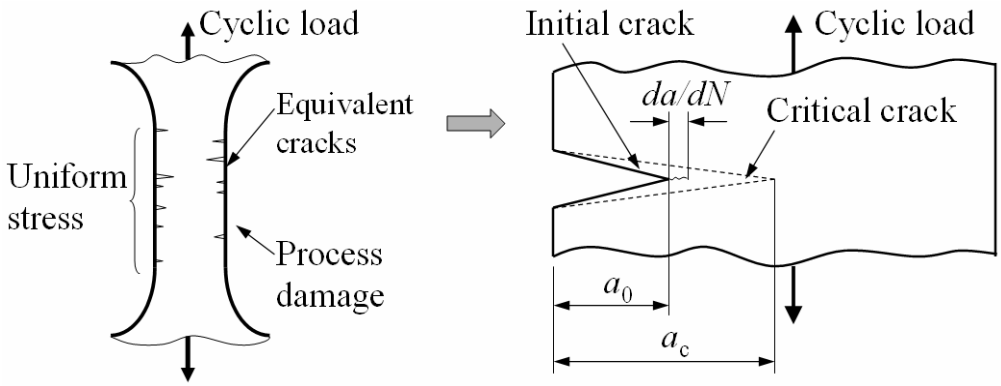


**Fig. 2.9** Fatigue extension of equivalent cracks starting from initial defects.

As has been suggested [75], not only the static strength but also fatigue lifetime as well may be correlated to the same initial damage. The defects introduced by the etching process were modeled as equivalent cracks on the etched side walls of specimens as illustrated in Fig. 2.9, which extend with microscopic dislocation slip at the crack tip as discussed in the Introduction. For the case of the fatigue tests, the applied loads were sinusoidal with stress amplitudes smaller than the specimen strengths. Therefore the specimens broke not immediately, but after individual numbers of load cycles. During this period, equivalent cracks propagate from their initial lengths $a_0$ to critical length $a_c$. The crack extension rate per cycle *da/dN* was formulated by Paris' law [82,84] in the form normalized by the fracture toughness $K_{Ic}$ as

$$\frac{da}{dN} = C\left(\frac{K}{K_{Ic}}\right)^n, \tag{2.3}$$

where $C$ and $n$ are two material parameters, and $K$ is either the maximum stress intensity factor $K_{max}$ or the amplitude of the stress intensity factor $\Delta K$. Considering again the possible movement of dislocations in micro-scale silicon structures, the stress intensity factor amplitude $\Delta K$ is expected to play a preponderant role in fatigue crack growth similarly to metallic materials. The fatigue process in both ceramic and metallic materials could be modeled with Paris' law [73]. Fatigue crack extension in metals still obeys Paris' law even at temperature as low as −125°C [85]. The results in [85], where the fatigue tests were performed with different positive load ratios, show that both the maximum stress intensity factor $K_{max}$ and $\Delta K$ control the fatigue process. It has also been suggested that the maximum stress intensity factor $K_{max}$ rather than $\Delta K$ plays the preponderant role in ceramic materials [42]. No matter whether $K_{max}$ or $\Delta K$ plays the preponderant role in micro-scale silicon, since the stress ratio $R = 0$ was applied in this study, the use of either $K_{max}$ or $\Delta K$ does not affect any result subsequently obtained. The stress intensity factor amplitude $\Delta K$ was used in Paris' law in the previous studies [75,76], and is used again in this thesis. The factor $K$ in Eq. (2.3) is then defined as

$$K = \Delta K = \beta\sigma\sqrt{\pi a}, \tag{2.4}$$

where $a$ is the crack length at cycle number $N$, $\beta$ denotes a dimensionless correction factor reflecting the geometry of both the crack and the specimen, and $\sigma$ is the

amplitude of the applied cyclic stress. In this study, $K_{Ic}$ and $\beta$ were taken as 1.1 MPam$^{1/2}$ [75,23] and 1.12 [75,82], respectively. As reported in the previous study [75], different values of $K_{Ic}$ and $\beta$ do not affect the parameter $n$, so far as they are kept to be constant throughout the crack extension process. The possible error range due to the variation of $K_{Ic}$ and $\beta$ will be discussed in Section 2.4.2 with the results of evaluation. When a specimen breaks, the stress intensity factor at the tip of the largest crack is expected to be equal to the toughness $K_{Ic}$. By integrating Eq. (2.3) with respect to the crack length from the initial crack length $a_0$ to $a_N$ which represents the crack length after $N$ cycles of load, $a_N$ is obtained as

$$a_N = \left[ a_0^{(2-n)/2} + \frac{C(2-n)}{2} \left( \frac{\beta\sigma\sqrt{\pi}}{K_{Ic}} \right)^n N \right]^{2/(2-n)} . \quad (2.5)$$

This equation expresses the extension of the initial crack as a function of the applied stress amplitude $\sigma$ and number of load cycles $N$.

On the other hand, when a specimen breaks, the stress intensity factor at the tip of the largest crack is expected to be equal to the toughness $K_{Ic}$. Therefore the strength of the material is formulated in terms of the equivalent crack length $a$ as

$$\sigma = \frac{K_{Ic}}{\beta\sqrt{\pi a}} . \quad (2.6)$$

Since the distribution of initial crack lengths can be evaluated from static strength distribution by substituting Eq. (2.6) into Eq. (2.1), the cumulative probability $F$ is formulated in the terms of crack length as

$$F = 1 - \exp\left[ -\left( \frac{a_0}{a_{\sigma 0}} \right)^{-m/2} \right], \quad (2.7)$$

with $a_{\sigma 0} = (K_{Ic}/\beta\sigma_0\pi^{1/2})^2$. Equation (2.7) represents the cumulative probability of specimens to bear cracks with maximum length longer than $a_0$. By applying Eqs. (2.5) and (2.7), the calculated crack extension behavior is illustrated in Fig. 2.10 in relation to the distribution of the initial crack length $a_0$ and the resulting fatigue lifetime distribution in terms of the number of cycles $N$. Here the parameters $\sigma_0$, $m$, $C$ and $n$ obtained in the previous study [64] were used as an example, i.e., 1.60 GPa, 12.1, $1.43\times10^{-13}$ m/cycle and 26.9, respectively. Figure 2.10 (a) shows that 80% of

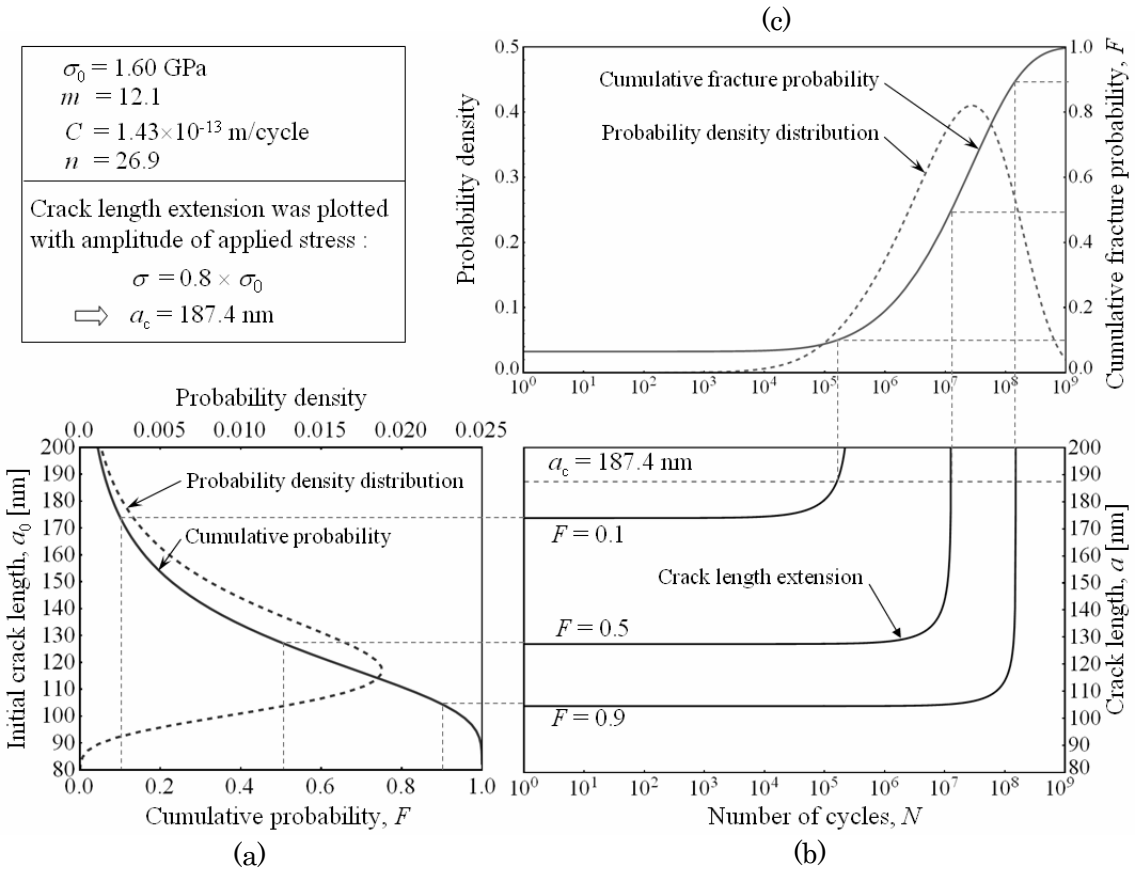


**Fig. 2.10** Crack extension versus fatigue lifetime.

equivalent initial crack length $a_0$ was in a range from 105 to 175 nm. It was however difficult to directly identify the initial cracks on the specimens because of the roughness of etched surface and the length of specimen. In addition, unfortunately, the specimen broke away into pieces, which makes it also difficult to survey the fracture surface.

Starting from the initial crack length distribution as shown in Fig. 2.10 (a), the crack length extension was calculated with the applied amplitude of stress $\sigma = 0.8\sigma_0$ as an example and plotted in Fig. 2.10 (b). Three lines were plotted with three different values of the cumulative probability $F$ corresponding to three different initial crack lengths $a_0$. The crack length increases with the number of cycles $N$ and the specimen breaks when a crack reaches the critical crack length $a_c = (K_{Ic}/\beta\sigma\pi^{1/2})^2$, i.e., the stress intensity factor at the crack tip reaches the toughness. The crack extension behavior in Fig. 2.10 (b) may not be similar to those observed with the stress ratio $R = -1$ in the literature [29,32,34,36], where change in resonance frequency was attributed

to fatigue crack extension and the rate of change did not increase sharply towards the end of lifetime. On the other hand, in the case of damage accumulation evaluated in terms of stiffness decrease, it was reported that the change became considerable only after about $10^5$ and $10^6$ cycles [39]. Taking the effect of compressive stress discussed in the Introduction [30,27,38] also into account, the apparent fatigue behavior under the stress condition without compression could be considerably different from that already reported with compressive stress. The cumulative fracture probability $F$ corresponding to the intersection of critical crack length $a_c$ and the lines of crack extension in Fig. 2.10 (b) was plotted in Fig. 2.10 (c).

The fracture probability for a specimen to break after $N$ cycles under loads up to $\sigma$ is now given a mathematical form. By substituting $a_N$ with $a_c$ in Eq. (2.5), the initial crack length leading to fracture after $N$ cycles is obtained as a function of the applied stress:

$$a_0 = \left( \frac{K_{Ic}}{\beta\sigma\sqrt{\pi}} \right)^2 \left[ 1 + \frac{C(n-2)}{2} \left( \frac{\beta\sigma\sqrt{\pi}}{K_{Ic}} \right)^2 N \right]^{2/(2-n)} . \qquad (2.8)$$

By substituting $a_0$ in Eq. (2.7) with Eq. (2.8), the cumulative fracture probability $F$ is obtained as

$$F = 1 - \exp\left\{ -\left( \frac{\sigma}{\sigma_0} \right)^m \left[ 1 + \frac{C(n-2)}{2} \left( \frac{\beta\sigma\sqrt{\pi}}{K_{Ic}} \right)^2 N \right]^{m/(n-2)} \right\} . \qquad (2.9)$$

When the number of cycles $N$ is 0, Eq. (2.9) becomes identical to Eq. (2.1) showing the static strength distribution. From this equation, distributions of fatigue lifetime can be estimated at arbitrary applied stress levels.

The two parameters $C$ and $n$ are determined by fitting Eq. (2.9) to experimental data. When the LSM is applied as in the previous studies [75,76], the sum of the squared deviations between the cumulative fracture probability calculated with Eq. (2.9) and the experimental set of data was minimized by varying $C$ and $n$. In this calculation, the fatigue test data of each group were ranked in descending order of the initial crack length $a_0$ calculated with Eq. (2.8), and then the cumulative fracture probability $F$ of the fatigue test data was obtained by using Eq. (2.2). When the MLM is applied, the probability density function (PDF) is derived as

$$f = \begin{cases} \partial F/\partial \sigma & \text{when } N = 0 \\ \partial F/\partial N & \text{when } N > 0, \end{cases} \tag{2.10}$$

since the applied cyclic stress is from 0 to the maximum stress and the number of cycles starts from 0. It is understood that $f$ corresponds to a static test in Eq. (2.9) when a specimen breaks at $N$ = 0, i.e., the specimen breaking during the first monotonic load increase is unable to complete the first load cycle. In this case, the cumulative fracture probability depends only on the applied stress $\sigma$. Therefore the PDF $f$ is simply defined by taking the derivative of the cumulative fracture probability with respect to $\sigma$. However, if the specimen survives the first cycle, it goes into the fatigue test regime. Because the applied stress amplitude is constant, the cumulative fracture probability of the specimen depends only on the number of load cycles. Therefore $f$ is defined by taking the derivative of the cumulative fracture probability with respect to $N$. An example of such a PDF is plotted as a dashed curve in Fig. 2.10 (c). The likelihood of obtaining a set of observations $\{\sigma,N\}$ with probability density function $f(\sigma,N|\, C,n)$ is the product of the PDF values of all the observations as [77-79], i.e.,

$$L = \prod_{i=1}^{I} f(\sigma_i, N_i | C, n). \tag{2.11.a}$$

In practice it is often more convenient to work with the logarithm of the likelihood function, i.e., the log-likelihood ln$L$ defined as

$$\ln L = \sum_{i=1}^{I} \ln f(\sigma_i, N_i | C, n). \tag{2.11.b}$$

The MLM estimates the parameters $C$ and $n$ by finding their set of values maximizing $L$ or, equivalently, ln$L$. This so-called best estimates of $C$ and $n$ simultaneously satisfies

$$\begin{cases} \dfrac{\partial \ln L}{\partial C} = 0 \\ \dfrac{\partial \ln L}{\partial n} = 0. \end{cases} \tag{12}$$

Best MLM estimates of the two parameters $C$ and $n$ were thus obtained by solving Eq. (2.12).

## 2.4. Calculation and discussion

### *2.4.1. Estimation of optimum parameters in Paris' law*

First, the optimization of $C$ and $n$ was performed by the LSM. In addition to optimal parameters for individual specimen groups, combined optimal parameter values were obtained by pooling data of two groups and fitting their results with common values of $C$ and $n$. Similarly, common optimal values were obtained by pooling the data of all three groups. Results are shown in Table 2.3 (a). The combined optima are close to each other and close to the common optimum despite the spread of individual optima. The values of $n$ evaluated here appear to be fairly large in comparison to those commonly obtained with metallic materials, but lie within the range of those reported for mono-crystalline silicon and polysilicon extending roughly from 10 to 50 [86]. High values of the crack growth exponent were also obtained with A533 B steel at low temperature [87], i.e., the crack growth rate data obtained at 77K indicated a value of $n$ as high as 48. In the case of pearlitic steel tested with load ratio $R = 0.7$ at temperature of −125°C, $n$ was found to be up to 38 [85]. In summary, the exponent $n$ of silicon as well as metal could assume values in a wide range. In the previous study [76], the values of $C$ and $n$ were presented as $9.30\times10^{-14}$ m/cycle and 26.9, respectively, for Group A and correspondingly $1.83\times10^{-13}$ m/cycle and 25.8 for Group B. The values of $C$ in this study appear different because $C$ depends on the value of $K_{Ic}$ [75]. A different estimate of $K_{Ic}$ was used in the previous study [76]. The value of $n$ of Group A was the same as that obtained in this study while $n$ of Group B was different from this study because it has recently been found that the calculation for Group B in the previous study had not yet correctly converged to the true optimum.

In Table 2.3 (a), no pair of number matches exactly. However, this may not necessarily mean that the fatigue behavior of three groups is completely different. Figure 2.11 presents the distribution of the cumulative fracture probability versus the applied stress $\sigma$ and number of cycles $N$ calculated for each group with respective $m$ and $\sigma_0$ but with common optima of $C$ and $n$. The larger and smaller dots show the experimental fatigue data and their projections onto the calculated surface, respectively. The cumulative fracture probability $F$ of an experimental data point was calculated by Eq. (2.2). Despite the difference between common and individual optima, calculation results excellently follow the trends of experimental data for all

the three groups. This suggests that those differences are physically not marked and that they are within a scatter range observed among different samples from a common mother group. In order to give a quantitative insight into this point, possible distribution ranges of the parameters *C* and *n* were statistically estimated as follows.

**Table 2.3.** The optimum values of power parameters *C* and *n*

(a) Least squares method

| Parameters | | *C* [m/cycle] | *n* |
|---|---|---|---|
| Individual optima | Group A | $1.43\times10^{-13}$ | 26.9 |
| | Group B | $1.86\times10^{-13}$ | 18.0 |
| | Group C | $1.55\times10^{-12}$ | 34.3 |
| Combined optima | Groups A and B | $8.51\times10^{-13}$ | 32.7 |
| | Groups B and C | $9.55\times10^{-13}$ | 30.4 |
| | Groups C and A | $1.32\times10^{-12}$ | 36.9 |
| Common optimum (obtained with all three groups) | | $1.62\times10^{-12}$ | 36.2 |

(b) Maximum likelihood method

| Parameters | | *C* [m/cycle] | *n* |
|---|---|---|---|
| Individual optima | Group A | $1.82\times10^{-14}$ | 31.3 |
| | Group B | $2.45\times10^{-13}$ | 22.2 |
| | Group C | $1.45\times10^{-12}$ | 38.3 |
| Combined optima | Groups A and B | $1.74\times10^{-13}$ | 34.3 |
| | Groups B and C | $8.71\times10^{-13}$ | 34.1 |
| | Groups C and A | $5.25\times10^{-13}$ | 40.6 |
| Common optimum (obtained with all three groups) | | $5.01\times10^{-13}$ | 37.1 |

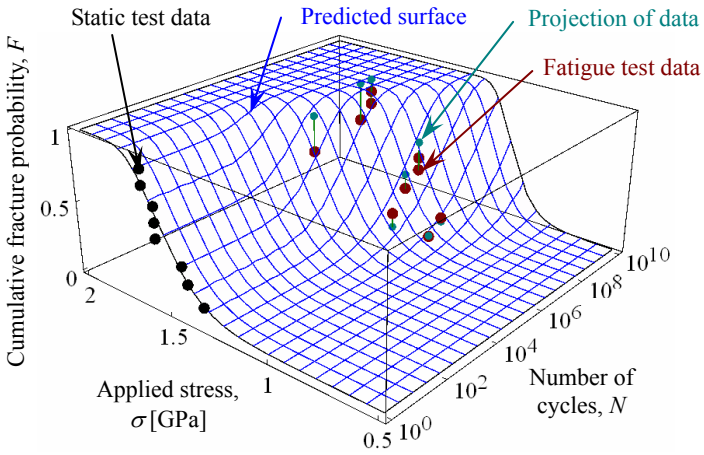


(a) Group A

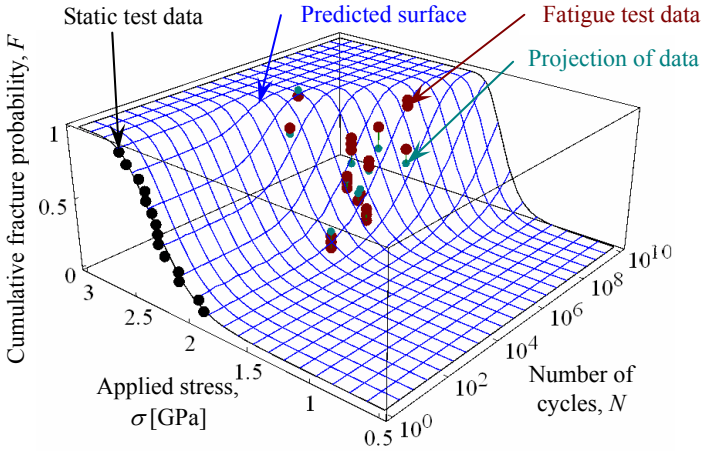


(b) Group B

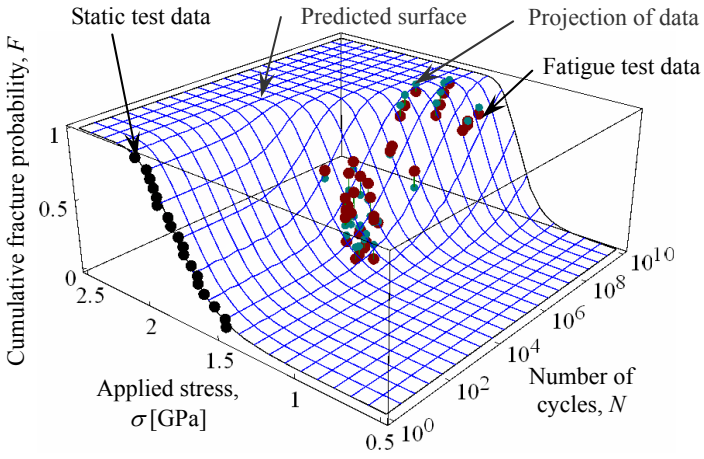


(c) Group C

**Fig. 2.11** Three-dimensional plots of the fatigue behavior of the three specimen groups using common values of $C$ and $n$.

The difference between the two cumulative fracture probabilities obtained by experiment and calculation with the optimized parameters is here called deviation. The root mean square (RMS) deviation is defined as

$$\Delta F_{RMS} = \sqrt{\frac{1}{I}\sum_{i=1}^{I} \Delta F_i^2} \ . \tag{2.13}$$

Figure 2.12 shows optimum regions and points in the *C*-*n* space. The optimum *C*-*n* points, shown as symbols, are those parameter combinations where $\Delta F_{\mathrm{RMS}}$ attains its minimum value $\Delta F_{\mathrm{RMSmin}}$ listed in Table 2.4. The contours show loci of *C*-*n* combinations with RMS deviations from the experimental data larger than $\Delta F_{\mathrm{RMSmin}}$ by 0.03. The increment of 0.03 was selected so as to give bounds of parameters comparable to the 90% MLM confidence bounds evaluated below. The contours indicate that the increment of the RMS deviation is not marked when the values of *C* and *n* lie in a direction into which the contours extend. It means that the parameter values within these ranges are likely to be obtained from a single mother group of fatigue behavior and that they are consequently sensitive to small changes of the RMS deviation, i.e., sensitive to individual data shifts. It explains why the optimum values of the parameters scatter in a large range, especially when the number of experimental data is small. Therefore, even if the optimum values between the three groups seem to be different, they can represent a unique fatigue behavior and the most likely optimum values, i.e. the common optimum can be used for all the groups with a small value of the RMS deviation $\Delta F_{\mathrm{RMS}}$.

On the other hand, optimum values of the two parameters *C* and *n* obtained with MLM by solving Eq. (2.12) are shown in Table 2.3 (b). Ratios of the likelihood functions were used to draw confidence bounds appropriately called likelihood ratio confidence bounds. Likelihood ratio confidence bounds are based on the equation [88,89]

$$-2\ln\left(\frac{L_1}{L_2}\right) = \chi^2_{\alpha,k} \ , \tag{2.14}$$

where $L_1$ is the likelihood function for the unknown parameters lying on the confidence bound, $L_2$ is the likelihood function for the best estimates obtained by the MLM, and $\chi^2_{\alpha,k}$ is the chi-square distribution with the confidence level $\alpha$ and the

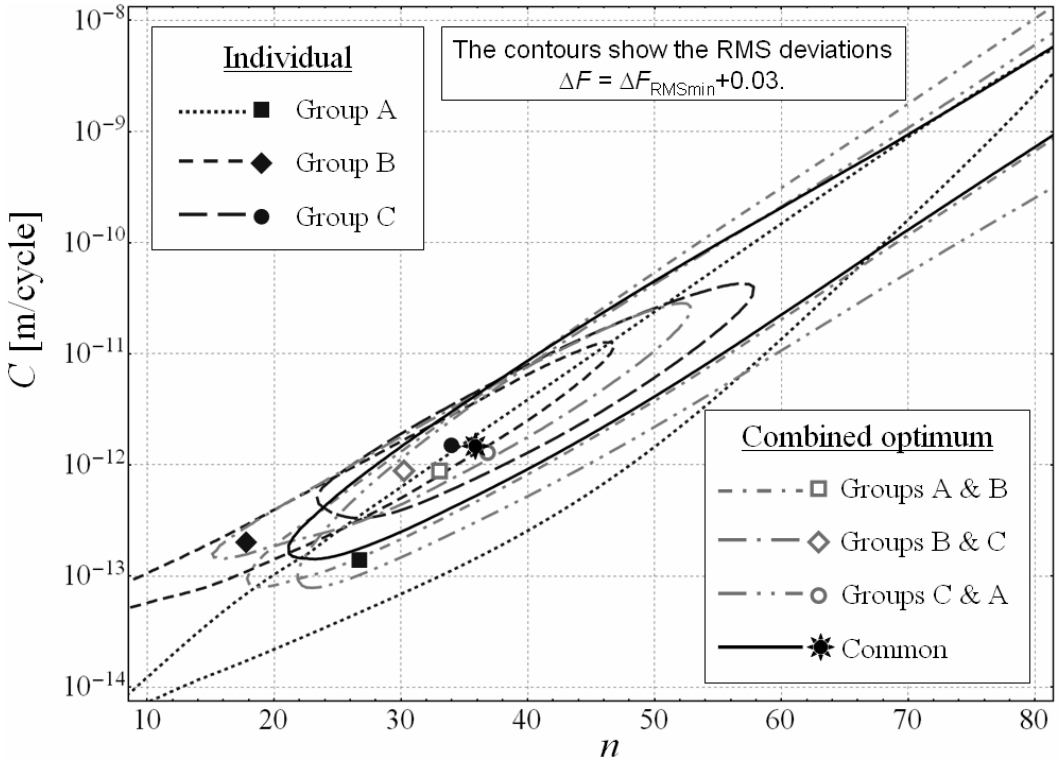


**Fig. 2.12** Contours of RMS deviations and optimum points of $C$ and $n$ obtained by the least squares method with the individual and combined groups.

**Table 2.4.** The value of root mean square deviation for the best fits

| | Individual optimum | | | Combined optimum | | | |
|---|---|---|---|---|---|---|---|
| Groups | A | B | C | A and B | B and C | A and C | Common |
| $\Delta F_{\mathrm{RMSmin}}$ | 0.128 | 0.059 | 0.075 | 0.126 | 0.077 | 0.118 | 0.113 |

number of estimated parameters $k$.

The confidence bounds of parameters of $C$ and $n$ were drawn at a level of 90% in Fig. 2.13 as the black contours for individual groups and the common analysis. These contours indicate the area in which 90% of $C$-$n$ combinations obtained with data samples out of a mother group are expected to lie. The solid symbols show the optimum values of $C$ and $n$ obtained by the MLM as the best estimates where the likelihood function is maximized. For convenient comparison, the contours and the optimum points obtained by the LSM were also included as corresponding types of

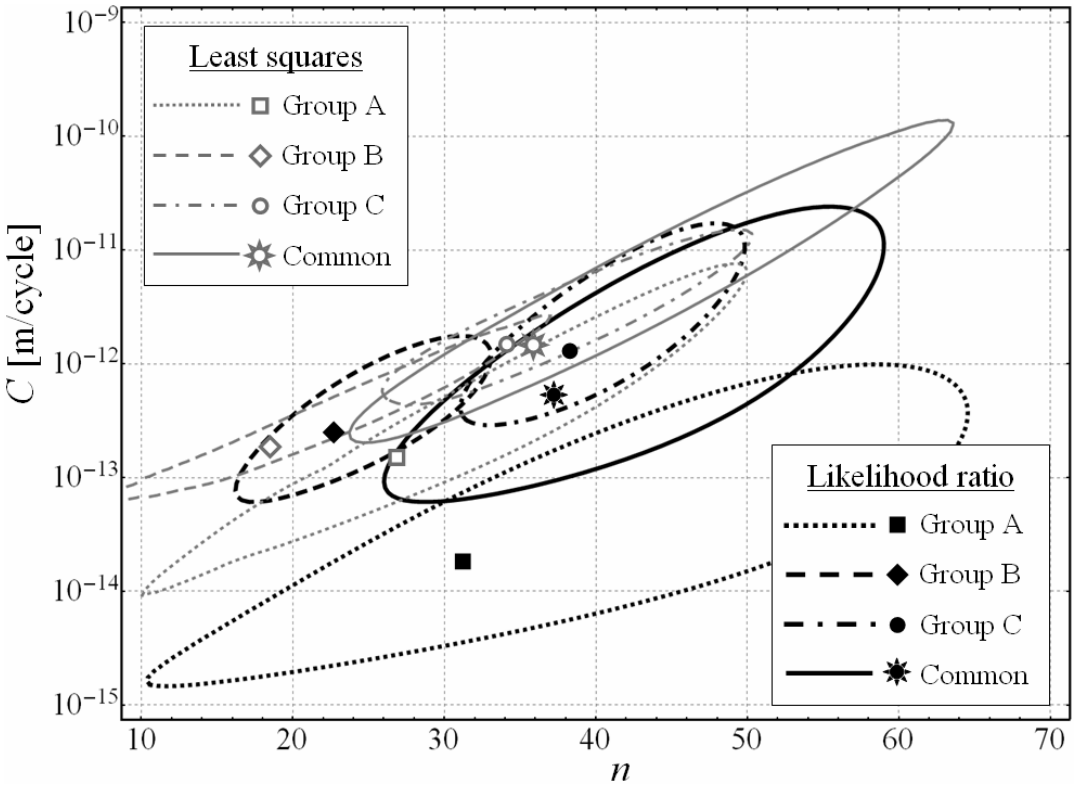


**Fig. 2.13** Comparison the optimum results of *C* and *n* obtained by the least squares method and the maximum likelihood method.

gray contours and open symbols. This plot therefore shows that most of the optimum values of *C* and *n* obtained by the LSM lie within the confidence bounds estimated by the MLM.

The fact that the estimated values lie within the confidence bound of the common case and all the contours overlap with each other for all the cases especially in Fig. 2.12 suggests that their optimum values of parameters can all be obtained from a mother group with unique characteristics, i.e., their fatigue characteristics is the same in terms of *C* and *n* despite the marked differences in static strength levels. On the other hand, the results of Group A obtained with the LSM and MLM do not match each other in Fig. 2.13 while those of other groups and common calculation matched relatively well. It was indicated in the literature [90] that the MLM estimation is biased and depends much on the sample size. Therefore the large difference between the results of Group A obtained by the two methods might be caused by the small number of data. Another possible reason could be that the etching recipe of specimens of Group A was different from that of the other two groups. Therefore it remains still

ambiguous whether the two parameters $C$ and $n$ are independent of the etching recipe or inherent to the material. However, Fig. 2.11 indicates that the fatigue test data of the three groups are described well by a unique set of parameters $C$ and $n$. Then, from a practical point of view, it is interesting to know the expected error levels when representative values of $C$ and $n$ are applied for the prediction of lifetime distribution. For this purpose, the discussion is focused in the next section on the fatigue lifetime prediction with the common values of $C$ and $n$ in Table 2.3 and its deviation from the fatigue lifetime distribution estimated with a set of parameters deviating from the common values.

### *2.4.2. Fatigue lifetime distribution*

The fatigue lifetime, denoted by the number of cycles $N$ under an applied stress amplitude $\sigma$ with cumulative fracture probability $F$ being given, can be explicitly calculated with optimized parameters by rewriting Eq. (2.9) as

$$N = \left(\frac{K_{\mathrm{Ic}}}{\beta\sigma\sqrt{\pi}}\right)^2 \frac{2}{C(n-2)} \left\{ \left[ -\left(\frac{\sigma_0}{\sigma}\right)^m \ln(1-F) \right]^{(n-2)/m} - 1 \right\}. \quad (2.15)$$

Because the fatigue lifetime $N$ is larger than 0, Eq. (2.15) is true when the condition $F \leq 1-\exp[-(\sigma/\sigma_0)^m]$ is satisfied. Stress-lifetime (S-N) curves calculated by applying Eq. (2.15) are shown in Figs. 2.14 (a)-(c) for the three groups. The solid and dashed curves in these figures present the S-N curves when using the common and individual optimum values of $C$ and $n$ obtained by LSM, respectively. The S-N curves were plotted with the values 0.1, 0.5 and 0.9 of $F$ starting from the static strength distribution. The symbols in Fig. 2.14 show fatigue test data. Although the scatter ranges are large, it appears that all the groups roughly follow a unique fatigue behavior indicated by the solid lines drawn with the common set of parameters $C$ and $n$.

To see the possible effect of testing frequency, the S-N curves with $F = 0.5$ and the experimental data of the three groups shown in Figs. 2.14 (a)-(c) were re-composed into Fig. 2.14 (d) in a normalized fashion with respect to $\sigma_0$. Due also to the large scatter in lifetime, it is difficult to clearly see the effect of testing frequency on the fatigue lifetime. When the curves are compared, however, the lifetimes of Groups

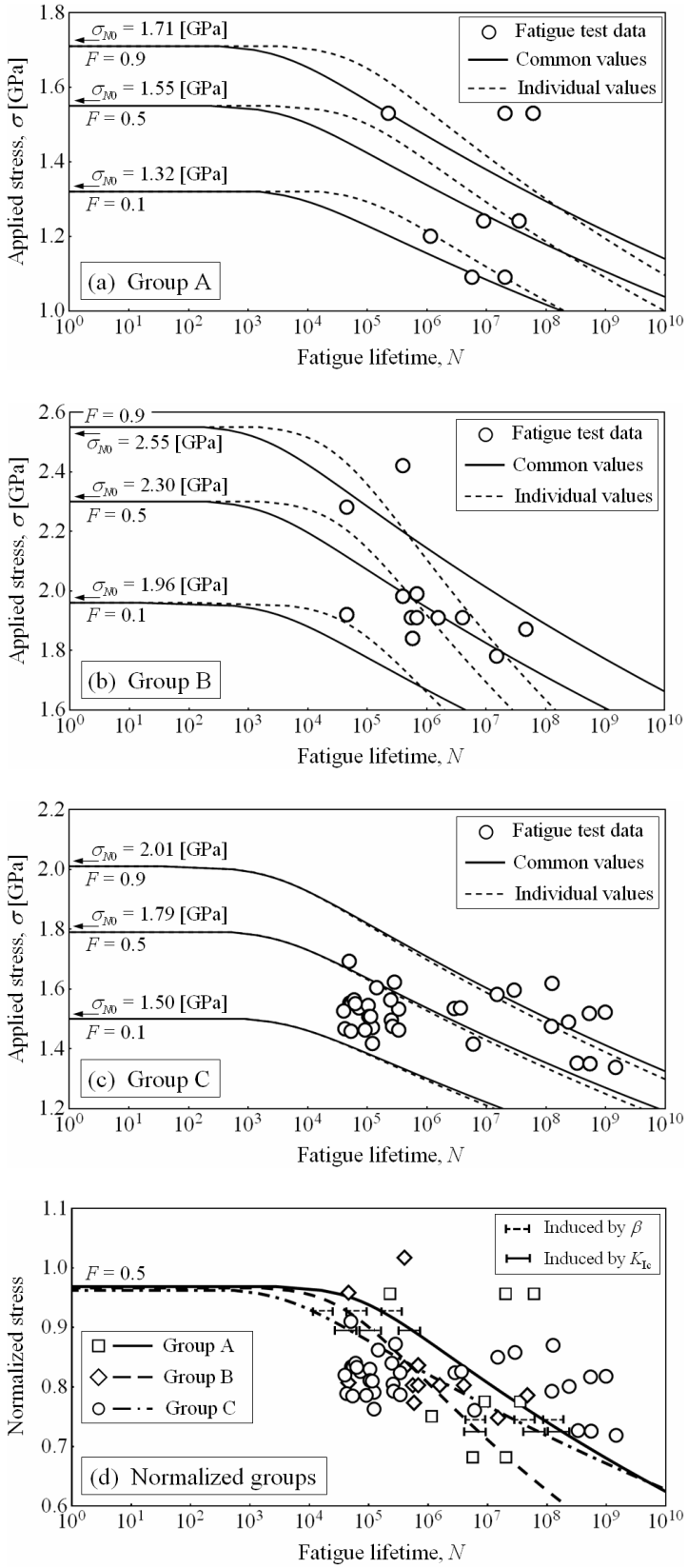


**Fig. 2.14** S-N curves of the three groups using the values of $C$ and $n$ obtained by the least squares method.

A and B appear longest and shortest, respectively, while the frequencies in the fatigue tests of Groups A and C were lowest and highest. This trend observed here looks different from what was reported in the literature where a higher frequency (40 kHz in comparison to 4 kHz) resulted in a longer lifetime distribution [34] in terms of numbers of cycles. In contrast, the effect of the testing frequency was also reported to be negligible when tested within the lower range of frequency (from 50 Hz to 6000 Hz) [35]. Judging from the frequencies in this study ranging from 100 Hz to 500 Hz, the results with little frequency effect shown in Fig. 2.14(d) is consistent with the reported situation.

The origin of data scatter in Fig. 2.14 was considered in the analysis above as the distribution of initial crack lengths determining the static strength. However, especially for the case of polysilicon, there is also a possibility where random grain orientation causes the scatter through different values of fracture toughness $K_{Ic}$. The geometry factor $\beta$ may also change. So far as $K_{Ic}$ and $\beta$ are constant during the crack extension process as assumed in the analysis, the value of $n$ estimated with Eq. (2.9) does not change even if different values of $K_{Ic}$ and $\beta$ are applied. However, their change during the crack extension causes the change of both $C$ and $n$. In both the cases, the changes in $K_{Ic}$ and $\beta$ lead to an error range in the analysis. The toughness was reported to vary from 0.84 $MPam^{1/2}$ to 1.24 $MPam^{1/2}$, which was attributed to the local cleavage anisotropy and relative orientation of the grains [91]. When a crack changes its shape from a semi-circular crack to a through-the-thickness two-dimensional crack, the value of $\beta$ for the largest stress intensity factor changes from 0.71 to 1.12. To evaluate the consequences of these uncertainties, changes in lifetime distributions due to the change in these parameters were calculated, and plotted in Fig. 2.14 (d) as the solid and dashed small horizontal bars. They indicate the calculated ranges of fatigue lifetime change corresponding to the ranges between those two sets of extreme values of $K_{Ic}$ and $\beta$ mentioned above. Although they are plotted at particular positions, their length, i.e., the calculated ranges of change in logarithmic scale, were constants for all the positions along the S-N curves. They are indeed far shorter than the ranges of actual data scatters. Therefore, the large scatter of the fatigue lifetime is most likely caused by the scatter of initial crack length as analyzed above.

Another point to be mentioned concerning the scatter is that the S-N curve

with $F = 0.9$ appears to leave more than 10% of the data on the outside, especially in Fig. 2.14(c). Since the cumulative fracture probability $F$ of the experimental data was calculated with Eq. (2.2), the data distribution may have been distorted when it was transferred from the lifetime to the cumulative fracture probability. As a comparison, Fig. 2.15 shows the S-N curves of Group C calculated by using the estimated values of $n$ and $C$ obtained by MLM where the experimental data were not ranked. The number of data lying out of the S-N curve with $F = 0.9$ was then reduced. It means that the calculated distribution with the optimum values may also slightly change depending on the methods of statistical analysis.

The curves in Figs. 2.14 (a)-(c) also show that the calculated lifetimes are indeed different between the cases when the individual and common values of $C$ and $n$ are applied with the same applied stress. The difference in lifetime calculated with common values and those deviating from common values are evaluated here in logarithmic scale as

$$\Delta \log N = \log N\big|_{C^*,n^*} - \log N\big|_{C,n}, \tag{2.16}$$

where $N$ is the calculated number of cycles from Eq. (2.15), $C$ and $n$ are here the common optimum values as the representative reference, $C^*$ and $n^*$ are values deviating from $C$ and $n$. The function log stands for the logarithm to the base 10. By substituting Eq. (2.15) into Eq. (2.16), $\Delta\log N$ is written as

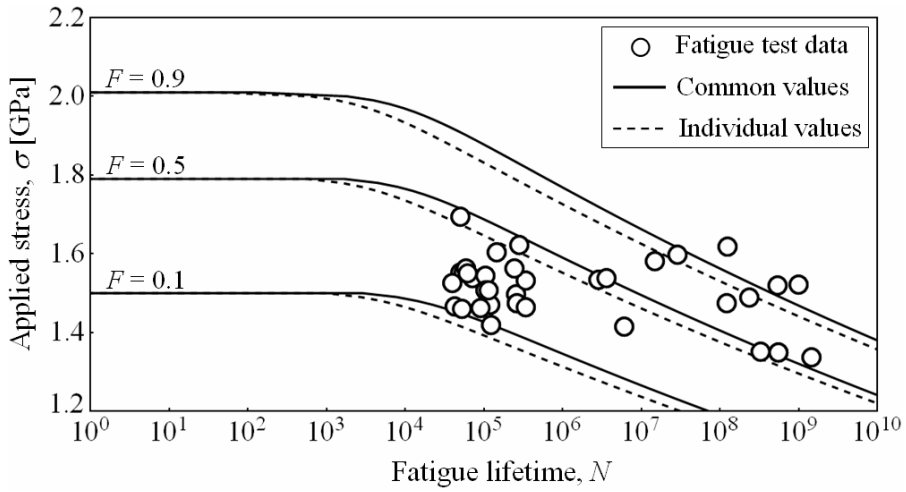


**Fig. 2.15** S-N curves of Group C using the values of $C$ and $n$ obtained by the maximum likelihood method.

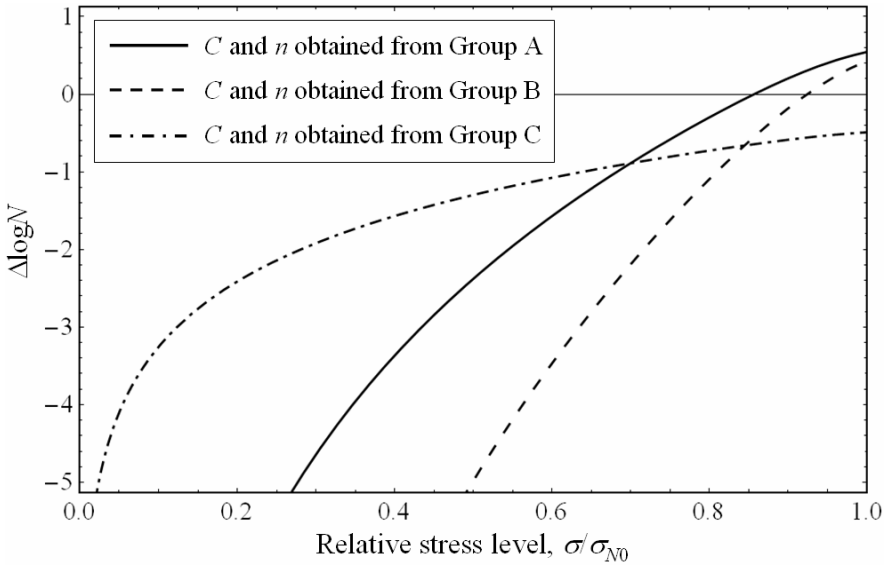


**Fig. 2.16** Error distribution in lifetime when the estimated parameters deviate from the optimum values of $C$ and $n$.

$$\Delta \log N = \log\left(\frac{C(n-2)}{C^*(n^*-2)}\right) + \log\left(\frac{1-(\sigma/\sigma_{N0})^{n^*-2}}{1-(\sigma/\sigma_{N0})^{n-2}}\right), \qquad (2.17)$$

where $\sigma_{N0}$ is the stress value which yields a determined value of $F$ in the static strength test. The values of $\sigma_{N0}$ corresponding to the different values of $F$, i.e., 0.1, 0.5 and 0.9, of the groups are shown in Figs. 2.14 (a)-(c), where the arrows indicate that the stress value of the S-N curves converge to $\sigma_{N0}$ when $N$ decreases to 0. The ratio of $\sigma$ to $\sigma_{N0}$ is called as relative stress level. It represents a relative value of applied stress on an S-N curve and takes values from 0 to 1. As indicated in Eq. (2.17), $\Delta\log N$ depends only on the relative stress level $\sigma/\sigma_{N0}$. Therefore, the distribution of the difference in predicted lifetime can be examined using a single analysis for arbitrary values of the cumulative fracture probability $F$.

The distributions of $\Delta\log N$ were calculated and are plotted in Fig. 2.16 with the different values of $C^*$ and $n^*$ assuming the individual optimum values for the three groups in Table 2.3 (a). Figure 2.16 compactly summarizes the difference in lifetime when estimated with a set of parameters $C^*$ and $n^*$ deviated from the representative values of $C$ and $n$. The results show that the absolute value of $\Delta\log N$ is smaller than 1 which corresponds to a factor of 10 in terms of $N$ when the relative stress level $\sigma/\sigma_{N0}$ is larger than 0.8, i.e., the applied stress is larger than $0.8\sigma_{N0}$. This

fact suggests that we may predict the lifetime on the basis of the static strength distribution with the common optima in accordance with specified values of $F$ within a factor 10 so far as the low cycle range is concerned. The deviation seems to be a rather large, but it helps to limit the range of fatigue lifetime prediction at this moment. When the relative stress level is small, however, it is difficult to give a reliable prediction, which is probably because our experimental data is limited to a cycle range smaller than $10^9$ cycles. Further fatigue tests to be performed with smaller applied stress amplitude would improve the prediction in the higher cycle range, which is made difficultly at the moment by the limited testing frequency of 500 Hz.

## 2.5. Conclusion

The fatigue process determining the lifetime was formulated by using Paris' law. In order to find whether the same two parameters $C$ and $n$ of Paris' law can be used to predict the fatigue lifetime of polysilicon thin films through the equivalent crack extension model to represent the damage accumulation process, experimental data of the static strength and fatigue lifetime were examined for three groups of specimens with different static strength levels. Optimum values of $C$ and $n$ for individual groups and for all the groups were obtained by two methods, namely the LSM and the MLM, in order to investigate the validity of evaluated parameters. All the optimum sets of parameter values were indeed different from each other. By surveying the confidence bounds and the distributions of the RMS deviation between the experimental data and calculation, it was found that they scatter over a range, which led to the ambiguity of concluding whether they are inherent to the material. The remaining ambiguity is further examined from a bit different aspect in the next chapter. However, the fatigue lifetime distribution was found to be reasonably well predicted by using a unique set of parameters $C$ and $n$ despite marked differences in static strength levels among those groups of specimens. These findings suggest that fatigue lifetime estimation on the basis of static strength distribution is possible, which may also indirectly suggest the possibility that defect accumulation causes fatigue fracture in polysilicon.

# Chapter III

# Estimation of Fracture Strength and Fatigue Lifetime of Arbitrarily-Shaped Polysilicon Thin Films

## 3.1. Introduction

In Chapter II, the fatigue lifetime distribution of polysilicon thin films was surveyed and formulated using Paris' law as a fatigue crack extension process starting from equivalent initial cracks whose lengths were determined from the distribution of the initial static strength [92]. It showed that the lifetime can be predicted on the basis of the static strength by using the same values of the parameters of Paris' law, regardless of different levels of static strength. However, the large range of the parameter values led the ambiguity of conclusion whether they are unique. Besides, all the used specimens had the same shape and the stress distribution in the specimens was assumed to be uniform.

On the other hand, many reports concerning the strength and fatigue behavior of silicon used notched specimens [15,16,23,27-29,31-34,37,74,81,86,93,94] with non-uniform stress distributions. Although the strength and fatigue behaviors were so far understood for those specifically shaped specimens, the obtained information could not be used to estimate the behavior of structures with other shapes. Since shapes and sizes of structures in MEMS vary widely among applications, it is difficult to perform the tests with all those structures. Therefore, from the view point of engineering, a method to evaluate the fracture strength and fatigue lifetime of arbitrarily-shaped structures from the experimental results of a specific structure type is necessary in order to design MEMS structures.

In this chapter, firstly, the theory presented in Chapter II is extended to polysilicon thin films with arbitrary shapes or non-uniform stress distributions. It is applied to evaluate the static strength and fatigue behaviors of three types of specimens with different shapes fabricated under the same conditions as applied for Group C in Chapter II. The first type here is the specimens of Group C with the shape and experimental data already presented in Chapter II. They are flat specimens, i.e., without notch. The other two types are designed with notches of two different shapes. Since the specimens were etched under the same etching condition, their etching damage is assumed to be identical regardless of the shapes of specimens. Then, the strength and fatigue behavior should have the same local characteristics at any position on the patterned surface in view of the initial damage and equivalent crack extension process. By taking the stress distribution on etched surfaces of specimens

into account, the theory is refined to obtain the parameters in the Weibull distribution and Paris' law which determine such local characteristics of static strength and fatigue behavior. The parameters are evaluated using the maximum likelihood method (MLM) [77-79]. The likelihood ratio test is applied to estimate the confidence bounds of estimated parameters on the basis of the results of the MLM and the chi-square distribution [88,89]. By analyzing the confidence bounds, the parameters describing local characteristics of the polysilicon thin films are investigated in order to see whether the obtained parameters are the same regardless of the shapes of specimens.

The large scatter of the estimated values of the parameters obtained from the specimens without a notch presented in Chapter II left an ambiguity in the conclusion of fatigue behavior of polysilicon thin films fabricated under different etching condition. In order to confirm the conclusion of Chapter II, next, two groups of specimens are newly designed and fabricated under the different etching conditions. They are also subjected to static and fatigue tensile tests. The estimated parameters in Paris' law estimated from the new two groups and those obtained from the previous group are also compared to each other. The confidence bounds are analyzed in order to confirm whether the fatigue process in polysilicon thin films has the same characteristics despite the stress distributions and initial damage distribution on the specimens.

## 3.2. Statistical analysis

### *3.2.1. Static strength test*

It is known that the strength of brittle materials such as silicon shows large scatter which is well described by the Weibull distribution [8,84]. In this chapter, only the etched surfaces of specimens were considered as the location for the initiation of fracture. Therefore, when the stress distribution in a specimen is not uniform, the cumulative fracture probability $F$ of the entire etched surface of a specimen is defined in general form as [95,96]

$$F = 1 - \exp\left[ -\int_A \left( \frac{\sigma_a}{\sigma_0} \right)^m \frac{dA}{A_0} \right], \tag{3.1}$$

where $m$ denotes the Weibull modulus or shape parameter representing the data scatter,

$\sigma_0$ denotes the scale parameter related to the average strength of the infinitesimal area $dA$, and $\sigma_a$ is the applied stress. The symbol $A$ indicates the area of the entire etched surface of specimens.

Equation (3.1) can be applied to any specimens with arbitrary shape if the distribution of the applied stress $\sigma_a$ is known. For the actual calculation, Eq. (3.1) can be rewritten in the discretized form as

$$F = 1 - \exp\left[ -\sum_e \left( \frac{A_e}{A_0} \right) \left( \frac{\sigma_e}{\sigma_0} \right)^m \right], \tag{3.2}$$

where $A_e$ and $\sigma_e$ are the area and the average stress of the surface element, respectively, as described in Fig. 3.1. One basically imagines the etched surface of a specimen to be composed of many small elements and the stress $\sigma_e$ in each element to be uniform. Under the assumption of linear elastic deformation, the stress $\sigma_e$ of each element is correlated to the maximum stress $\sigma$ in the specimen by the ratio of $\sigma_e$ to $\sigma$, which is notated as $k_e = \sigma_e/\sigma$. Equation (3.2) is then rewritten as a function of a variable $\sigma$ by

$$F = 1 - \exp\left[ -\left( \frac{\sigma}{\sigma_0} \right)^m \sum_e \gamma k_e^m \right], \tag{3.3}$$

where $\gamma$ is the ratio of the area of the surface element $A_e$ to the area $A_0$.

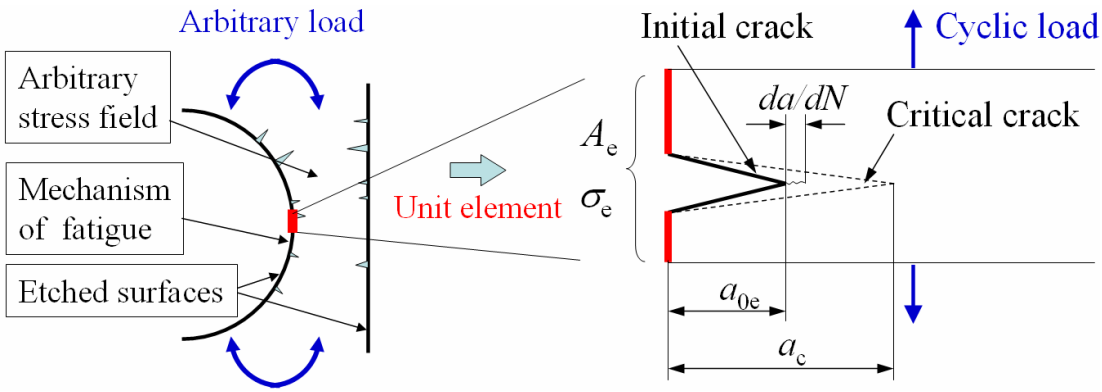


**Fig. 3.1** Schematic of the fatigue extension of equivalent cracks starting from initial defects.

A probability density function (PDF) is derived from Eq. (3.3) as

$$f_s = \frac{\partial F}{\partial \sigma} = \left[ \frac{m}{\sigma_0} \left( \frac{\sigma}{\sigma_0} \right)^{m-1} \sum_e \gamma k_e^m \right] \exp\left[ -\left( \frac{\sigma}{\sigma_0} \right)^m \sum_e \gamma k_e^m \right]. \quad (3.4)$$

In the MLM [77-79], the likelihood function of obtaining a set of observations $\{\sigma\}$ with the PDF denoted by $f_s(\sigma|\sigma_0,m)$ is the product of the PDFs of all the observations, i.e.,

$$L_s = \prod_{i=1}^{I} f_s(\sigma_i|\sigma_0,m), \quad (3.5)$$

where $I$ denotes the number of tested specimens of each data group. The likelihood function can be presented in the form of natural logarithm as

$$\ln L_s = \sum_{i=1}^{I} \ln f_s(\sigma_i|\sigma_0,m) = \sum_{i=1}^{I} \left\{ \ln\left[ \frac{m}{\sigma_0} \left( \frac{\sigma_i}{\sigma_0} \right)^{m-1} \sum_e \gamma k_e^m \right] - \left( \frac{\sigma_i}{\sigma_0} \right)^m \sum_e \gamma k_e^m \right\}. \quad (3.6)$$

The MLM estimates the parameters $\sigma_0$ and $m$ by finding their values maximizing $L_s$ or $\ln L_s$. These so-called the best estimators simultaneously satisfy

$$\begin{cases} \dfrac{\partial \ln L_s}{\partial \sigma_0} = 0 \\ \dfrac{\partial \ln L_s}{\partial m} = 0 \end{cases}. \quad (3.7)$$

The best MLM estimators of the parameters $\sigma_0$ and $m$ are thus obtained by solving Eq. (3.7).

### *3.2.2. Fatigue test*

It has been suggested that not only the static strength but also the fatigue lifetime is correlated to the same initial damage [75]. The defects caused by the etching process were modeled as equivalent cracks on the etched surfaces of the specimens as illustrated in Fig. 3.1. In the fatigue tests, the applied loads were sinusoidal with the stress amplitude smaller than the specimen's strength. Therefore the specimens broke not immediately but after a number of load cycles $N \geq 1$ which is here called as the specimen's fatigue lifetime. During this period, equivalent cracks in an element propagate from their initial length $a_{0e}$ to the critical length $a_c$. The

extension rate of the equivalent crack under cyclic loading, named the crack growth rate *da*/*dN*, is formulated by Paris' law [82,84] in the form normalized by fracture toughness $K_{\mathrm{Ic}}$ as

$$\frac{da}{dN} = C\left(\frac{\Delta K}{K_{\mathrm{Ic}}}\right)^{n}, \tag{3.8}$$

where $C$ and $n$ and $\Delta K$ denote the two parameters of Paris' law yet to be determined and the amplitude of the stress intensity factor. Since the stress ratio was zero in this study, the amplitude of the stress intensity factor for the element is defined as

$$\Delta K = \beta\sigma_e\sqrt{\pi a_e}, \tag{3.9}$$

where $a_e$ denotes the equivalent crack length at the cycle $N$. The constant $\beta$ denotes a dimensionless correction factor reflecting the geometry of both the cracks and the structures. In this chapter, $\beta$ and $K_{\mathrm{Ic}}$ were set to be the same to Chapter II, i.e., 1.12 [23,75] and 1.1 $\mathrm{MPam}^{1/2}$ [75,82], respectively. When a specimen breaks, the stress intensity factor at the tip of the critical crack is expected to be equal to the toughness $K_{\mathrm{Ic}}$. The equivalent critical crack length is $a_{\mathrm{c}} = (K_{\mathrm{Ic}}/\beta\sigma\pi^{1/2})^2$. By substituting $\Delta K$ in Eq. (3.8) with Eq. (3.9) and then integrating Eq. (3.8) with respect to the crack length from $a_{0\mathrm{e}}$ to $a_{\mathrm{c}}$, the number of cycles $N$ required for the extension of cracks to the critical crack length can be obtained. From this calculation, the initial crack length $a_{0\mathrm{e}}$ is obtained as

$$a_{0\mathrm{e}} = \left(\frac{K_{\mathrm{Ic}}}{\beta\sigma k_e\sqrt{\pi}}\right)^2\left[1+\frac{C(n-2)}{2}\left(\frac{\beta\sigma k_e\sqrt{\pi}}{K_{\mathrm{Ic}}}\right)^2 N\right]^{2/(2-n)}. \tag{3.10}$$

Since the distribution of initial crack lengths can be evaluated from static strength distribution by modifying Eq. (3.2) with the correlation of stress to crack length $\sigma = K_{\mathrm{Ic}}/\beta(\pi a)^{1/2}$, the cumulative probability $F$ to contain an initial crack longer than $a_{\sigma 0}$ is formulated in terms of crack length as

$$F = 1-\exp\left[-\sum_e \gamma\left(\frac{a_{0\mathrm{e}}}{a_{\sigma 0}}\right)^{-m/2}\right], \tag{3.11}$$

where $a_{\sigma 0} = (K_{\mathrm{Ic}}/\beta\sigma_0\pi^{1/2})^2$ is a constant. Therefore, the cumulative fracture probability $F$ of the entire etched surfaces is formulated as a function of both the maximum stress

$\sigma$ in the specimen and the number of cycle $N$ as

$$F = 1 - \exp\left\{ -\left( \frac{\sigma}{\sigma_0} \right)^m \sum_e \gamma_e k_e^m \left[ 1 + \frac{C(n-2)}{2} \left( \frac{\beta \sigma k_e \sqrt{\pi}}{K_{\mathrm{Ic}}} \right)^2 N \right]^{m/(n-2)} \right\}. \quad (3.12)$$

When the number of cycles $N$ is 0 then Eq. (3.12) becomes identical to Eq. (3.3) showing the static strength distribution. From this equation, fatigue behavior of the specimens with arbitrary shapes can be estimated at arbitrary applied load levels.

The PDF corresponding to the cumulative fracture probability of Eq. (3.12) can be derived similarly in Chapter II as

$$f_{\mathrm{f}} = \begin{cases} \partial F / \partial \sigma & \text{when } N = 0 \\ \partial F / \partial N & \text{when } N > 0. \end{cases} \quad (3.13)$$

It corresponds to a static test in Eq. (3.12) when a specimen breaks at $N = 0$, i.e., the specimen breaks while the applied load is monotonically increasing for the first load cycle. In this case, the cumulative fracture probability depends only on the applied stress $\sigma$. Therefore, the PDF is simply defined by taking the derivative of the cumulative fracture probability with respect to $\sigma$. If the specimen still survives after the applied stress has reached to the stress amplitude then it should also survive until the end of the first cycle. This means that the specimen is not broken by the static load and enters the fatigue test regime. Because the applied stress amplitude is constant, the cumulative fracture probability of the specimen depends only on the number of load cycles. Therefore the PDF is defined by taking the derivative of the cumulative fracture probability with respect to $N$. The likelihood function of a set of observations $\{\sigma, N\}$ obtained from fatigue tests is presented in the form of natural logarithm as

$$\ln L_{\mathrm{f}} = \sum_{i=1}^{I} \ln f_{\mathrm{f}}(\sigma_i, N_i | C, n). \quad (3.14)$$

In the MLM, the best estimators of $C$ and $n$ satisfy the simultaneous equations

$$\begin{cases} \partial \ln L_{\mathrm{f}} / \partial C = 0 \\ \partial \ln L_{\mathrm{f}} / \partial n = 0 \end{cases} \quad (3.15)$$

and are thus found by solving these equations.

## 3.3. Evaluation of the strength and fatigue behaviors of specimens fabricated under the same conditions

### *3.3.1. Specimens and experiment*

The tensile test structure presented in Chapter II was utilized for the experiments in this chapter. For this study, three types of specimens with different shapes as shown in Fig. 3.2 were fabricated from polysilicon thin films under exactly the same etching condition, which was used to fabricate the specimens of Group C in Chapter II. Therefore, their etching damage distributions are expected to be similar. The films were patterned into parallel-sided specimens with and without notches, with the stress concentration factors 1.0, 3.3 and 10, respectively, in order to establish different stress distributions on the specimens. The three specimen geometries are named Types $C_{1.0}$, $C_{3.3}$ and $C_{10}$, where the capital letter C indicates the specimens were fabricated exactly in the same conditions of Group C in Chapter II, subscripts present the designed stress concentration factor of the specimen types. From here, "Group" indicates all the specimens fabricated under the same conditions, while "Type" indicates a specific shape of the specimens in a group. The specimen Type $C_{1.0}$ was designed without notch; its shape is similar to that of the specimens in the previous studies [75,92]. Types $C_{3.3}$ and $C_{10}$ were designed with a notch located in the middle of the specimens. The tensile stress along the etched surfaces of the specimens is shown in Fig. 3.3. The abscissa shows the distance from the middle points indicated in Fig. 3.2 toward both ends along the etched surfaces 1 and 2. Stress values are normalized by the average stress over a cross-section with 50 μm width and 1 μm thickness. These stress distributions were calculated using a finite element method (FEM) with the elements on the etched surfaces set to be squares with an area of 1 $\mu m^2$. The total area of the two etched surfaces of specimen Type $C_{1.0}$ indicated in Fig. 3.2(a) is set for the area $A_0$.

Figure 3.4 shows the experimental setup which was used for both the static fracture tests and the fatigue tests. The setup was located in an environmental chamber (ETAC TH441HA, accuracy: ±0.1°C and ±1%) with controlled temperature and humidity. The test structure was fixed to the holder and actuated by a piezo-positioner (PI P-841.20, travel: 30 μm, resolution: 0.6 nm). The applied load was recorded by a load cell PCB 209C2 (resolution: 0.09 mN, sensitivity: 538.9 mV/N, maximum

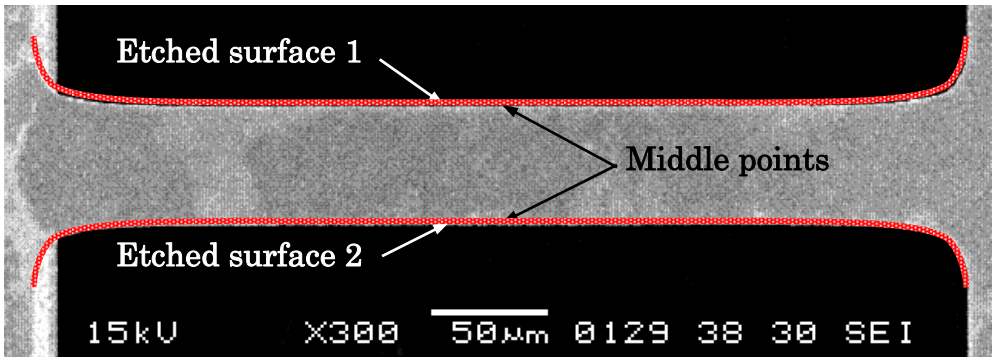


(a) Type $C_1$

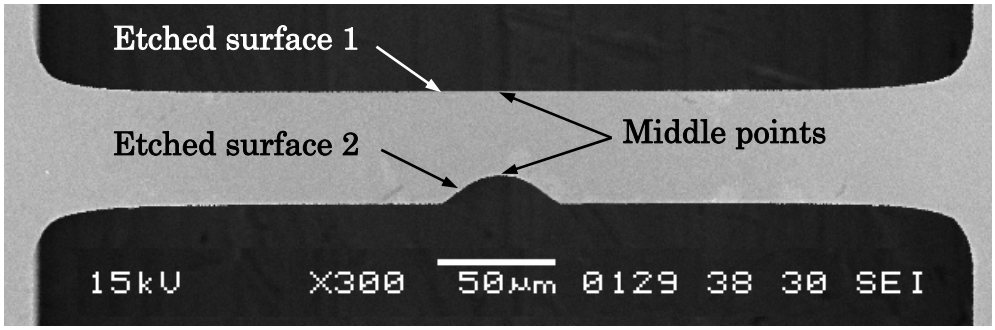


(b) Type $C_{3.3}$

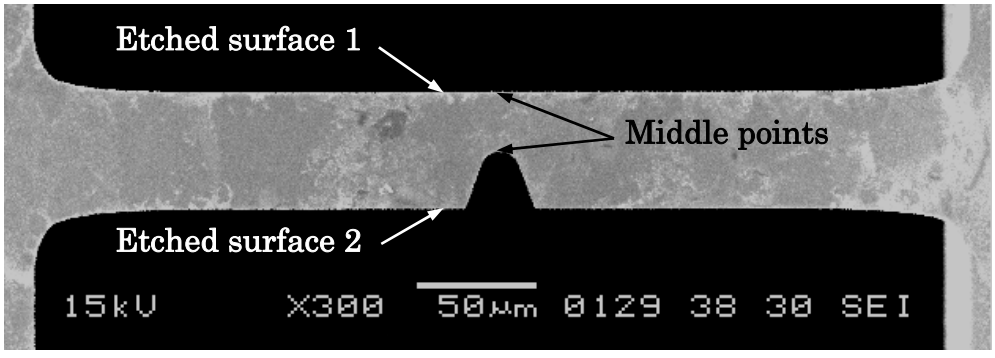


(c) Type $C_{10}$

**Fig. 3.2** Scanning electron micrograph of specimens.

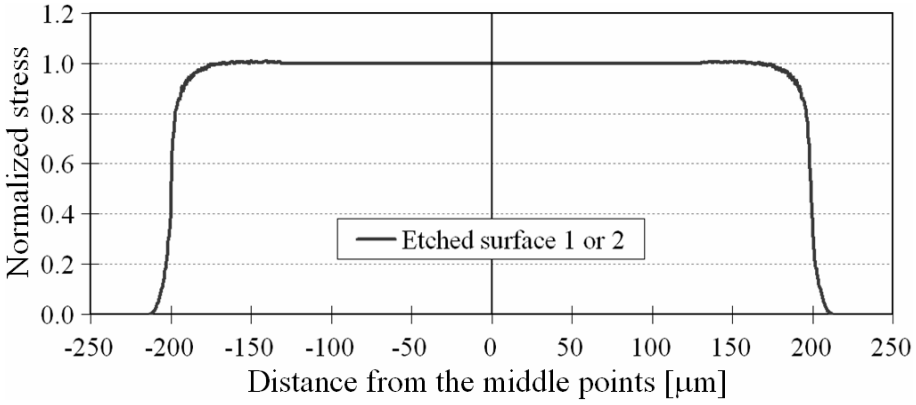


(a) Type A

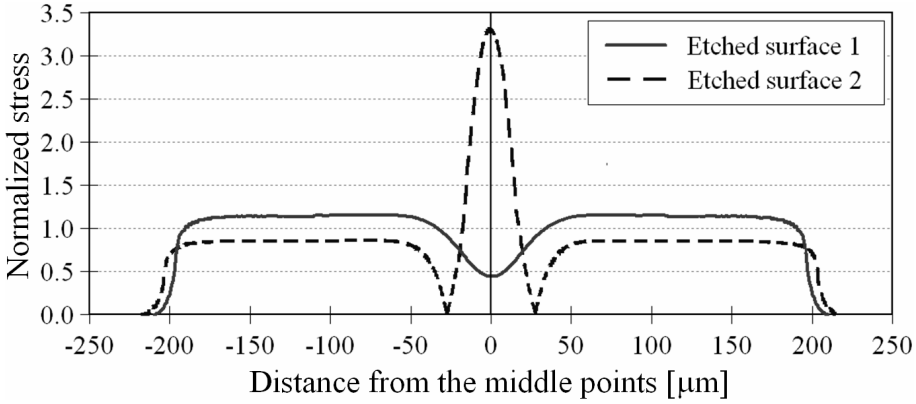


(b) Type B

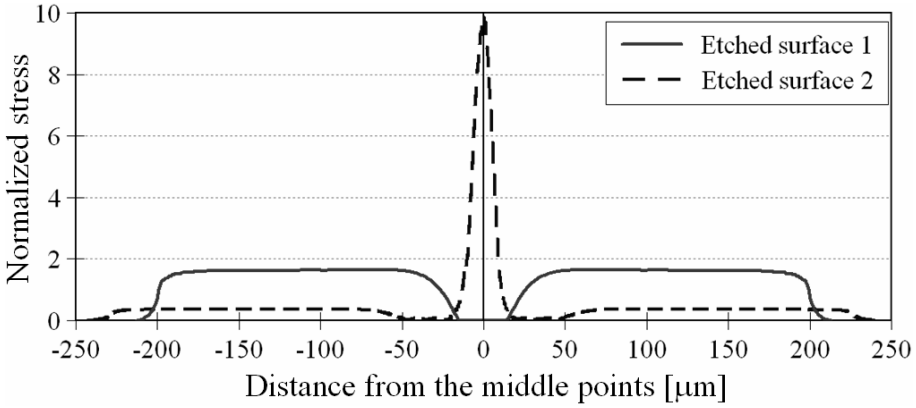


(c) Type C

**Fig. 3.3** Estimated stress distribution on the etched surfaces.

capacity: 48.9 N, stiffness: 350 N/μm), which was mounted on the tip of the actuator. The displacement of the inner frame was recorded by a laser displacement sensor (Anritsu, KL1300B, resolution: 5 nm, sampling frequency: 64 kHz) facing the test structure. The test structure was observed through a microscope during the tests. All equipment was driven from outside the chamber by a computer which also recorded the data from the actuator, load cell and laser displacement sensor. The overall view of the experimental system was similar to that presented in Fig. 2.4 of Chapter II.

The static strength tests were performed with monotonically increasing load under lab-air condition. The strain rate in the static tests was 0.15 μm/s. The results of static tests of three types of specimens are plotted in Fig. 3.5. The abscissa indicates the ranked number of the static test data from the weakest to the strongest sample in each type, and the ordinate indicates the maximum stress value along the distribution in Fig. 3.3 when the specimen broke.

The fatigue experiments were performed at 22°C and relative humidity of 80%. All the specimens were cyclically loaded between the common minimum of zero and maximum stress which was kept at a different constant value for each individual specimen. Therefore, the ratio of the minimum to the maximum stress (stress ratio) in the loading cycle was zero for all the specimens. The loading frequency was 500 Hz.

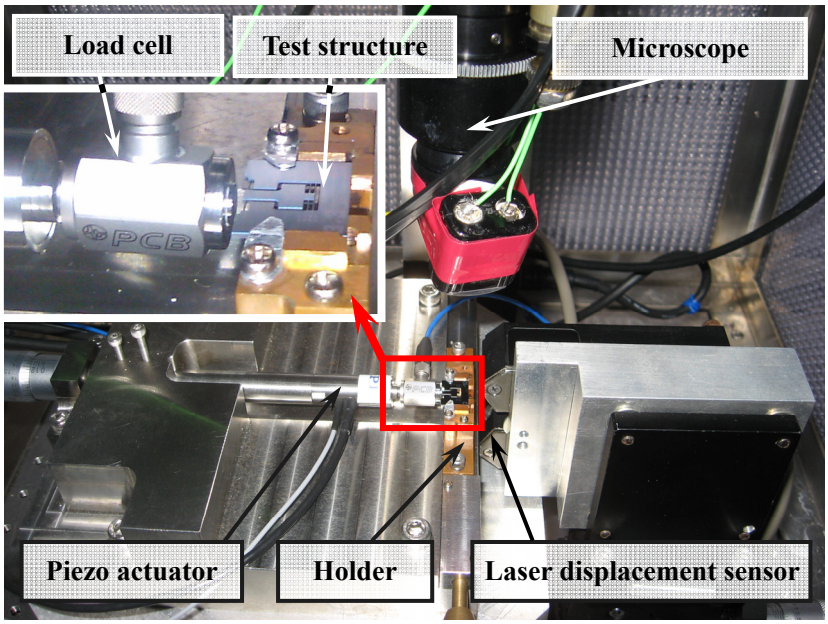


**Fig. 3.4** Experimental setup.

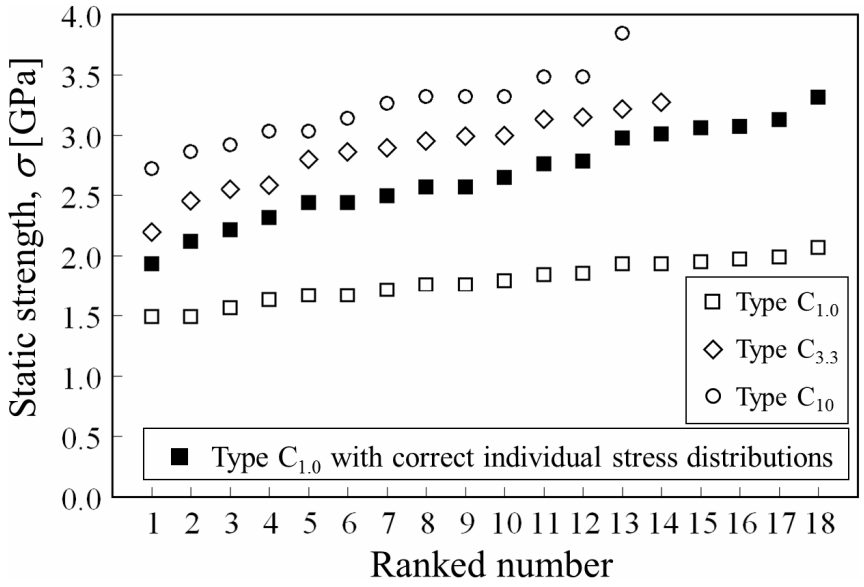


**Fig. 3.5** Static strength of three specimen types.

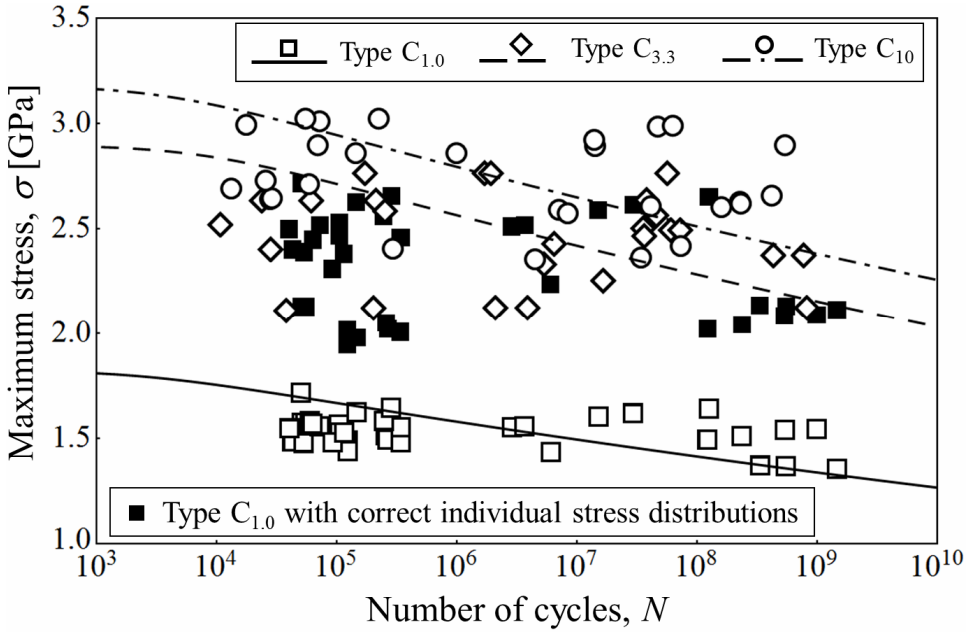


**Fig. 3.6** Results of fatigue tests performed at 22°C and 80%RH.

Further details of the methods to obtain static and fatigue test data were described in the previous papers [75,80]. Figure 3.6 shows the experimental results of the fatigue tests of the three types of specimens with the symbols. Each symbol presents the maximum stress applied to a specimen and fatigue lifetime in terms of the number of cycles at which fracture of the specimen occurred in the fatigue experiments. The

number of fatigue test data of Types $C_{1.0}$, $C_{3.3}$ and $C_{10}$ is 37, 26 and 28, respectively.

### *3.3.2. Estimation of parameters*

#### *3.3.2.1. Static test*

By applying Eq. (3.7) to the static test data and solving it, the best estimators of the two parameters $\sigma_0$ and $m$ were obtained for the individual types of the specimens as listed in Table 3.1. They are shown as the open symbols in Fig. 3.7. On the basis of the likelihood function, the likelihood ratio test was applied to estimate confidence bounds. They are calculated as [88,89]

**Table 3.1.** The best estimators of $\sigma_0$ and $m$

| Parameters | Type $C_{1.0}$ | Type $C_{3.3}$ | Type $C_{10}$ |
|---|---|---|---|
| $\sigma_0$ [GPa] | 1.84 | 2.05 | 2.00 |
| $m$ | 12.15 | 11.72 | 10.92 |

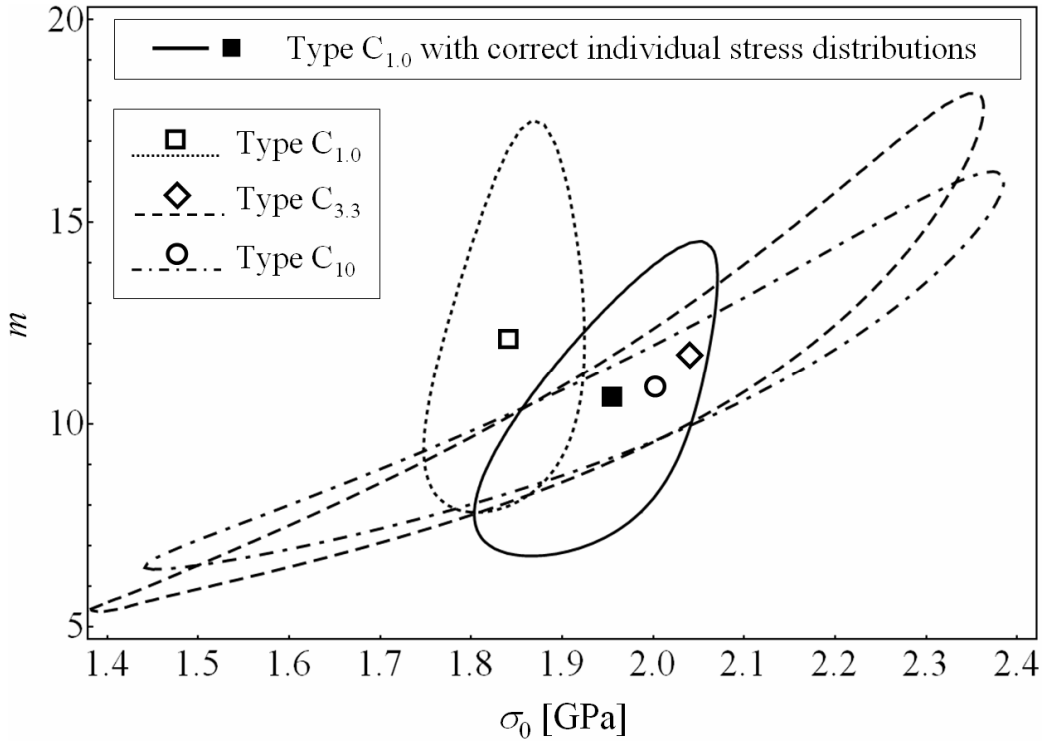


**Fig. 3.7** The best estimators and 90% confidence bounds of $\sigma_0$ and $m$.

$$-2\ln\left(\frac{L_1}{L_2}\right)=\chi^2_{\alpha,k}\,, \tag{3.16}$$

where $L_1$ is the likelihood function for the parameter values on the confidence bound, $L_2$ is the value of likelihood function with the parameter values estimated by the MLM. The right hand side $\chi^2_{\alpha,k}$ denotes the chi-square statistic with confidence level $\alpha$ and degrees of freedom $k$, where $k$ equals to the number of estimated parameters. The confidence bounds of the parameters $\sigma_0$ and $m$ of the three specimen types were drawn at a confidence level of 90% in Fig. 3.7 as the dashed contours. The distributions of $\sigma_0$ and $m$ of Types $C_{3.3}$ and $C_{10}$ in Fig. 3.7 are almost identical while that of Type $C_{1.0}$ lies in a different region. This means that the distribution of the local strength along the etched surfaces is expected to be statistically unique at least for Types $C_{3.3}$ and $C_{10}$. It also strongly suggests that the optimum values of $\sigma_0$ and $m$ of Types $C_{3.3}$ and $C_{10}$ are not markedly different despite the different shapes. In contrast, the local strength distribution obtained with Type $C_{1.0}$ specimens might be inconsistent with that of the other two types.

### *3.3.2.2. Fatigue test*

The values of $C$ and $n$ were estimated similarly by solving Eq. (3.15) applied to the fatigue test data. The values estimated with the individual types of specimens were obtained as listed in Table 3.2 and are shown in Fig. 3.8 as the open symbols. The best estimators of $n$ are consistent with the reported range of 40 to 50 for polysilicon films [86]. The dashed contours show the 90% confidence bounds of the parameters $C$ and $n$ estimated by the likelihood ratio test with Eq. (3.16). The results show that most of the distribution ranges of $C$ and $n$ obtained with Types $C_{3.3}$ and $C_{10}$ overlap with each other. In contrast, only a small portion of the distribution range of $C$ and $n$ obtained with Type $C_{1.0}$ lies within the 90% confidence bounds of Types $C_{3.3}$ and $C_{10}$ and vice versa. This means that the local characteristics of the etched surface is unique at least of Types $C_{3.3}$ and $C_{10}$ also for the case of the fatigue behavior; the optimum values of $C$ and $n$ of Types $C_{3.3}$ and $C_{10}$ are not markedly different. In contrast, those of Type $C_{1.0}$ might again be inconsistent with the other two types.

The fatigue test data plotted in Fig. 3.6 show a wide scatter of lifetime, and

**Table 3.2.** The best estimators of the Paris law parameters $C$ and $n$

| Parameters | Type $C_{1.0}$ | Type $C_{3.3}$ | Type $C_{10}$ |
|---|---|---|---|
| $C$ [m/cycle] | $1.91\times10^{-12}$ | $2.42\times10^{-13}$ | $3.94\times10^{-13}$ |
| $n$ | 41.63 | 39.48 | 43.09 |

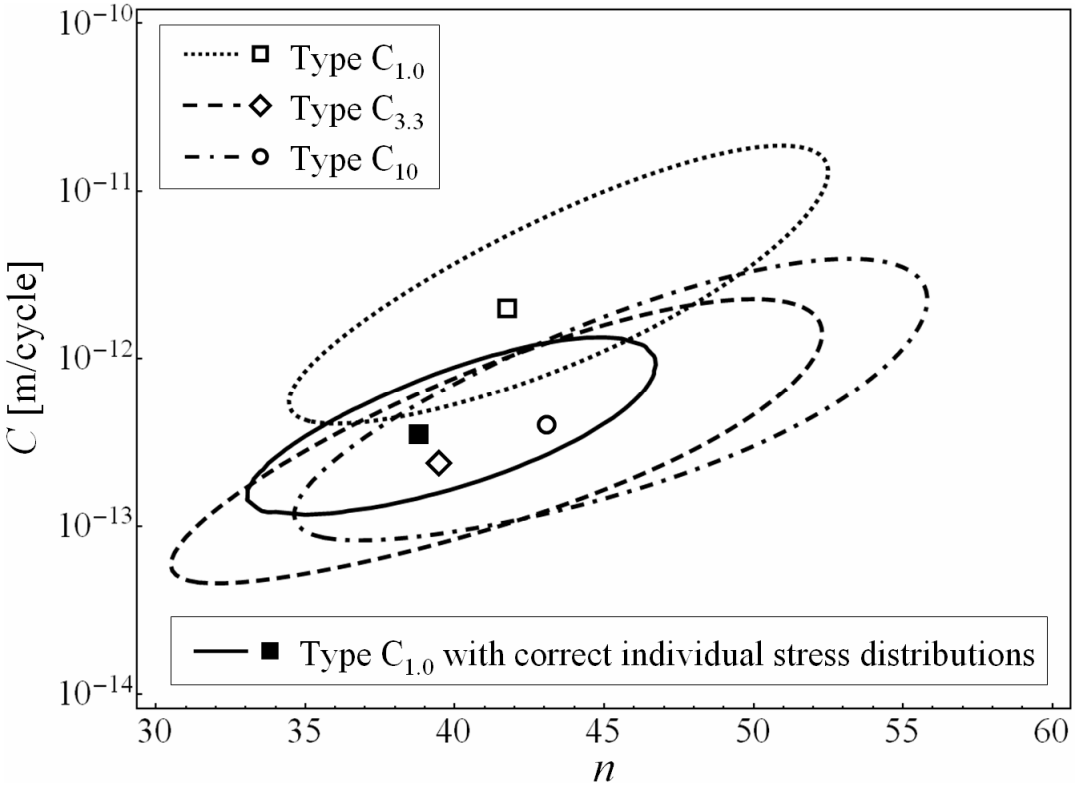


**Fig. 3.8** The best estimators and 90% confidence bounds of $C$ and $n$.

thus the correlation between the applied stress and fatigue lifetime is not clear. The large scatter of fatigue lifetime was explained in Chapter II where it was caused by the large scatter of initial crack lengths [92]. The difference in static strength was enlarged into the huge scatter in fatigue lifetime, which was well described by the model proposed in the previous chapter [92]. By using the parameter values in Table 3.2, stress-lifetime curves could be calculated by using Eq. (3.12). The stress-lifetime curves of the three specimen types with cumulative fracture probability $F$ = 0.5 plotted in Fig. 3.6 trace the trends of the correlation between the applied stress and fatigue lifetime for the three specimen types.

As mentioned in the Introduction however, since the three types of specimens were fabricated in the same conditions, the four parameters $\sigma_0$, $m$, $C$ and $n$ were expected to be independent of the shapes of specimens. In the next section, inferential statistics will be used to evaluate how markedly the parameter values extracted from the three specimen types are different.

### *3.3.3. Discussion*

Firstly, a hypothesis test was performed using inferential statistics to see how markedly the parameters $\sigma_0$, $m$, $C$ and $n$ of the three types differ. When the confidence bounds of the parameters start to overlap with each other with the same value of the confidence level, that confidence level is called the statistical difference level [89,97-99]. The statistical difference level could take a value ranging from 0 to 100%. If the statistical difference level is small, it can be concluded that there is no marked difference. In contrast, if the statistical difference level is large, one can conclude that there is a marked difference. The statistical difference levels of the parameters $\{\sigma_0,m\}$ in the static tests and $\{C,n\}$ in the fatigue tests of the three types are shown in Table 3.3. For the cases of the pair of Types $C_{1.0}$ and $C_{3.3}$, and the pair of Types $C_{1.0}$ and $C_{10}$, since the statistical difference levels of the parameters $\{\sigma_0,m\}$ and $\{C,n\}$ are close to 50%, it is difficult to draw any conclusion. For the case of Types $C_{3.3}$ and $C_{10}$, since the statistical difference levels are smaller than 10%, it is concluded that the estimated values of the parameters of Types $C_{3.3}$ and $C_{10}$ are not markedly different.

To survey the origin of this discrepancy seamingly setting Type $C_{1.0}$ apart from Types $C_{3.3}$ and $C_{10}$, stress distributions in the test specimens were further investigated in detail. The gap between the outer and inner frames in a structure was designed with a nominal width of 400 μm. The length of the specimens was originally designed to precisely fit this gap. However, it was difficult to fabricate the gap with exactly the designed dimension. This was because the slight taper of the etched surface implying the progressive widening of the gap as the substrate is being etched through from the rear. Figure 3.9 presents the tested specimens of the three types. In Fig. 3.9(a) the dashed lines indicate the specimen shape of the type $C_{1.0}$ specimens before the test. The distance from the edge of the gap to the edge of the anchor part of a specimen is called the overetch distance. For these specimens, this distance was observed to lie in

**Table 3.3.** The statistical difference levels of the parameters between the three specimen types

| Parameters | Types $C_{1.0}$ and $C_{3.3}$ | Types $C_{1.0}$ and $C_{10}$ | Types $C_{3.3}$ and $C_{10}$ |
|---|---|---|---|
| $\{\sigma_0, m\}$ | 54.8% | 50.1% | 3.4% |
| $\{C, n\}$ | 53.7% | 51.4% | 6.9% |

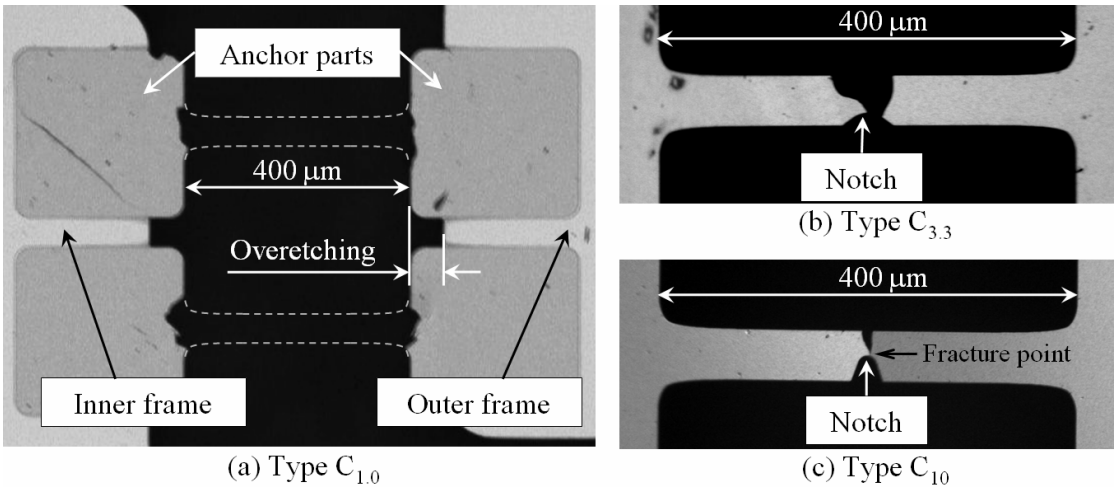


**Fig. 3.9** Optical micrographs of the broken specimens after the tests, where the specimens of (a) Type $C_{1.0}$ broken close to the specimen suspensions due to overetching during their fabrication, while specimens of (b) Type $C_{3.3}$ and (c) Type $C_{10}$ broken at the notches.

the range from 20 μm to 60 μm. The overetching was taken into account in the FEM calculation to analyse its impact on the stress distribution on the specimen Type $C_{1.0}$. Results are shown in Fig. 3.10. Figure 3.10(a) shows the stress distribution on the etched surface normalized by the nominal stress when the overetch distance was set as 0 μm and 40 μm. Figure 3.10(b) shows the stress concentration factor calculated as a function of overetch distance from 0 μm to 60 μm. They clearly show that the maximum value in the stress distribution increases when overetching increases. From this result, the actual stress concentration factor of specimens of Type $C_{1.0}$ was expected to range from 1.2 to 1.6 in view of the range of the observed overetch distances. Besides, the position of maximum stress was found to be different with different values of overetching. When overetching was 0 μm, the position of

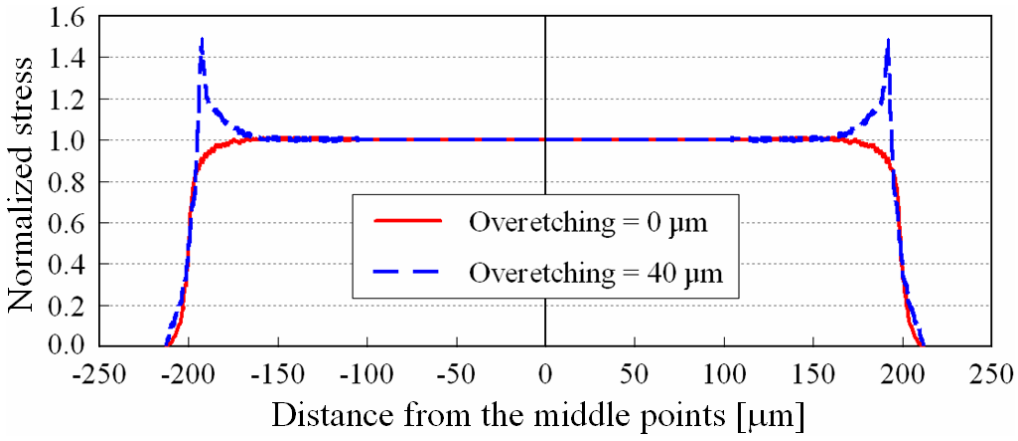


(a)

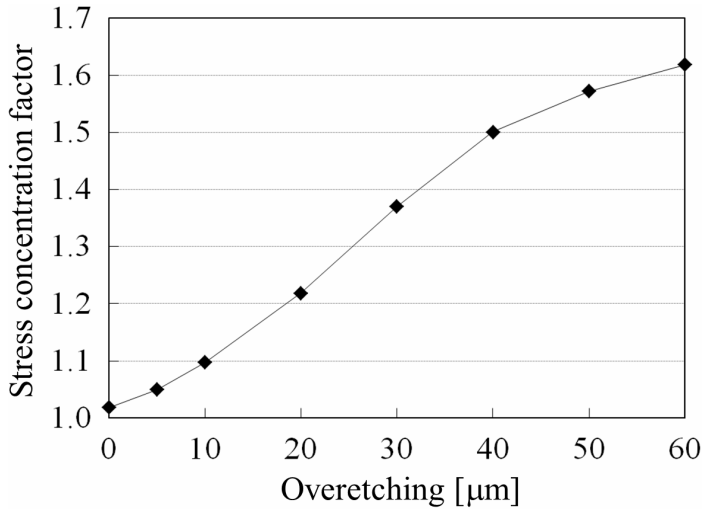


(b)

**Fig. 3.10** Effect of overetching on the stress distribution on specimens of Type $C_{1.0}$. (a) Stress distributions when the overetching was 0 μm and 40 μm. (b) Stress concentration factor versus the overetching of specimen. The line segments are guides to the eye.

maximum stress was at about 110 μm from the middle points. When overetching was 40 μm, it was at about 190 μm from the middle points, i.e., close to the anchor part of specimen. Therefore, in the case of large overetching, specimens will likely break close to the anchor part as shown in Fig. 3.9(a) for an example with 60 μm of overetching. When the true value of the stress concentration factor of Type $C_{1.0}$ was not taken into account, i.e., the stress concentration factor was kept to be 1.0, the

calculated static strength becomes smaller and the rate of crack extension reflected in $C$ becomes larger. This explanation is consistent with the estimated parameters, where the value of $\sigma_0$ of Type $C_{1.0}$ was smaller than those of Types $C_{3.3}$ and $C_{10}$, and the value of $C$ of Type $C_{1.0}$ was larger than those of Types $C_{3.3}$ and $C_{10}$. Likely the observations made here are also applicable to the previous studies [75,92], where the specimens had the same shape and size as Type $C_{1.0}$. This is possibly a reason why the estimated values of the parameters $C$ and $n$ in those reports and Chapter II showed a broad scatter, i.e., $C$ range from $1.43\times10^{-13}$ m/cycle to $1.45\times10^{-12}$ m/cycle and $n$ ranged from 18 to 40 [75,92]. For the cases of Types $C_{3.3}$ and $C_{10}$, when overetching changed, there also was a change in stress distribution at the flare part of the specimens. However, the stress value at the flare part is much smaller than that at the notch tip. Therefore the maximum stress value in the notched specimens did not change and the position always remained at the peak of the notch. From the consideration above, it is expected that the results obtained with the notched specimens are not significantly distorted by the overetching and thus are close to their true values. Figures 3.9(b) and 3.9(c) show clearly that the specimens of Types $C_{3.3}$ and $C_{10}$ broke at the notches corresponding to the position of the high stress region. Note that the actual fracture point would not be exactly at the notch root, because it is determined by the probability. Though the specimens tend to break into pieces, the fracture origin must be unique and it may bifurcate during extension when catastrophic fracture happens. With the high stress concentration at the notch root of Type $C_{10}$ specimens, the crack surfaces were often preserved after the tests and therefore fractography analysis can be performed as presented in the next section.

In order to include the effect of overetching in the evaluation of the parameters for Type $C_{1.0}$, stress distributions of the individual specimens calculated by FEM due to their overetchings were carefully taken into account. In this case, since the stress distribution of each specimen with its individual overetch length is different, the specimens belong to different types with different strength levels; thus the optimum values of the Weibull and Paris' law parameters are estimated using combined likelihood functions. The experimental data of Type $C_{1.0}$ with the corrected stress distributions are plotted in Figs. 3.5 and 3.6 with symbols denoted as "Type $C_{1.0}$ with correct individual stress distributions". The fluctuation width of the static strength of the corrected data of Type $C_{1.0}$ is not much different from that of Types $C_{3.3}$ and $C_{10}$.

The best estimators of the parameters $\sigma_0$, $m$, $C$ and $n$ were obtained as 1.95 GPa, 11.03, $3.31\times10^{-13}$ m/cycle and 38.81, respectively. These estimated values and their 90% confidence bounds are shown in Figs. 3.7 and 3.8 as the solid symbols and solid contours. The statistical difference levels of the parameters $\{\sigma_0,m\}$ and $\{C,n\}$ between Types $C_{1.0}$ and $C_{3.3}$, and between Types $C_{1.0}$ and $C_{10}$ were estimated again. Results are shown in Table 3.4. The statistical difference levels are now much smaller than in Table 3.3. This suggests that the estimated values of the parameters of Type $C_{1.0}$ structures with correct individual stress distributions are not markedly different from those of the other specimen types. It also proves that the wide difference in $\sigma_0$ as well as $C$ between Type $C_{1.0}$ and other types was caused by overetching which led to the change of stress distribution on the specimens of Type $C_{1.0}$ from the initially assumed ideal distribution.

Based on the above observation, when the corrected stress distributions are taken into account, one may expect that the parameter values should represent the unique local characteristics of the etched surface. The fracture strength and fatigue behaviors of each specimen type should therefore be reasonably described with the same values of the four parameters. The optimum values of the parameters $\sigma_0$, $m$, $C$ and $n$ were obtained by using simultaneously the experimental data of all the specimen types. The best estimators are 2.01 GPa, 11.12, $3.36\times10^{-13}$ m/cycle and 41.06, respectively. The cumulative fracture probability $F$ in Eq. (3.12) was calculated and plotted in Fig. 3.11 for Types $C_{3.3}$ and $C_{10}$ as a function of both the applied stress and the number of cycles in order to present the full picture of the fatigue behavior. The fatigue test data were ranked from the longest to the shortest initial crack lengths

**Table 3.4.** The statistical difference levels of the parameters with the stress distributions of the individual specimens of Type $C_{1.0}$ taken into account

| Parameters | Types $C_{1.0}$ and $C_{3.3}$ | Types $C_{1.0}$ and $C_{10}$ |
|---|---|---|
| $\{\sigma_0, m\}$ | 9.1% | 3.8% |
| $\{C, n\}$ | 10.4% | 22.6% |

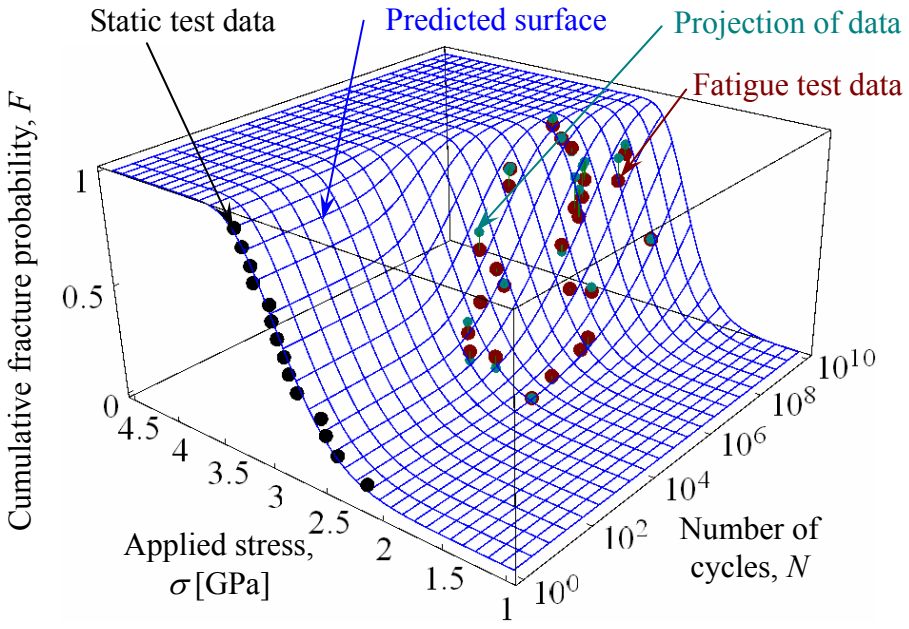


(a) Type $C_{3.3}$

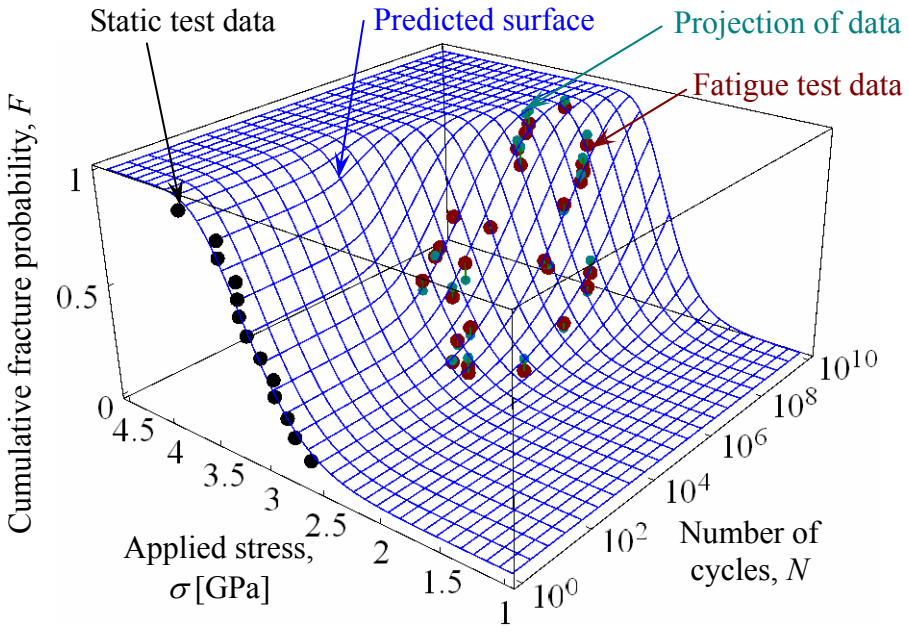


(b) Type $C_{10}$

**Fig. 3.11** Three-dimensional plot of the calculated behavior of (a) Type $C_{3.3}$ and (b) Type $C_{10}$ using the combined best estimators of $m$, $\sigma_0$, $C$ and $n$ obtained from Types $C_{3.3}$ and $C_{10}$.

calculated using Eq. (3.10). The calculated surface describes very well the distributions of static and fatigue test data with the same values of parameters despite the different specimen shapes. This fact suggests that the strength distribution and fatigue behavior of structures with arbitrary shapes can be practically estimated on the basis of the unique local characteristics of the etched surface represented by these four parameters, provided that the conditions of etching, operating stress ratio and environment are the same.

## 3.4. Prediction of fatigue lifetime of specimens fabricated under different etching conditions

### *3.4.1. Specimens and experiment*

Since the effect of overetching on the stress distribution on the flat specimens was found, the shape of specimens was redesigned in order to avoid that effect. Figure 3.12 presents the newly designed specimens with and without notches, where the shape of Type $C_{1.0}$ specimen is shown by dashed lines in Fig. 3.12(a). The width and length of the testing part of the specimens are 50 μm and 400 μm, respectively. The specimens without and with a notch were designed to have stress concentration factor of 1.0 and 3.0, respectively. The maximum principal stress distribution on the specimen without a notch is shown in Fig. 3.13 when the overetching was 40 μm, and the applied load was 80 mN. For this case, the maximum stress position still is at the middle part of the specimen, where stress concentration factor was 1.02. It means that the effect of overetching was negligible and could be avoided. Stress distribution on the etched surfaces of these specimens was calculated and plotted in Fig. 3.14, where the abscissa shows the distance from the middle points indicated in Fig. 3.12 toward both ends along the etched surfaces 1 and 2, and the ordinate shows the normalized stress which is the stress values normalized by the average stress over a cross-section with 50 μm width and 1 μm thickness.

For this study, two groups of specimens were newly fabricated from polysilicon thin films by using the two different etching recipes. One group was etched with RIE process and named as Group D. One other group was etched with

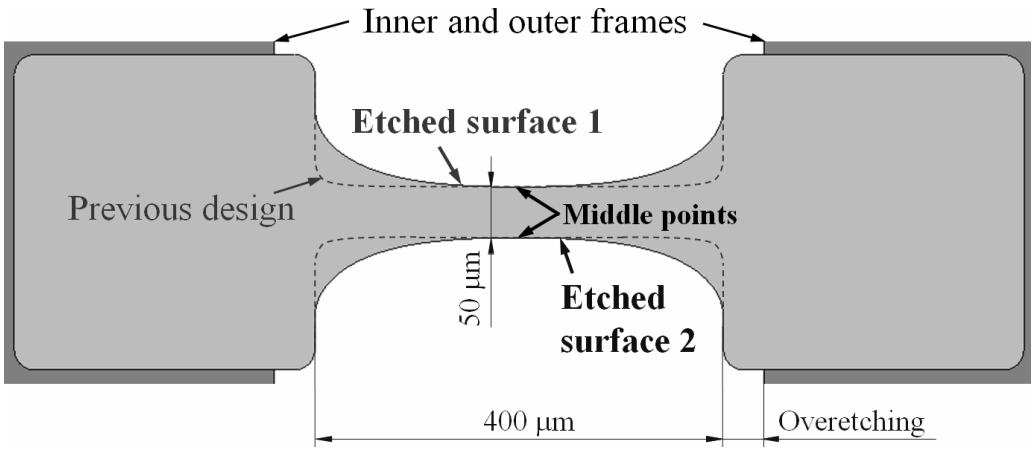


(a)

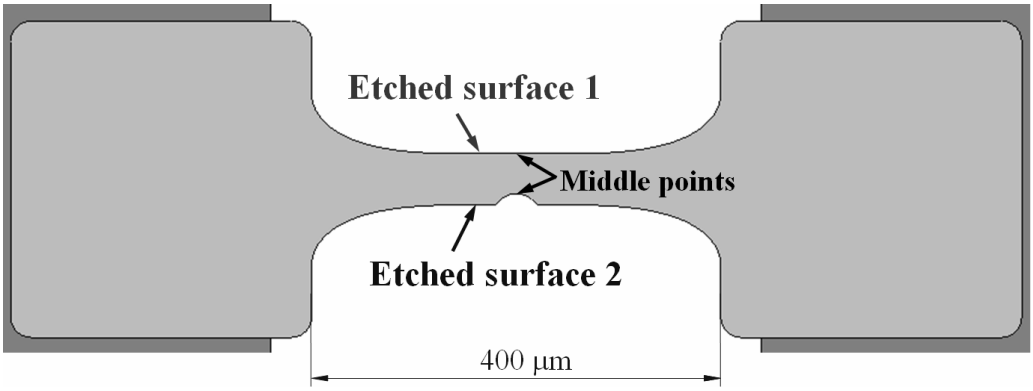


(b)

**Fig. 3.12** Newly designed specimens (a) without a notch and (b) with a notch.

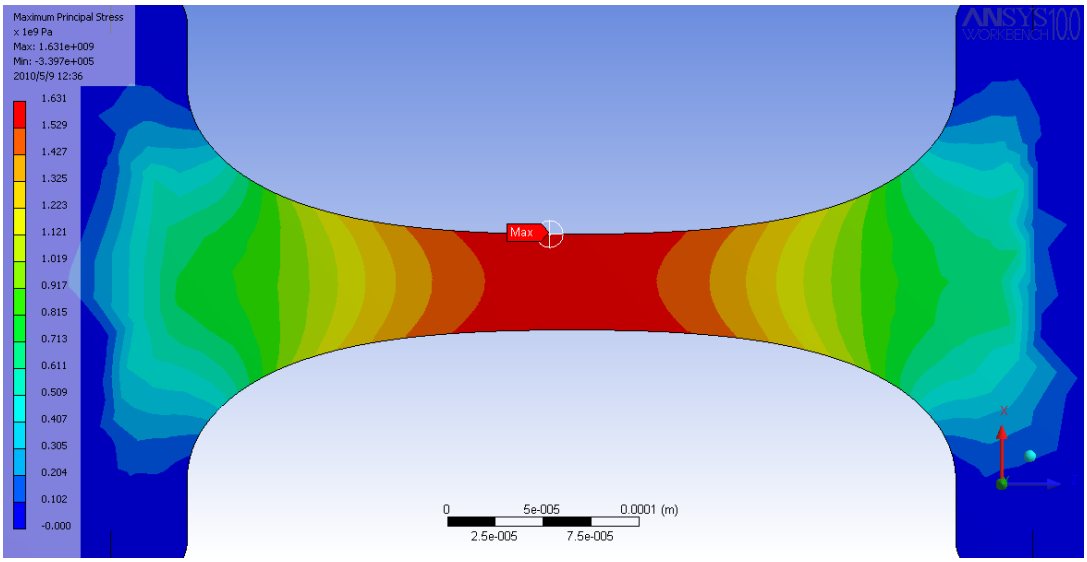


**Fig. 3.13** Maximum principal stress distribution on the newly designed specimen without a notch when overetching was 40 µm.

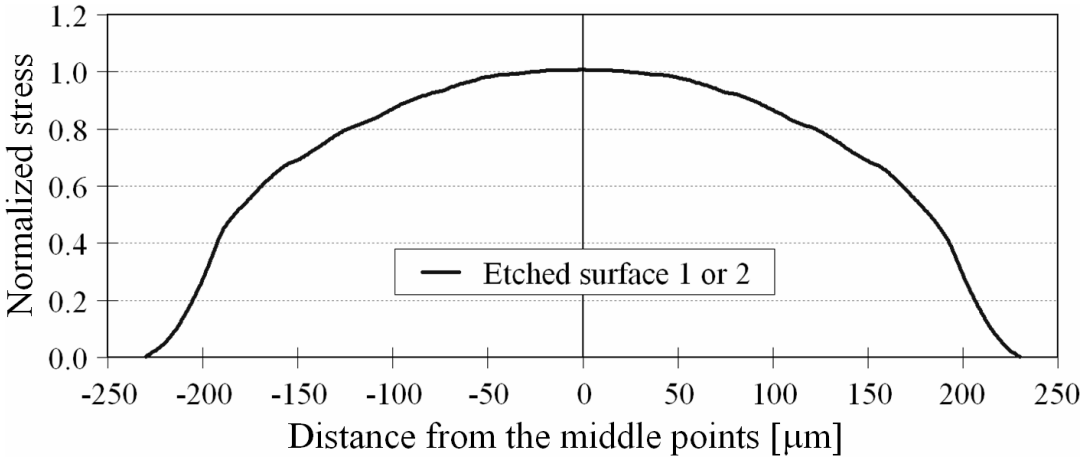


(a)

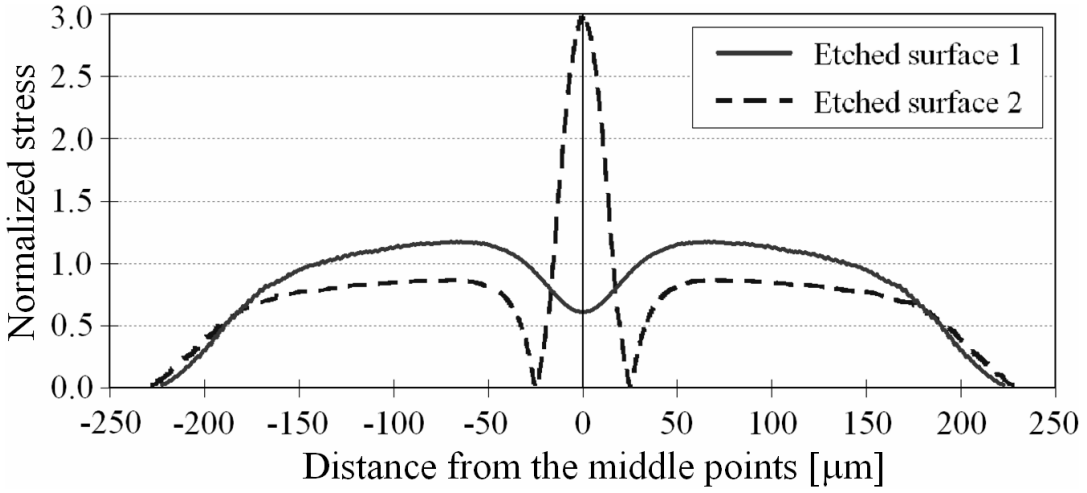


(b)

**Fig. 3.14** Stress distribution on the etched surfaces of the newly designed specimens (a) without a notch and (b) with a notch.

Bosch process and named as Group E. The recipes of these etching processes were the same to those presented in Chapter II and shown in Table 2.1. The average thickness and the fluctuation range of the thicknesses of these polysilicon films is 970±8 nm. For each group, the two newly designed specimen types with and without a notch as explained before were fabricated. The specimens are then named Types $D_{1.0}$, $D_{3.0}$, $E_{1.0}$ and $E_{3.0}$, where capital letter and subscript indicates the group of specimen and stress concentration factor, respectively. Table 3.5 summarizes the information of the groups and types of the specimens used in this chapter.

**Table 3.5.** Summarization of the groups and types of the specimens in Chapter III

| Group | Specimen type | Stress concentration factor | Average thickness | Etching process | Year of Fabrication |
|---|---|---|---|---|---|
| C | $C_{1.0}$ | 1.2 ~ 1.6 | 996 nm | Bosch | 2008 |
| | $C_{3.3}$ | 3.3 | | | |
| | $C_{10}$ | 10 | | | |
| D | $D_{1.0}$ | 1.0 | 966 nm | standard RIE | 2011 |
| | $D_{3.0}$ | 3.0 | | | |
| E | $E_{1.0}$ | 1.0 | 970 nm | Bosch | 2011 |
| | $E_{3.0}$ | 3.0 | | | |

Figure 3.15 presents the experimental setups. They were used for both the static fracture and the fatigue tests with the newly designed specimens. Overall view of the system is shown in Fig. 3.15(a) with the equipments controlling the tests. The environmental chamber (ETAC TH441HA, accuracy ±0.1°C and ±1%) with controlled temperature and humidity contains the two setups shown in Fig. 3.15(b) running in parallel. The two setups were controlled from outside of the chamber by the equipments shown in Fig. 3.15(a). By using these two setups, two test structures could be examined simultaneously in order to increase the number of experimental data as well as reduce the time for experiment. In each setup, a test structure was fixed to the holder and actuated by the piezo-positioners PI P-841.10. The two piezo-positioners in the two setups were controlled by a function generator WF1943A. The applied load was recorded by a load cell PCB 219B (sensitivity 10.12 pC/kN, maximum capacity 44.5 N, stiffness 350 N/μm) in the setup 1 and a load cell PCB 209C2 (sensitivity 494.6 mV/kN, maximum capacity 48.9 N, stiffness 350 N/μm) in the setup 2. The two laser displacement sensors (Anritsu, KL1300B) were used to record the displacement of the inner frames.

By using these experimental setups, the static strength and fatigue tests of the newly designed specimens were performed with the same conditions as those used for the previous specimens. The results of static and fatigue tests of three types of the specimens of Groups D and E are plotted as the solid and open symbols in Figs. 3.16

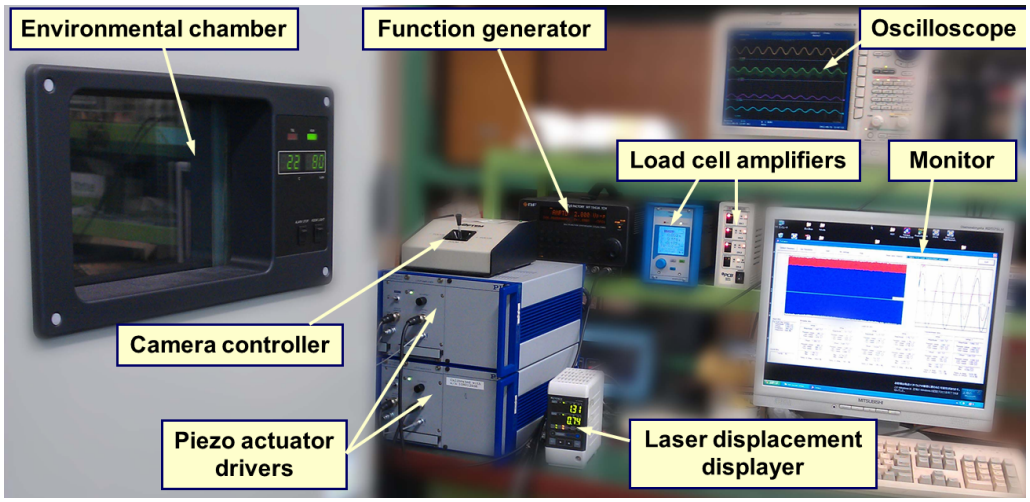


(a)

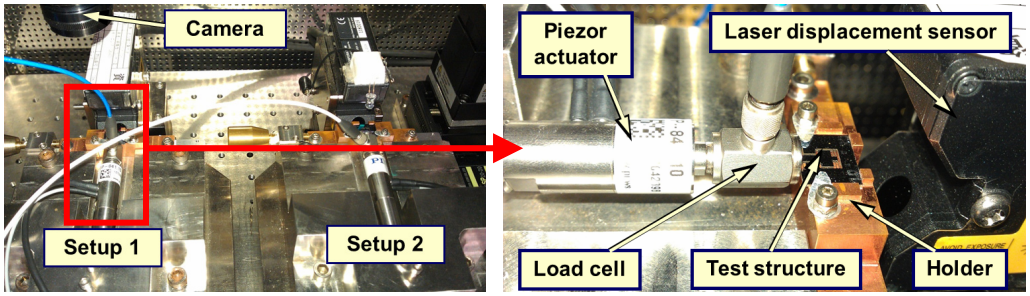


(b)

**Fig. 3.15** (a) Overall an (b) close-up views of experimental setups.

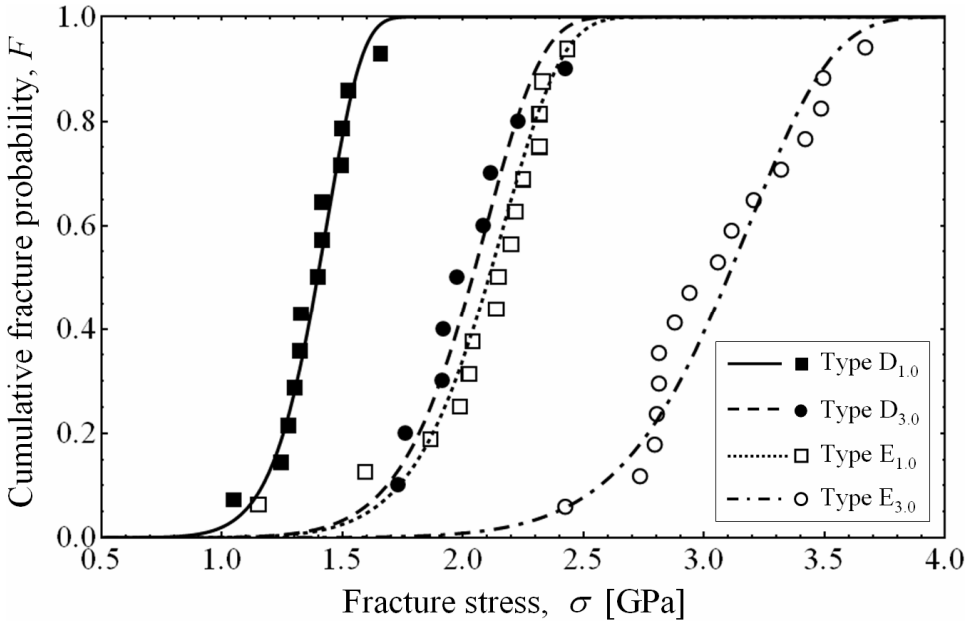


**Fig. 3.16** Static strength test results of the newly designed specimens.

and 3.17, respectively. Since the number of specimens was limited, fatigue test was not performed with the specimens of Type $D_{3.0}$. The data numbers of those tests for each specimen type are summarized in Table 3.6.

### *3.4.2. Static strength evaluation*

By applying Eq. (3.7) to the static test data of the newly designed specimens and solving it, the best estimators of the two parameters $\sigma_0$ and $m$ of an infinitesimal area on the etched surface were obtained for the individual types as listed in Table 3.7. The fitting results are presented in Fig. 3.16 as the curvilinear lines. The best estimators are plotted as the symbols in Fig. 3.18 together with their 90% confidence

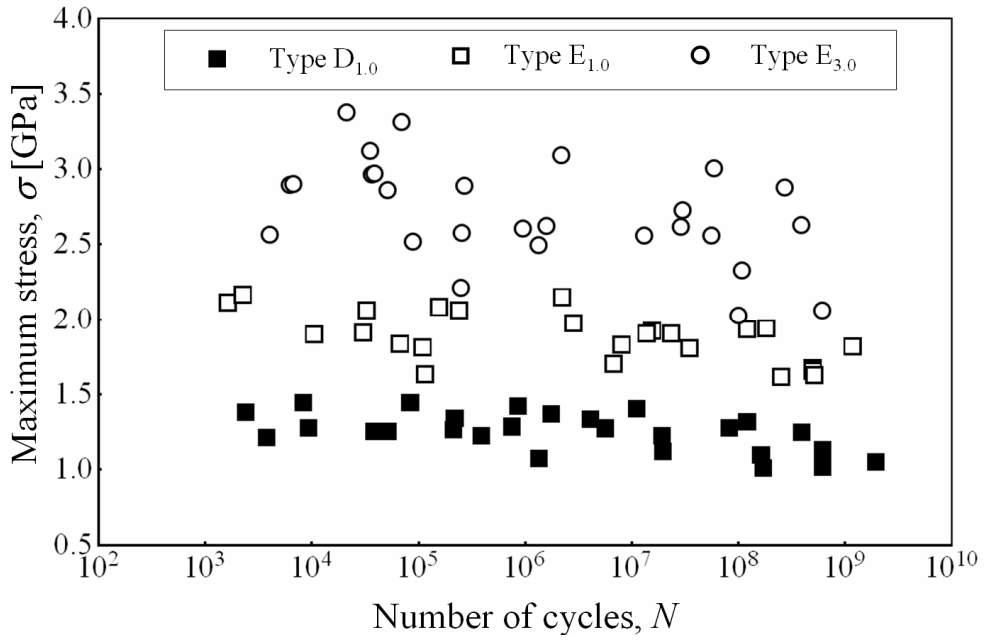


**Fig. 3.17** Fatigue test data of the newly designed specimens.

**Table 3.6.** Summarization of the data number

| | Type $D_{1.0}$ | Type $D_{3.0}$ | Type $E_{1.0}$ | Type $E_{3.0}$ |
|---|---|---|---|---|
| Static test | 14 | 9 | 15 | 16 |
| Fatigue test | 27 | – | 25 | 27 |

bounds in the space of $\sigma_0$ and $m$. The distributions of $\sigma_0$ and $m$ show that those of each group are close to each other. The statistical difference levels of the parameters $\{\sigma_0,m\}$ were also calculated for the specimen types in each group. The statistical difference level between Types $D_{1.0}$ and $D_{3.0}$ and between Types $E_{1.0}$ and $E_{3.0}$ is 4.5% and 1.6%, respectively. These values show that there is no marked difference of those parameters between the specimen types fabricated in the same conditions. The difference in $\sigma_0$ between the two groups corresponds to the difference of local strength levels, which was induced by different etching conditions. It is confirmed again that the values of the parameters $\sigma_0$ and $m$ of the specimens fabricated in the

**Table 3.7.** The best estimators of $\sigma_0$ and $m$ of the newly designed specimens

| Parameters | Type $D_{1.0}$ | Type $D_{3.0}$ | Type $E_{1.0}$ | Type $E_{3.0}$ |
|---|---|---|---|---|
| $\sigma_0$ [GPa] | 1.31 | 1.32 | 1.97 | 2.02 |
| $m$ | 10.57 | 9.86 | 9.67 | 10.03 |

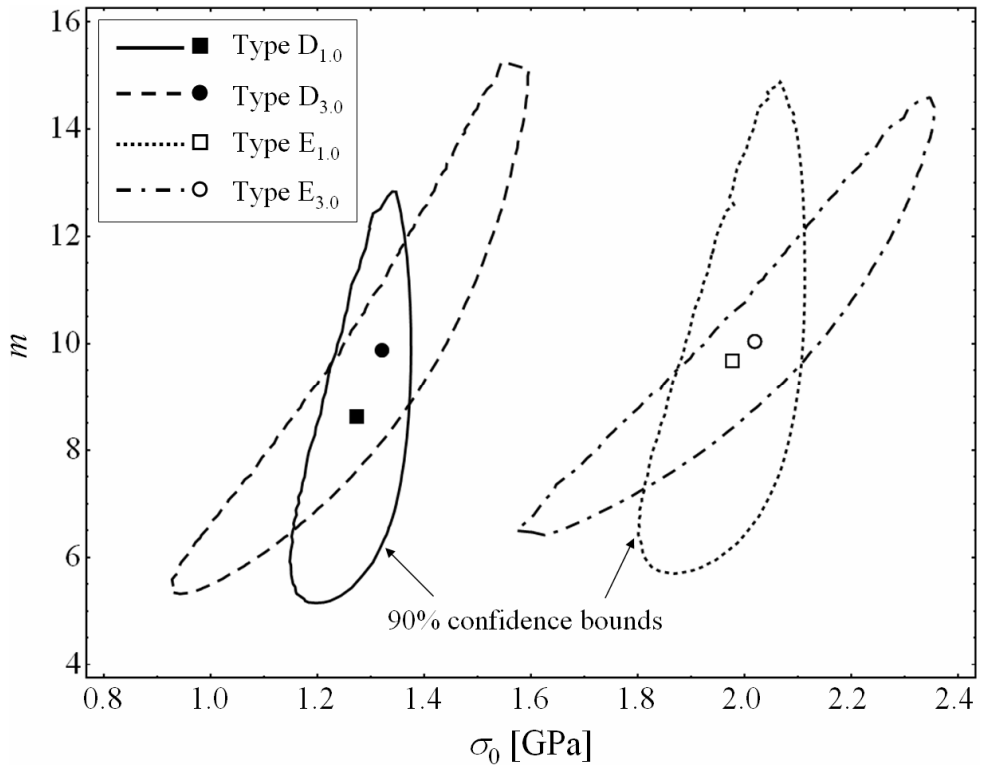


**Fig. 3.18** The best estimators and 90% confidence bounds of $\sigma_0$ and $m$ of the newly designed specimens.

same conditions are independent of the shapes of the specimens. Therefore, local characteristics of the etched surface of polysilicon thin films are unique.

### *3.4.3. Fatigue lifetime prediction and discussion*

By using the common optimum values the parameters *C* and *n* obtained from Group C, i.e., $3.36\times10^{-13}$ m/cycle and 41.06, respectively, the cumulative fracture probability *F* under fatigue loading was calculated by Eq. (3.12) and plotted in Fig. 3.19 for Types $D_{1.0}$, $E_{1.0}$ and $E_{3.0}$ as a function of both the applied stress and the number of cycles in comparison to the experimental data. The parameters $\sigma_0$ and *m* in these calculations were taken with the values presented in Section 3.4.2 for the individual types. The calculated surface describes very well the distributions of static and fatigue test data. This fact suggests that the fatigue behavior of structures with arbitrary shapes can be practically estimated on the basis of the unique set of the parameters *C* and *n* despite the difference in strength levels.

In order to investigate the accuracy of the prediction, the fitted distribution of fatigue test data was performed and then was compared to the predicted distribution. By fitting Eq. (3.12) to the fatigue test data of Types $D_{1.0}$ , $E_{1.0}$ and $E_{3.0}$ with the MLM, the optimum values of *C* and *n* were obtained as shown in Table 3.8. Those optimum values are plotted in Fig. 3.20 as the open symbols together with their 90% confidence bounds as the dashed contours. In this figure, the optimum values of *C* and *n* of Types $C_{1.0}$, $C_{3.3}$ and $C_{10}$ are also presented as the gray solid symbols. The common optimum values of *C* and *n* of Group C, i.e., common of Types $C_{1.0}$, $C_{3.3}$ and $C_{10}$, and its 90% confidence bound are shown as the asterisk and solid contour. Figure 3.20 shows clearly that all the optimum points are now inside of all the 90% confidence bounds. Besides, the statistical difference levels between the distribution of *C* and *n* of the common case of Group C and those of Types $C_{1.0}$, $C_{3.3}$ and $C_{10}$ were also calculated and were obtained as 23.6%, 12.5% and 1.3%, respectively. These results show that the values of *C* and *n* of Types $D_{1.0}$ , $E_{1.0}$ and $E_{3.0}$ are not markedly different from those of Group C. Therefore, it could be concluded that the values of *C* and *n* of polysilicon thin films are inherent material constants despite the difference of the specimen shapes and etching conditions.

The accuracy of the fatigue lifetime prediction of Types $D_{1.0}$ , $E_{1.0}$ and $E_{3.0}$

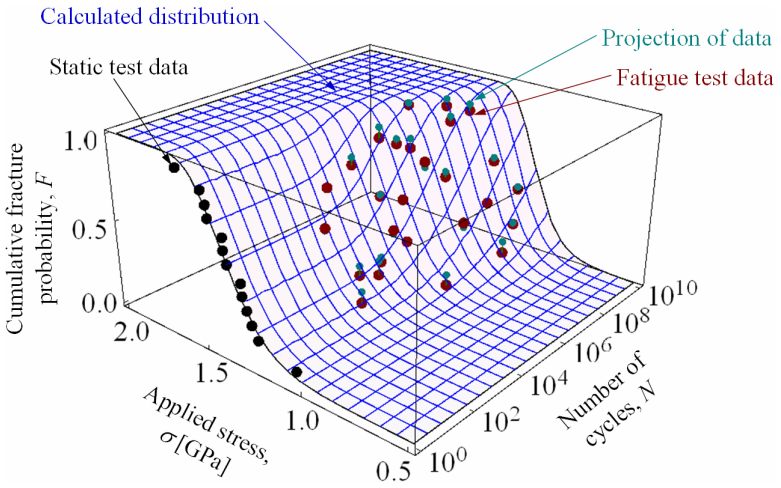


(a)

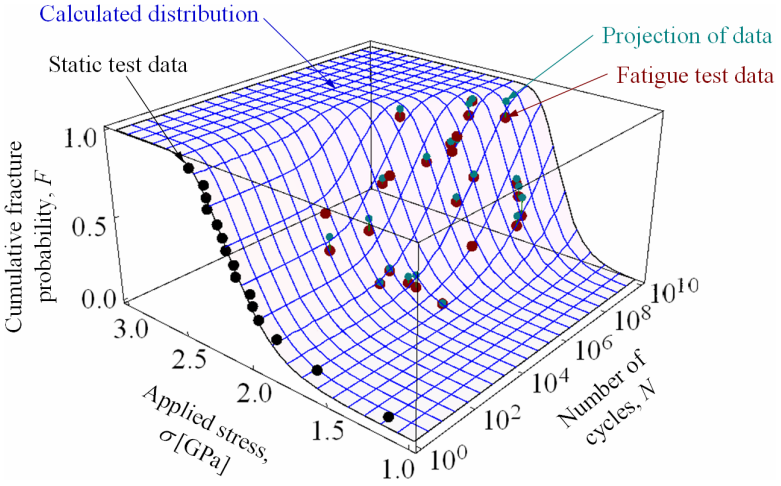


(b)

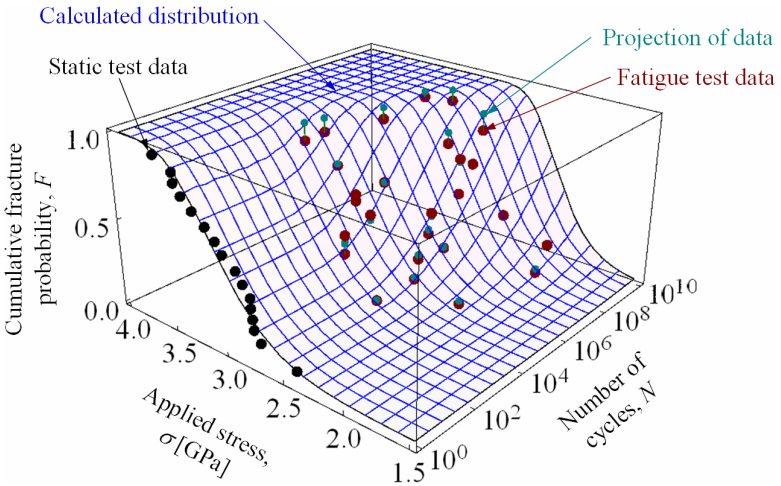


(c)

**Fig. 3.19** Plots of the calculated behavior of (a) Type $D_{1.0}$, (b) Type $E_{1.0}$ and (c) Type $E_{3.0}$ using the combined best estimators of $C$ and $n$ obtained from Group C.

**Table 3.8.** The best estimators of $C$ and $n$ obtained from the newly designed specimens

| Parameters | Type $D_{1.0}$ | Type $E_{1.0}$ | Type $E_{3.0}$ |
|---|---|---|---|
| $C$ [m/cycle] | $7.40\times10^{-13}$ | $6.79\times10^{-13}$ | $3.18\times10^{-13}$ |
| $n$ | 41.25 | 42.70 | 39.55 |

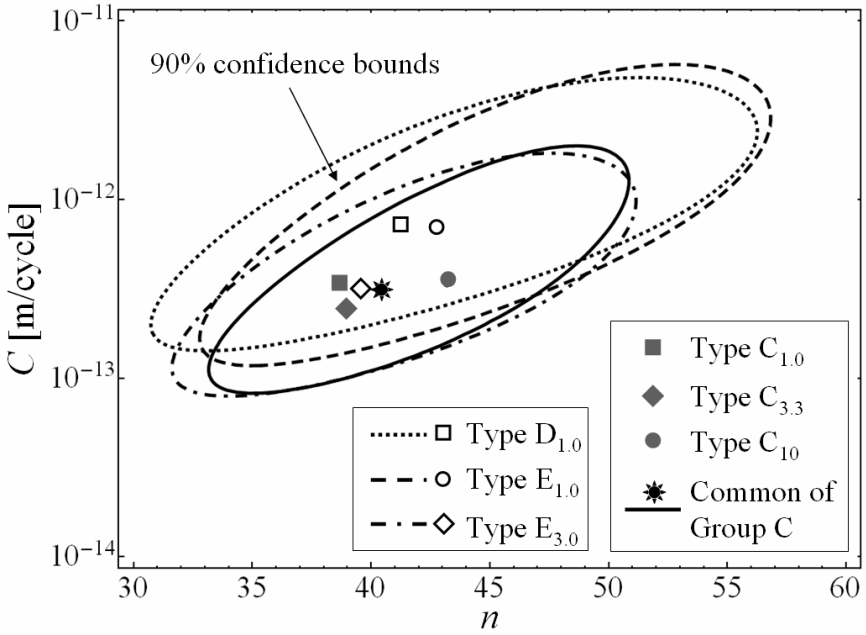


**Fig. 3.20** The best estimators and 90% confidence bounds of $C$ and $n$.

when using the common optimum values the parameters $C$ and $n$ obtained from Group C is now able to be investigated by comparison to the fatigue lifetime distribution when using the individual optimum values of those types. By the same way presented in Chapter II, the differences in lifetime in logarithmic scale $\Delta\log N$ between the cases of using the common and individual optimum values of $C$ and $n$ were calculated and are plotted in Fig. 3.21 for Types $D_{1.0}$, $E_{1.0}$ and $E_{3.0}$. The results show that the absolute value of $\Delta\log N$ is smaller than 1 which corresponds to a factor of 10 in terms of $N$ when the relative stress level $\sigma/\sigma_{N0}$ is larger than 0.2, i.e., the applied stress is larger than $0.2\sigma_{N0}$. This factor reduced to be smaller than 2.6 when the relative stress level $\sigma/\sigma_{N0}$ was larger than 0.5. It means that the fatigue lifetime could be predicted within an efficient accuracy on the basis of the static strength distribution with the common optima of $C$ and $n$ in accordance with specified values of $F$.

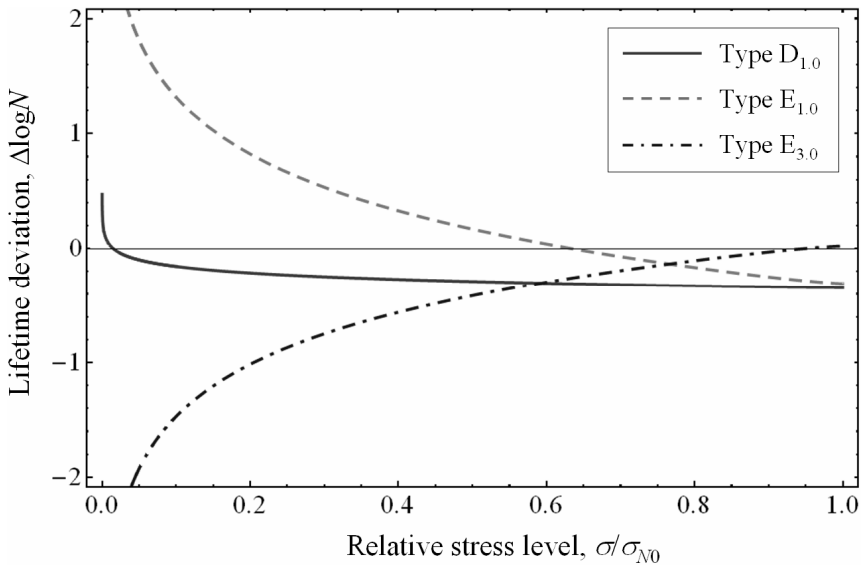


**Fig. 3.21** Error distribution in lifetime of Types $D_{1.0}$ , $E_{1.0}$ and $E_{3.0}$ when the estimated parameters deviate from the common optimum values of $C$ and $n$ of Group C.

## 3.5. Conclusion

In this chapter, a theory describing the static strength and fatigue behavior of MEMS structures with arbitrary stress distributions was formulated by extending the theory presented in Chapter II where the stress distributions were assumed to be uniform. Three groups of polysilicon thin film specimens were fabricated under the different etching condition with different types of shapes in each group, and subjected to experiment. The experimental data were analyzed by applying the concept of inferential statistics in order to estimate the parameters, i.e., $\sigma_0$ and $m$ in the Weibull distribution and $C$ and $n$ in Paris' law, which represent the local characteristics of the static strength and fatigue behaviors of the surface damage due to the etching process.

The analysis results in this chapter showed that the stress distributions on the specimens used in Chapter II were affected by overetching of the gaps separating the inner and outer frames of the test structures. The change of stress distributions led to the parameters scattering on a large range, and therefore left the ambiguity in the conclusion of Chapter II. This was overcome by taking the individual stress distributions of the previously designed specimens into account, and using the newly designed specimens without the effect of overetching in this chapter. It was found that the estimated values of the parameters $\sigma_0$ and $m$ in the Weibull distribution were not

markedly different for the specimens fabricated under the same condition despite the difference of the specimen shapes. The distributions of the parameters $C$ and $n$ in Paris' law were almost identical for all the specimen types fabricated under the different conditions. It means that the etched surface of polysilicon thin films has unique local characteristics regardless of the shape of specimens. The parameters $C$ and $n$ should be the inherent material constants of polysilicon thin films. As a consequence, strength and lifetime predictions can be made about structures with arbitrary stress distributions by using the unique values of the four parameters $\sigma_0$, $m$, $C$ and $n$.

Since the method developed here was examined successfully with the different stress distributions of the specimen types, it is suggested that the application range of the method can be extended to any stress distribution on specimens of the same material with the same planar geometry and structured using the same etching technique. Therefore, the fracture strength and fatigue lifetime of the arbitrarily-shaped polysilicon thin films can be characterized statistically by the described method.

# Chapter IV

# A Novel Fatigue Test with Ramping Stress Amplitude to Evaluate Fatigue Behavior of Polysilicon Thin Films

## 4.1. Introduction

In the previous chapter [75, 6], Paris' law with two unknown parameters was used to predict the fatigue lifetime of polysilicon by using the results of conventional fatigue experiment with constant amplitude, which is hereafter called normal fatigue test. There the fatigue lifetime was predicted on the basis of static strength under monotonically increasing stress. The most inconvenient matter of the normal fatigue tests is that the experiment may have to be stopped before failure when the number of cycles exceeds an affordable time limit as indicated with Z in Fig. 4.1(a). This was usually seen in the previous reports of fatigue tests with constant stress amplitude when the applied stress amplitude was small or the fatigue tests were performed under low humidity environment [7,17,30,33,86,93,100]. It should impede drawing fully the fatigue behavior of silicon. In addition, because of a large scatter in strength, however, it was difficult to evaluate fatigue behavior with the normal fatigue test when

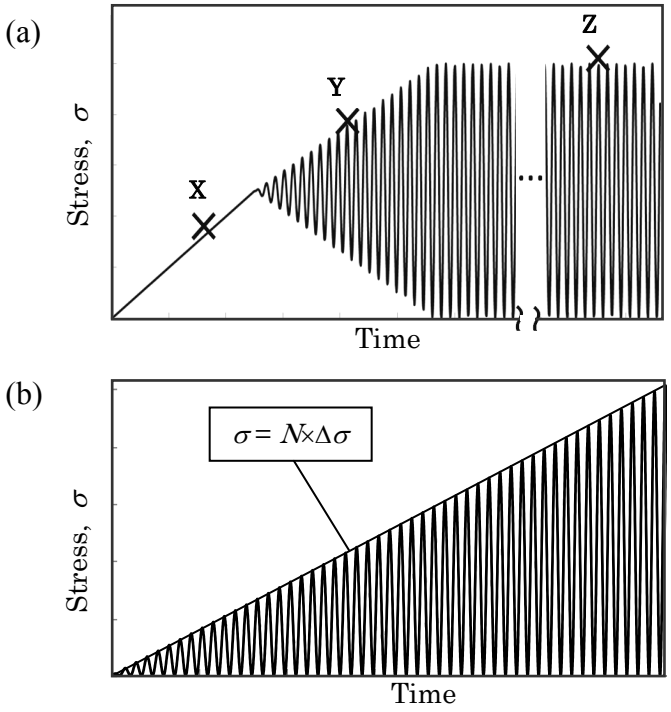


**Fig. 4.1** Actual stress history in (a) the normal fatigue tests with the possible fracture events of specimens and (b) the ramping fatigue tests. In (b), the stress amplitude $\sigma$ linearly increases with the number of cycles $N$ and $\Delta\sigma$ is the ramping increment per cycle.

specimens broke before reaching the target stress amplitude as indicated with X or Y.

In this chapter, the possibility of a new experimental method to estimate the fatigue behavior of polysilicon thin films is studied by using cyclic loading with gradually increasing stress amplitude as shown in Fig. 4.1(b), which is here called ramping fatigue test. This method has none of the fundamental problems of normal fatigue test in Fig. 4.1(a), because the small stress amplitude in the beginning gives fatigue degradation of strength and the large stress at the final stage breaks all the specimens. Therefore the effect of fatigue is seen as reduced fracture stress levels which depend on the fatigue damage. Later on, further increase of stress level breaks all the specimens in a planned period of time. With the success of formulating the normal fatigue test in terms of Paris' law [75,76], the ramping fatigue test is formulated also by Paris' law and the parameters optimized to the experiment were compared in both the fatigue tests. The method is applied to both the cases of the specimens with uniform and arbitrary stress distributions.

## 4.2. Uniform stress distribution

### *4.2.1. Statistical analysis*

The extension rate of the equivalent crack under cyclic loading is formulated by Paris' law as Eq. (2.3) and is rewritten here as

$$\frac{da}{dN} = C\left(\frac{\Delta K}{K_{\mathrm{Ic}}}\right)^n , \tag{4.1}$$

where the stress intensity factor $\Delta K$ is defined by Eq. (2.4) for the normal fatigue test. For the case of ramping test as described in Fig. 4.1(b), the value of applied stress $\sigma$ at the cycle number $N$ was $\sigma = N\Delta\sigma$. Therefore

$$\Delta K = \beta\sigma\sqrt{\pi a} = \beta N\Delta\sigma\sqrt{\pi a} . \tag{4.2}$$

In Eq. (4.2), $\beta$ denotes a dimensionless correction factor reflecting the geometry of both the cracks and the structures, $a$ is the crack length at the cycle $N$. In this study, $K_{\mathrm{Ic}}$ and $\beta$ were taken as the values used in the previous chapters, i.e., 1.1 MPam$^{1/2}$ and 1.12, respectively. By substituting $\Delta K$ in Eq. (4.1) by Eq. (4.2) and then integrating Eq. (4.1) with respect to the crack length from the initial crack length $a_0$ to the critical

length $a_c = (K_{Ic}/\beta\sigma\pi^{1/2})^2$ where the specimen was broken, i.e., the number of cycles needed to go from 0 to $N$, the initial crack length is obtained as

$$a_0 = \left[ \frac{C(n-2)}{2(n+1)} \left( \frac{\beta\sigma\sqrt{\pi}}{K_{Ic}} \right)^n \frac{\sigma}{\Delta\sigma} + \left( \frac{K_{Ic}}{\beta\sigma\sqrt{\pi}} \right)^{2-n} \right]^{2/(2-n)} . \quad (4.3)$$

Since the distribution of initial crack lengths can be evaluated from static strength distribution by combining Eqs. (2.7) and (4.3), the cumulative fracture probability $F$ for the increasing maximum stress $\sigma$ in ramping fatigue tests is formulated as

$$F = 1 - \exp\left\{ -\left( \frac{\sigma}{\sigma_0} \right)^m \left[ 1 + \frac{C(n-2)}{2(n+1)} \left( \frac{\beta\sigma\sqrt{\pi}}{K_{Ic}} \right)^2 \frac{\sigma}{\Delta\sigma} \right]^{m/(n-2)} \right\}. \quad (4.4)$$

When the ramping increment $\Delta\sigma$ comes to infinity, then Eq. (4.4) becomes identical to Eq. (2.1) showing the static strength distribution.

### *4.2.2. Specimens and experiment*

The tensile test structure with the specimens of Groups B and C introduced in Chapter II were utilized for the ramping fatigue tests here. These specimens are parallel-sided specimens, where stress concentration factor was designed to be 1.0 and the stress distribution was assumed to be uniform as it presented in Chapter II.

By using the experimental setup as in Chapter II, the ramping fatigue tests were performed under cyclic loading at a frequency of 100 Hz and gradually increasing stress amplitude as shown in Fig. 1(b). The environment of these tests was the same to the normal fatigue tests, i.e., temperature of 22°C and relative humidity of 80%. The specimens were loaded between zero and the gradually increasing maximum stress, i.e., the stress ratio $R$ was kept to be zero also here. For each group, a number of different increase rates of stress amplitude per cycle $\Delta\sigma$, which is here called the ramping increment, are applied. The ramping fatigue test data of Groups B and C are shown in Fig. 4.2, where the stress amplitude and number of cycles are plotted along the ordinate and abscissa, respectively. In this figure, each symbol indicates the fracture event of a specimen. The solid and open symbols present the experimental data of Groups B and C, respectively. The lines indicate the planned

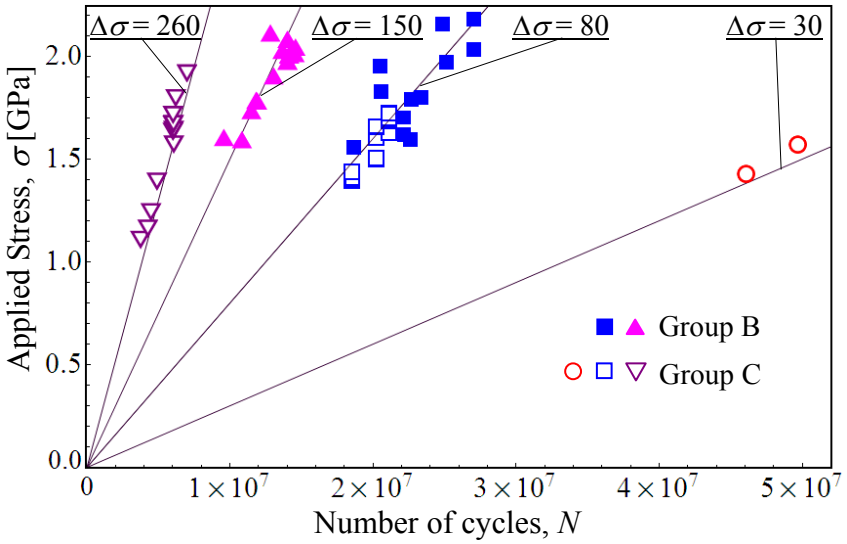


**Fig. 4.2** Ramping test data of both the groups with different ramping increments Δσ [Pa/cycle]. Symbols indicate the fracture events of specimens.

stress histories with the ramping increments $\Delta\sigma$. The data symbols might appear at positions deviating from the lines. This is caused by the fact that the four specimens on each structure were loaded using the actuator under displacement control, i.e., it is difficult to give exactly the same load under displacement control condition to the specimens on different structures with slightly different gap width depending on the situation of backside deep etching.

### *4.2.3. Results and discussion*

In order to compare the results of ramping fatigue tests to the normal fatigue tests, the two parameters in Paris' law for normal fatigue test results evaluated as described previously [75,76,92] are used here. The optimized values of the two parameters $n$ and $C$ of Group B and C obtained in Chapter II are listed again in the upper half of Table 4.1. The values in the column titled with “common” are the optima of $n$ and $C$ obtained by fitting Eq. (2.9) to the fatigue test data of Groups B and C simultaneously.

For the case of ramping test, the cumulative fracture probability $F$ of the specimens was evaluated by $F = i/(I+1)$, where $i$ is the ranked number of the data and $I$ is the number of tested specimens for the individual ramping increments $\Delta\sigma$. It

means that, for a value of ramping increment $\Delta\sigma$ of each group, each specimen was ranked as $i$ from 1 to $I$ from the weakest to the strongest as shown by the symbols in Fig. 4.3. By using $n$ and $C$ obtained from the normal fatigue tests, the cumulative fracture probability $F$ of ramping tests was predicted by using Eq. (4.4) as plotted in Fig. 4.3 with curvilinear lines, which agrees well with the experimental data shown by the symbols. In Fig. 4.3, each symbol type shows the data of experiment with a different intended value of ramping increment $\Delta\sigma$ shown in Fig. 4.2 and the corresponding curvilinear line was calculated by using that value of $\Delta\sigma$. There is no marked difference between Figs. 4.3 (a) and (b) for Group B, and Figs. 4.3 (c) and (d) for Group B, where the individual optima (Figs. 4.3 (a) and (c)) and the common optima (Figs. 4.3 (b) and (d)) of $n$ and $C$ were used for prediction.

When Eq. (4.4) was fitted to the ramping fatigue experimental data by the least squares method, the optimal values of $n$ and $C$ shown in the lower half of Table 4.1 were extracted. In Table 4.1, "common" means that Eq. (4.4) was fitted to the ramping test data of both the groups with the same values of $n$ and $C$. In order to show visually the calculated results of the parameters $n$ and $C$, Fig. 4.4 shows optimum regions and points in the $C$-$n$ space. The optimum $C$-$n$ points, shown as symbols, are those parameter combinations where $\Delta F_{RMS}$ attains its miminum value $\Delta F_{RMSmin}$. The

**Table 4.1.** Optimum values of $n$ and $C$ in Paris' law

| Normal fatigue tests | | | |
|---|---|---|---|
| Parameters | Group A | Group B | Common |
| $n$ | 17.98 | 34.31 | 30.41 |
| $C$ [m/cycle] | $1.86\times10^{-13}$ | $1.55\times10^{-12}$ | $9.62\times10^{-13}$ |
| Ramping fatigue tests | | | |
| Parameters | Group A | Group B | Common |
| $n$ | 27.42 | 31.45 | 30.15 |
| $C$ [m/cycle] | $1.17\times10^{-12}$ | $7.96\times10^{-13}$ | $9.24\times10^{-13}$ |

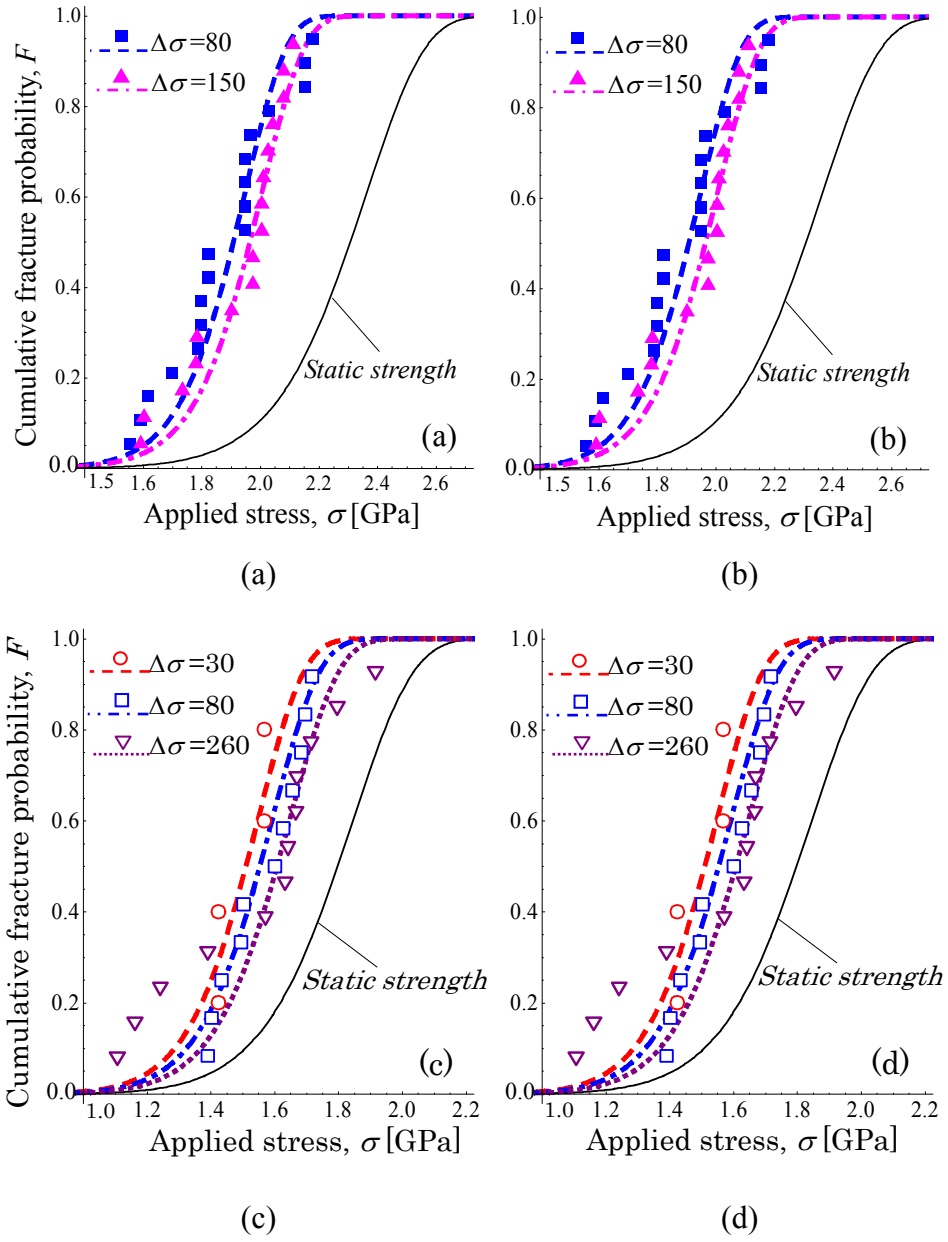


**Fig. 4.3** Prediction results of ramping tests using the individual (a,c) and common (b,d) optimum values of *n* and *C* obtained from normal fatigue tests for both groups of test structures.

contours show loci of *C*-*n* combinations with RMS deviations from the experimental data larger than $\Delta F_{\mathrm{RMSmin}}$ by 0.01. The solid and dashed contours present the RMS deviations in the normal and ramping fatigue tests, respectively. The contours indicate that the increment of the RMS deviation is not marked when the values of *C* and *n* lie in a direction into which the contours extend. It means that the parameter values within these ranges are likely to be obtained from a single mother group of fatigue

behavior and that they are consequently sensitive to small changes of the RMS deviation. In addition, although the individual optimized values of the two fatigue test methods for each group are different, the common values are almost identical. As suggested in Chapter II, although the common values are different from the individual optima, the fatigue lifetime could be well predicted with the common values of $n$ and $C$ [92]. It means that the common optimum values of $n$ and $C$ obtained from ramping tests could be used to predict the fatigue lifetime in the normal fatigue tests.

The optimum $n$ and $C$ values obtained from the ramping fatigue tests were applied backward to predict the normal fatigue behavior in order to confirm that they can be equivalent to those obtained from the normal fatigue test. Figure 4.5 shows the predicted results of fatigue lifetime in comparison to the normal fatigue test data. The predicted surfaces indicated by curvilinear lines were calculated by using Eq. (2.9) in Chapter II. As shown in Fig. 4.5, the experimental data of normal fatigue tests appeared in good agreement with prediction. Figures 4.5 (a) and (b) show the results of fatigue behavior for Group B, while Figs. 4.5 (c) and (d) show those for Group C, both by using the results of $n$ and $C$ from the ramping fatigue tests were used. The larger solid points show the normal fatigue experimental data and the smaller solid

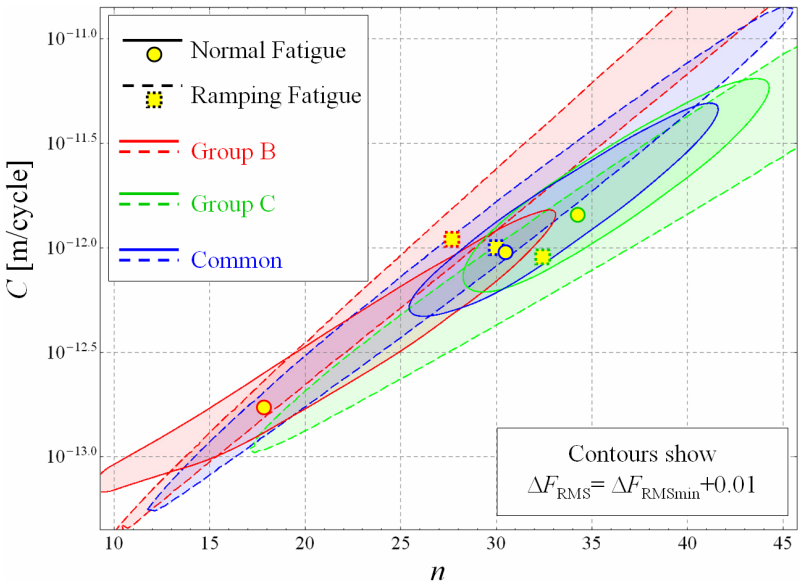


**Fig. 4.4** Contours of RMS deviations and optimum points of $C$ and $n$ obtained by the least squares method with the individual and combined groups. Solid and dashed contours show the RMS deviations of $C$ and $n$ obtained from the normal fatigue test data and the ramping fatigue test data, respectively.

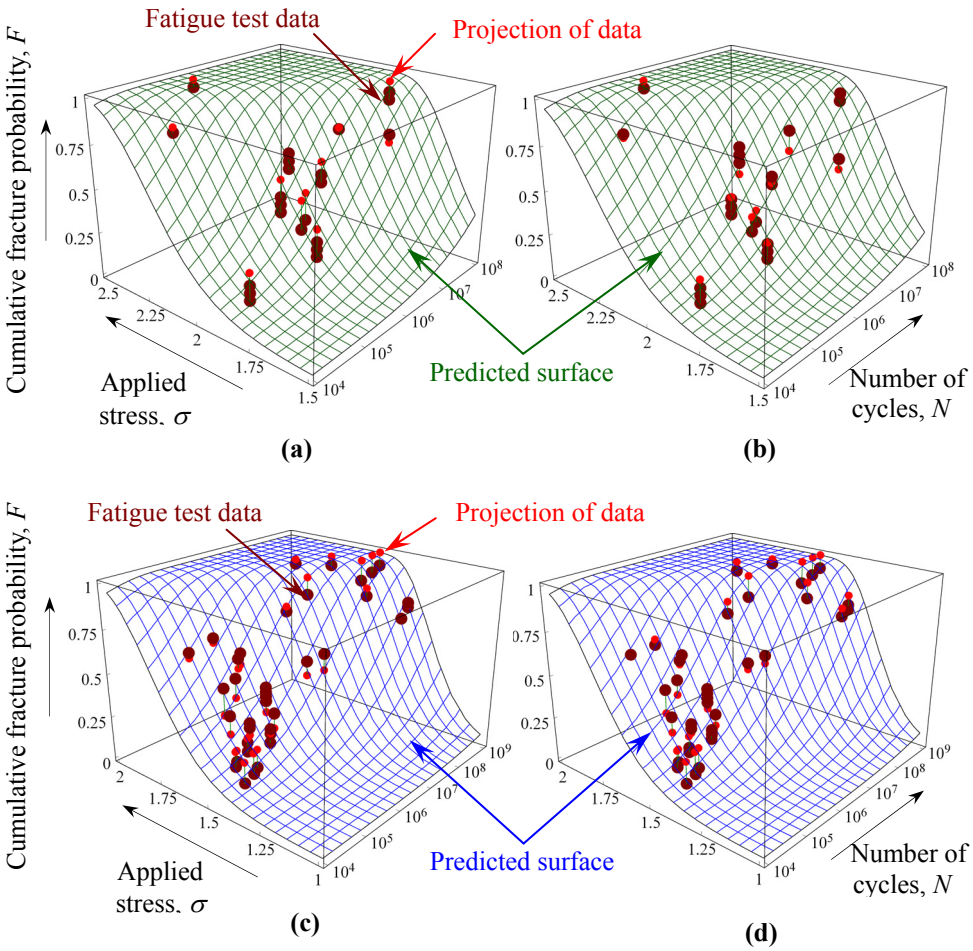


**Fig. 4.5** Three-dimensional plot of predicted fatigue lifetime distribution of Group B (a,b) and Group C (c,d) when using the individual (a,c) and common (b,d) optima of $n$ and $C$ obtained from ramping fatigue tests.

the values of $n$ and $C$ of Groups B and C are different between individual and common optima obtained from ramping fatigue tests, error levels of predicted results in Fig. 4.5 do not differ markedly.

## 4.3. Arbitrary stress distribution

### *4.3.1. Statistical analysis*

Starting from Paris' law as Eq. (4.1), by the same way of implementation for the normal tests with arbitrary stress distribution presented in Chapter III, the cumulative fracture probability $F$ for the entire etched surfaces of a specimen is

formulated as

$$F = 1 - \exp\left\{ -\left(\frac{\sigma}{\sigma_0}\right)^m \sum_e \gamma k_e^m \left[ 1 + \frac{C(n-2)}{2(n+1)} \left( \frac{\beta \sigma k_e \sqrt{\pi}}{K_{\mathrm{Ic}}} \right)^2 \frac{\sigma}{\Delta\sigma} \right]^{m/(n-2)} \right\}, \qquad (4.5)$$

where $\sigma$ is the maximum stress in the specimen, $k_e$ is the ratio of the stress $\sigma_e$ in each element to $\sigma$, and $\Delta\sigma$ is the ramping increment $\Delta\sigma = \sigma/N$. When the ramping increment $\Delta\sigma$ comes to infinity, then Eq. (4.5) becomes identical to Eq. (3.3) showing the static strength distribution of the specimens with arbitrary stress distribution.

### *4.3.2. Specimens and experiment*

For the trial of the ramping fatigue tests on the specimens with arbitrary stress distributions, the specimens of Types $E_{1.0}$ and $E_{3.0}$ introduced in Chapter III were utilized for the ramping fatigue tests here. The ramping fatigue tests on these specimens were also performed under the same conditions to the previous ramping tests. The ramping fatigue test data of Types $E_{1.0}$ and $E_{3.0}$ are shown in Fig. 4.6, where the specimens of Type $E_{1.0}$ were tested with 4 ramping increments and are shown by the open symbols, while those of Type $E_{3.0}$ were tested with only one ramping increment and are shown by the solid symbols. The experimental data follow well the

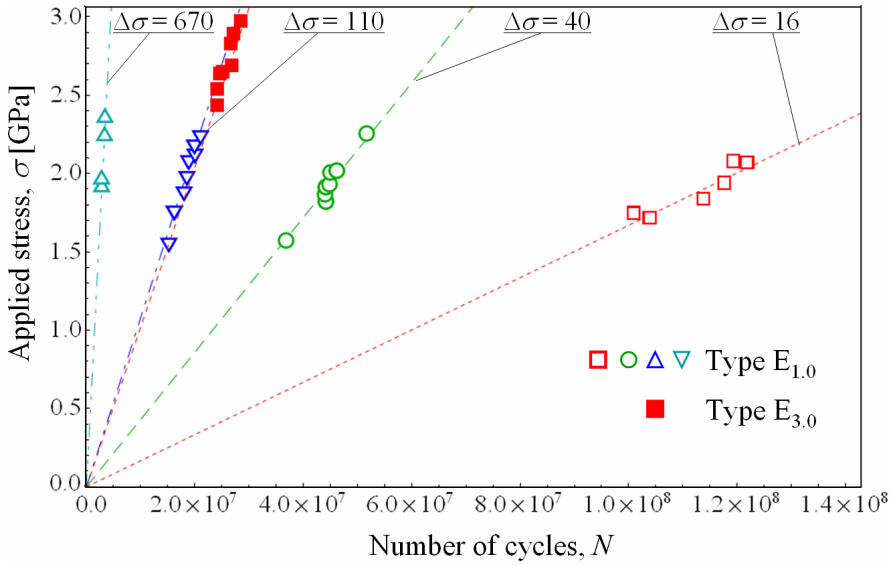


**Fig. 4.6** Ramping test data of Types $E_{1.0}$ and $E_{3.0}$ with different ramping increments $\Delta\sigma$ [Pa/cycle]. Symbols indicate the fracture events of specimens.

planned stress histories. This might be a consequence of overetching effect to be avoided by using the newly designed specimens.

### *4.3.3. Results and discussion*

The cumulative fracture probability $F$ of the specimens was evaluated by and is plotted versus the applied stress amplitude at fracture event in Fig. 4.7 as the open

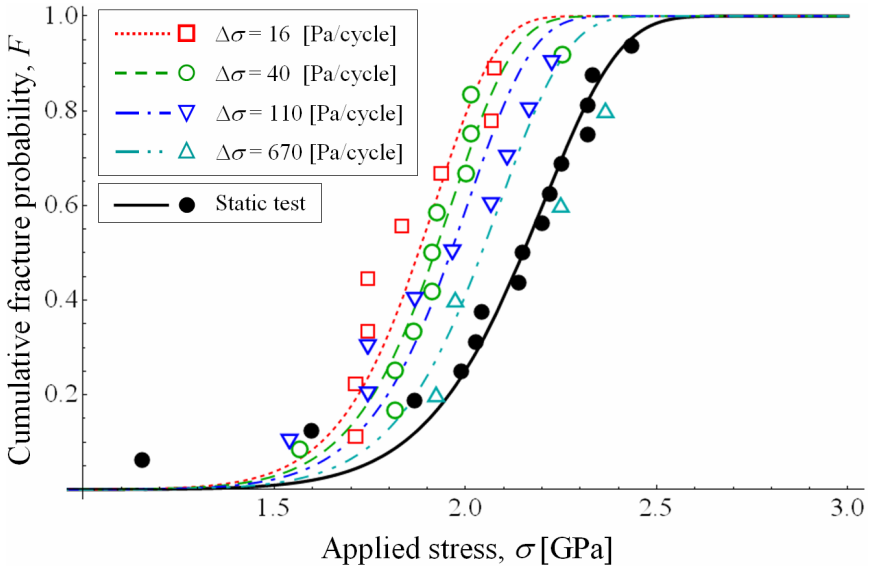


(a) Type $E_{1.0}$

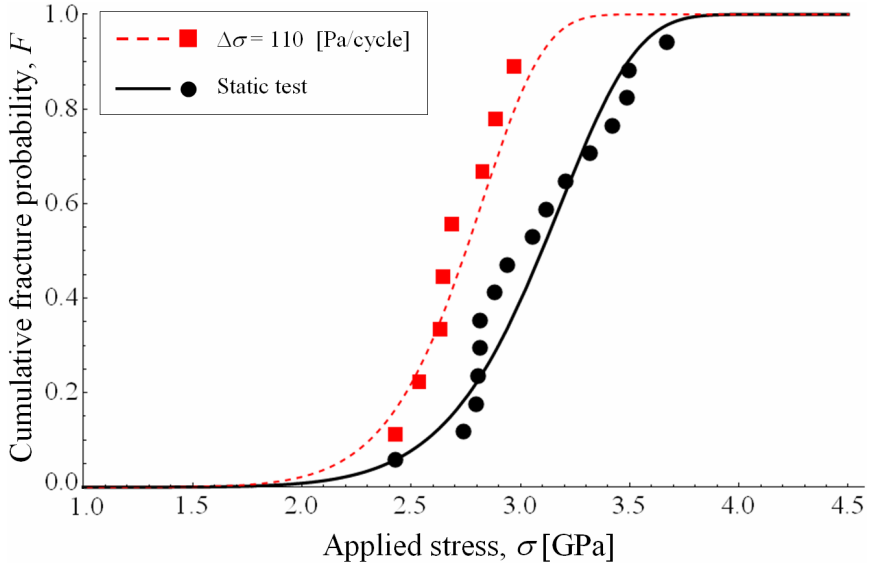


(b) Type $E_{3.0}$

**Fig. 4.7** Prediction results of ramping tests of (a) Type $E_{1.0}$ and (b) Type $E_{3.0}$ using the common optimum values of $n$ and $C$ obtained from normal fatigue tests of Group C.

symbols for Type $E_{1.0}$ and the solid rectangular symbols for Type $E_{3.0}$. The static test data and its fitted distribution are also shown in Fig. 4.7 by the solid circular symbols and solid curvilinear line, respectively, as a comparison of fracture strength. By using the common values of $n$ and $C$ obtained from the normal fatigue tests of Types $C_{1.0}$, $C_{3.3}$ ad $C_{10}$ presented in Chapter III, the cumulative fracture probability $F$ of ramping tests was predicted by using Eq. (4.5) as plotted in Fig. 4.73 with the dashed curvilinear lines. The predictions describe well the distributions of ramping test data of Type $E_{1.0}$ with the ramping increments of 16 Pa/cycle, 40 Pa/cycle, 110 Pa/cycle, and that of Type $E_{3.0}$ with the ramping increments of 110 Pa/cycle.

In order to see whether the experimental data follow well predictions, the average fracture strengths of the predictions and the experimental results was potted in Fig. 4.8, where the abscissa and ordinate show the ramping increment and the applied stress on the specimens at fracture event, respectively. The average strength in the prediction is shown in Fig. 4.8 by the solid curvilinear line, which was calculated by Eq. (4.5) with the cumulative fracture probability $F$ of 0.5. When the ramping increment comes to infinity, it presents the static strength. The average strengths of the ramping fatigue test and static test data are shown by the solid circular symbols. In

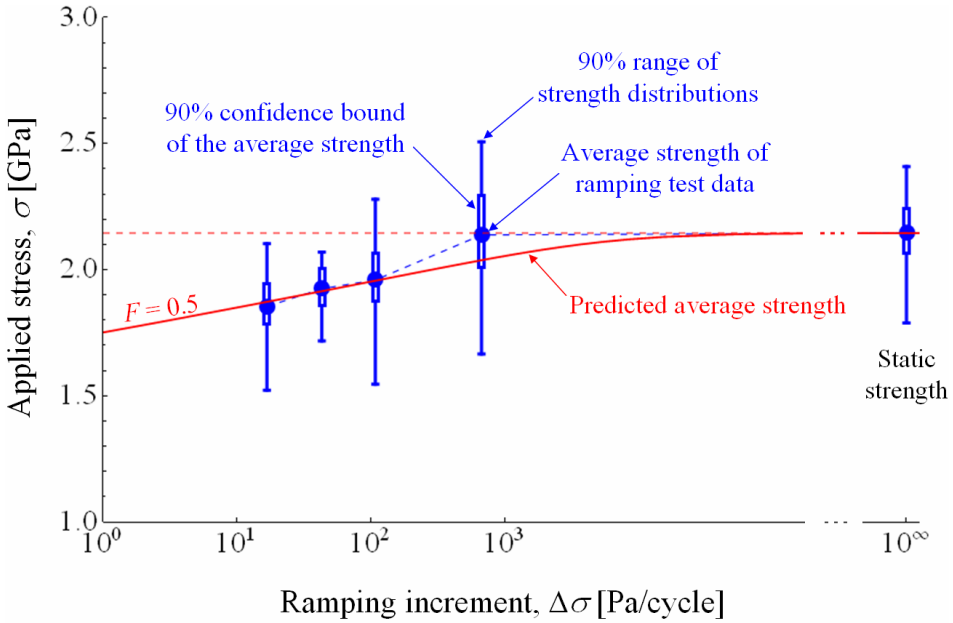


**Fig. 4.8** Comparison of the average strength of the experimental data and the predicted average strength for Type $E_{1.0}$ specimens.

additions, the 90% confidence bound of the average strength and the 90% distribution ranges of the experimental data were presented by the open rectangles and the error bars, respectively. For the case of $\Delta\sigma$ = 670 Pa/cycle, it shows that the average strength of the experimental data was higher than the prediction. This might be because of small number of data as 4 specimens tested at that ramping increment or strengthening effect as reported in the other studies used this experimental method [68,101]. However, since the predicted average strengths lay in the 90% confidence bound of the average strength of the experimental data, the average fracture strengths agree rather well among predictions and experimental results. This fact suggests that the ramping test method could also apply to the specimens with arbitrary shapes to evaluate the fatigue behavior of silicon thin films.

This test method could also be applied to other studies about properties of silicon rather than the use in this thesis. For example, it was used to survey the effect of environment to the strength and fatigue lifetime of silicon and polysilicon thin films [68,101], which were performed by the members in the same laboratory of the author of this thesis.

## 4.4. Conclusion

A novel ramping fatigue test method with increasing stress amplitude was developed to circumvent the problems of the normal fatigue test with constant stress amplitude. Especially, it ensures that experimental data is always obtained in an intended time limit. This method was successfully formulated with Paris' law to predict the fatigue behavior as well as its experimental data to be predicted in connection with the static strength distribution. The values of optimum parameters in Paris' law were quite close in the two fatigue test methods. It was proved that the fatigue behavior of polysilicon under constant stress amplitude can be appropriately and efficiently predicted by applying the new method.

# Chapter V

# A prediction Scheme of Static Fracture Strength of Thick Single-Crystal Silicon Structures Based on the Characterization of Damage Distribution on Processed Surface

## 5.1. Introduction

As introduced in Chapter I and used in the previous chapters, the two-parameter Weibull distribution function [4,6,7,9-13,92,102] was used well to describe the fracture strength distributions of the silicon structures. This is because the Weibull distribution function builds on the weakest link assumption [8] which has been known to fit to the characteristics of brittle materials [8,84]. A number of studies on static strength prediction attempts for silicon MEMS structures were reported [9-13,102], where the parameters of the Weibull distribution were estimated from a reference type of specimens. The extracted parameters were then used to predict the fracture strength distribution of specimens of other shapes, assuming that the local strength of the etched surface is identical regardless of specimen shape. Finite element (FE) analysis was used to evaluate the stress distribution on specimens and, in the next step, their fracture strength distribution. Such a prediction scheme appeared successful at least for the case of thin film specimens [9-11,102]. However, for the case of thick specimens [12,13], the prediction was not always fully convincing.

MEMS structures are often patterned by plasma etching. To fabricate thick structures with high aspect ratios, the so-called Bosch process using inductively coupled plasma reactive ion etching (ICP-RIE) is much appreciated because of its capability to realize close to vertical sidewalls. However, it also inevitably introduces manufacturing damage on the etched surface which determines the fracture strength of the structures [3,4,18,103]. By doing fractography analysis, nano-grooves on the etched surfaces induced by the etching process were observed to be the main source of fracture [34,104]. The relationship of the roughness of etched surface to strength was reported [103], where high surface roughness always indicated low fracture strength, and lower surface roughness resulted in a wider scatter of strength. As the etching progresses deeper and deeper into the wafer, the change of some factors of etching process such as microloading effects, etch lag, gas conductance, etc. [103,104,106] led to the two distinctive features. One is a slight taper of the gap, i.e., inclination of the etched sidewalls. Another aspect is the inhomogeneous distribution of the surface structure and thus of surface defects as a function of the coordinate perpendicular to the wafer [26]. It is expected resulting in a variation of the local strength of the etched surface along that coordinate axis. In the case of thin film structures [9-21,102], the effect of these features on fracture strength may be

negligible. However, especially in the case of thick structures [12,13], it may be the reason for an erroneous fracture strength prediction if it is not appropriately considered. Specifically, the wall inclination was taken into account in one study [12] where the stress distribution was evaluated using FE analysis. However, the stress distribution on the etched surface was not consistently taken into account as required by the weakest link assumption; only the maximum stress was retained for the calculation of fracture probability. To my knowledge, inhomogeneous damage has not yet been taken into account in the literature on strength prediction.

In view of these considerations, the main challenge in this chapter is to establish an advanced method to predict the fracture strength of single-crystal silicon structures, which is able to cope with the inclination of etched sidewalls and the inhomogeneous damage distribution in the etching direction. These characteristics of etched surfaces are fully taken into account in the analysis, aiming at a more robust and accurate fracture strength prediction. Specimens designed without notch were fabricated from a wafer and are used as a reference to estimate the damage distribution on the etched surfaces by applying different stress distributions to the etched surface in the strength tests. Further experiments are planned to systematically examine the applicability of the method, where specimens with notches of different tip radii are subjected to four-point bending test. On the other hand, the fracture strength of the notched specimens is calculated using the distribution of local strength estimated from the reference specimens. The assumptions, namely that the damage induced by the etching process, the surface inclination and the local strength distribution is identical regardless of the shape of specimens, are examined. The effect of these individual factors on the calculation results is assessed separately. The calculated fracture strengths are then compared to the experimental data.

## 5.2. Specimens

Specimens in this study were designed with and without notches, as shown in Fig. 5.1. They are named in this study standard specimen (Fig. 5.1(*a*)) and notched specimens (Fig. 1(*b*)). Their overall length $l$, height $h$ and thickness $t$ are 16 mm, 1.5 mm and 0.38 mm, respectively. The notched specimens were designed with four different notch tip radii as shown in Fig. 5.1(*b*), where the notches are located in the

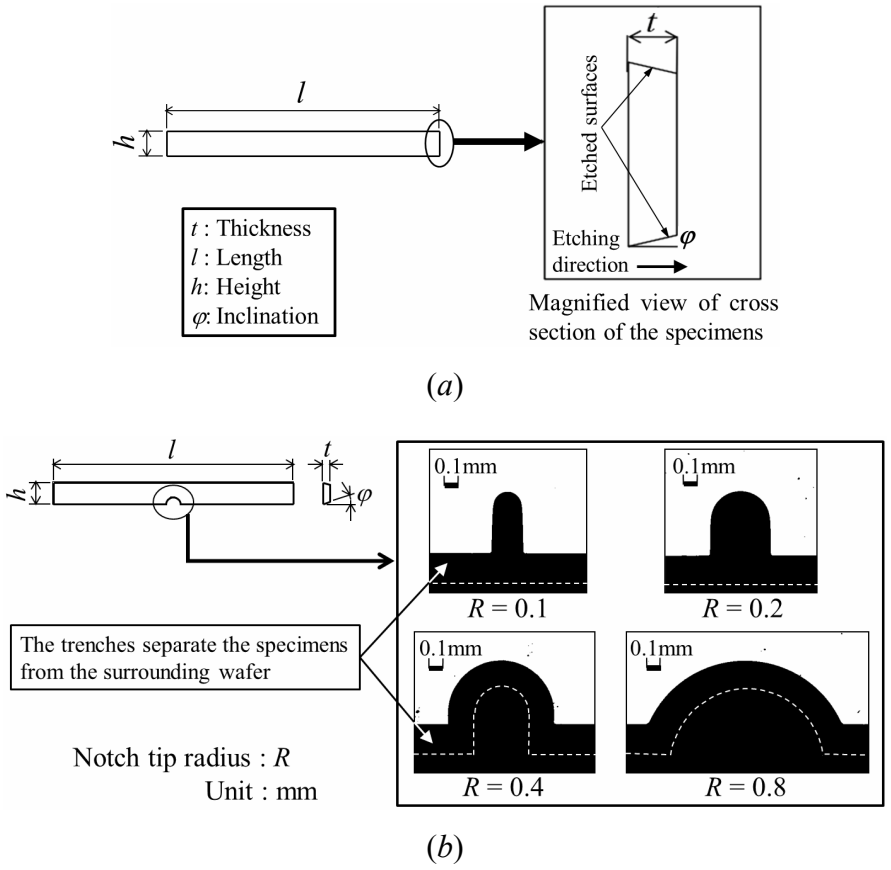


**Fig. 5.1** Specimen designs used in this study, with the shapes of (*a*) the standard specimens and (*b*) the notched specimens.

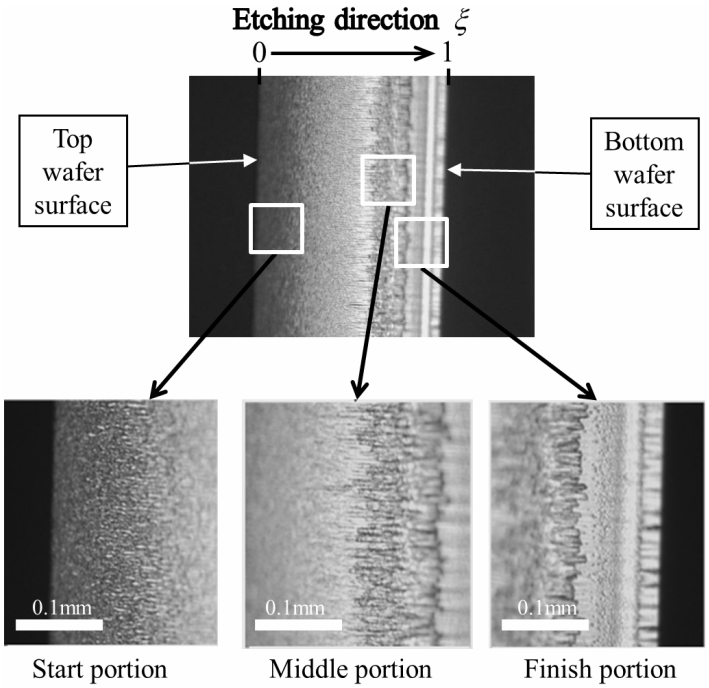


**Fig. 5.2** Optical micrographs of manufacturing damage distribution on the etched surface caused by the Bosch process.

middle of the specimens. The radii $R$ are 0.1 mm, 0.2 mm, 0.4 mm, and 0.8 mm. The depth of all notches is 0.5 mm.

All the specimens were fabricated with identical process conditions from 380-μm-thick (100)-oriented silicon wafers. The wafers were patterned into the specimens by a Bosch process with identical process parameters. As mentioned earlier, the resulting walls show a small taper depending on the process parameters. As a result, the cross-section of the specimens in this study was not perfectly rectangular, but rather trapezoidal as schematically shown in Fig. 5.1(*a*). The average inclination angle $\varphi$ of the etched surface was measured to be 4°, a value common to all specimen types because the trench separating the specimens from the surrounding wafer was designed with a constant width of 200 μm as indicated in Fig. 5.1(*b*). Since the height $h$ decreases in the etching direction, this also induces a non-uniform stress distribution on the etched surface in the direction perpendicular to the wafer.

The etched surface of the specimens was interpreted using an optical microscope. Micrographs are shown in Fig. 5.2, where $\xi$ indicates the position along the etching direction, taking values from 0 to 1 corresponding to the start and end positions of the etching process, i.e., to the top and bottom surfaces of the wafer. The pictures clearly show the difference of the damage close to the start, middle and finish portions on the etched surface. This is expected to induce a variation of the local strength as a function of $\xi$. In contrast, there is no marked difference in the in-plane direction perpendicular to the etching direction. This is consistent with the previous study [102], where the etched surface of 1-μm-thick polysilicon thin films was suggested to have unique local characteristics and therefore the etching damage to be homogeneous.

## 5.3. Experiment

In order to estimate the local strength distribution along the etching direction, which is determined by the inhomogeneous defect distribution, the standard specimens were subjected to four-point bending tests as schematically shown in Fig. 5.3. As shown in Fig. 5.2, the optical appearance of the damage does not change linearly with $\xi$ but rather shows three distinct characteristics in the three portions.

Therefore, in order to figure out the distribution of corresponding local strength, three different stress distribution patterns were applied by bending the specimens in three different directions. The corresponding mechanical situations are termed configurations A, B and C. The three bending configurations correspond to three different weight functions of the applied stress. They enable us to model the $\xi$-dependence of the local strength distribution, by solving an inverse problem on the basis of the fracture load of specimen measured in the three bending configurations.

On the other hand, the notched specimens were subjected to the four-point bending tests only in configuration A with the notches placed at the center, facing downward, and thus being loaded in tension. The data obtained with the notched specimens were compared with the predictions derived from the standard specimen data, as discussed in detail in the next section.

The loading equipment shown in Fig. 5.4 was used for all the tests. A specimen is pushed from above by two upper pins indicated in Fig. 5.4 as push pin. The distance between them is 6 mm. They are attached to the loading part of experimental setup in Fig. 5.4. The loading part is connected to the moving stage by a universal join made of a metal ball with 11 mm diameter. The join ensures that the pins are in contact with the inclined etched surfaces of the specimen along lines experiencing uniform pressure. The moving stage is controlled by a stepper motor in the downward direction at a constant displacement speed of 2 μm/s. On the opposite side, the specimen is supported by two support pins fixed to the stationary stage, as shown in Fig. 5.4. The distance between the two support pins is 13 mm. All the pins are made of stainless steel and have a diameter of 2 mm. The applied load is measured by a load cell LMA-O-50N (from Kyowa Electronic Instruments Co. Ltd.) for a maximum load of 50 N, incorporated in the stationary stage as indicated by the circle in Fig. 5.4. In the experiment, the load is increased monotonically until specimen fracture occurs at the maximum load, after which the load unstably drops to zero.

The stress distribution over the etched surface of each sample type, which is taken here as the distribution of the maximum principle stress, was calculated using FE analysis. Applying the fracture load of each individual specimen gave the maximum stress of each specimen and thus its fracture strength. For example, Fig. 5.5 shows the FE model used to calculate the stress distribution on the notched specimens, which was also used for the standard specimens with configuration A, and the detail

of the maximum principal stress distributions on the notches with different radii. In order to avoid the effect of element size in the prediction [107], the elements on the specimens in all the FE analyses in this study were set with the same area as 0.004 mm2. The stress values on the notches shown in Fig. 5 were calculated with an applied load of 5 N for one push pin. The peak stress appeared on the notches was indicated by the contour numbered as 1. It shows that the peak stress position and stress distribution were changed with the change of notch size. Therefore, stress distribution should be included in the strength prediction due to the change of local strength levels. The maximum amount of deformations on the symmetric plane in X direction relative to Y direction was in a range from 0.24 to 0.34 corresponding to the

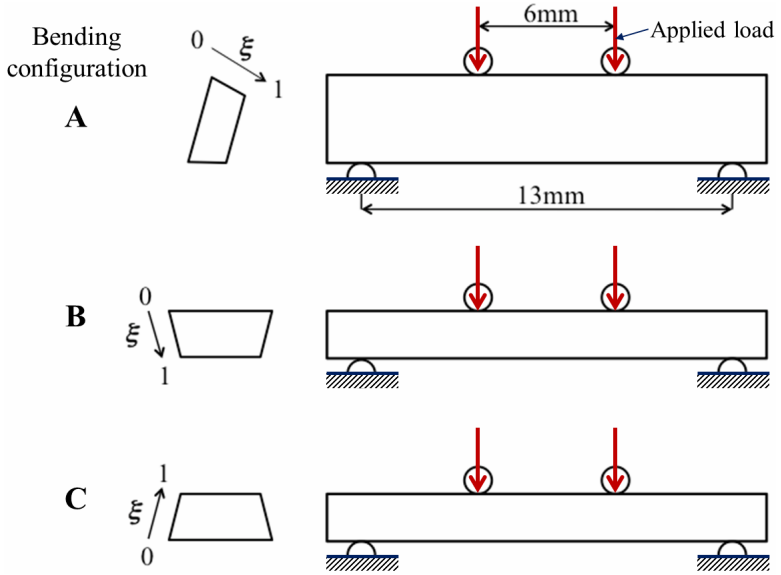


**Fig. 5.3** Three different bending configurations of the four-point bending tests applied to the standard specimens.

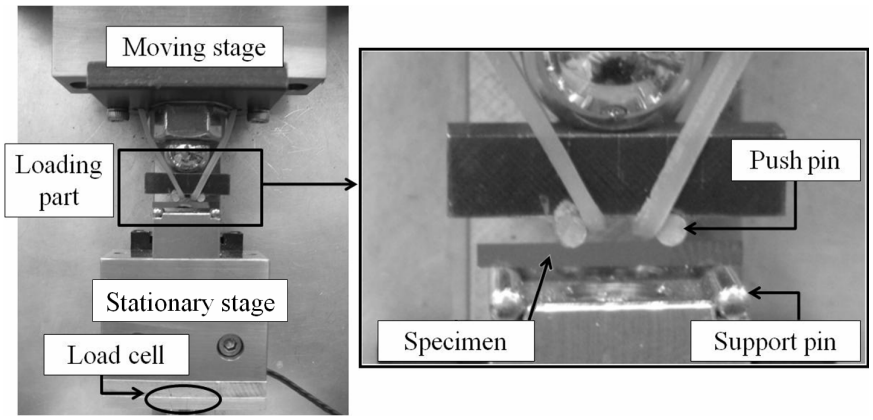


**Fig. 5.4** Experimental setup for the four-point bending tests.

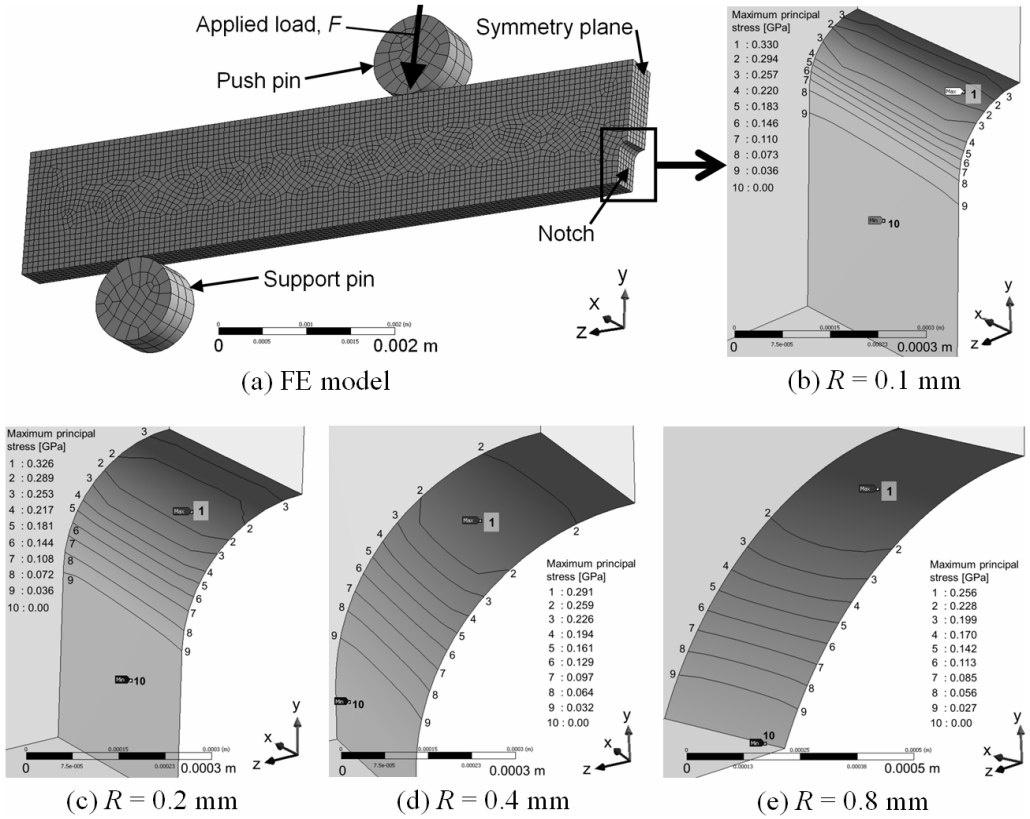


**Fig. 5.5** (a) FE model used to calculate the stress distribution on the notched specimens and the maximum principal stress distributions on the notches of the specimens with (b) $R$ = 0.1 mm, (c) $R$ = 0.2 mm, (d) $R$ = 0.3 mm and (e) $R$ = 0.8 mm when the applied load $F$ was 5 N.

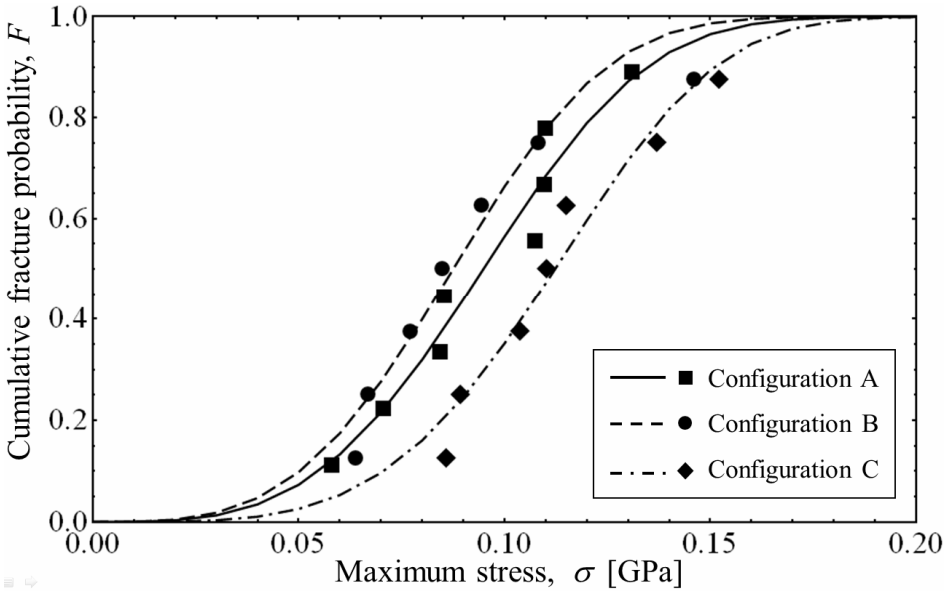


**Fig. 5.6** Cumulative fracture probabilities $F$ of the standard specimens as a function of their fracture strength $\sigma$ for the three configurations of the four-point bending test. The experimental data, shown as solid symbols, are fitted with Weibull distributions.

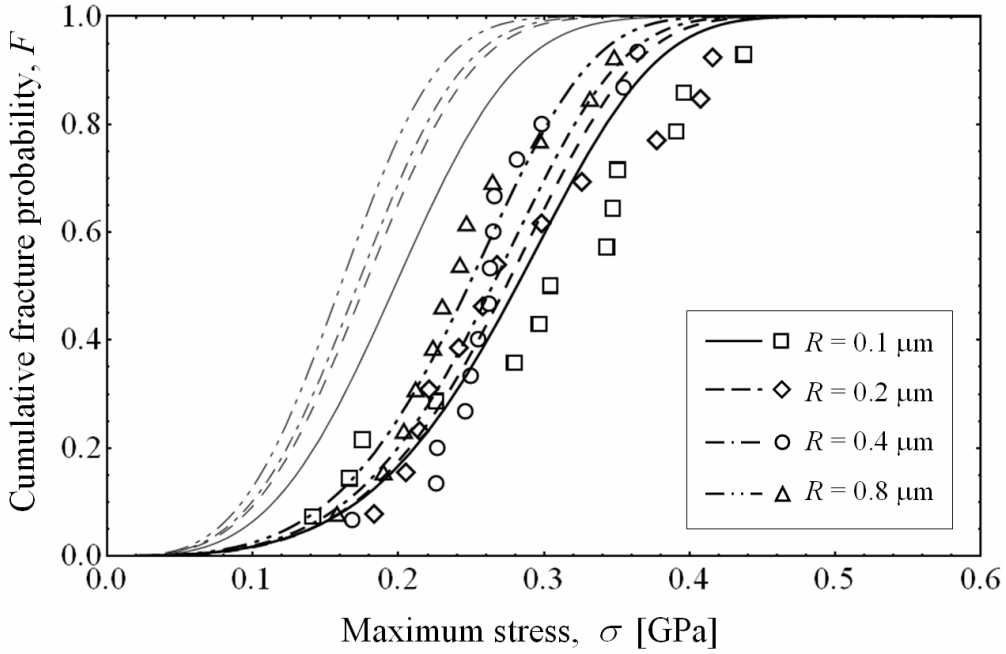


**Fig. 5.7** Cumulative fracture probabilities $F$ of the four types of notched specimens as a function of their fracture strength $\sigma$. The experimental data are shown as open symbols. The black and gray curvilinear lines are the fracture strength distributions predicted with and without the inhomogeneity of etching damage taken into account, respectively.

notched specimen with R = 0.8 and the standard specimen. Besides that, single crystal silicon is known to be anisotropic, and its failure usually occurs along (111) cleavage planes [108]. This means that strength may be anisotropic. The effect of anisotropy was also examined here in comparison to the isotropic case. The difference of the maximum stress between the anisotropy and isotropic cases was 3.4%. The error is small enough even if either anisotropy or isotropic material properties are used as concluded in the previous report [109].

The experiment was performed under lab-air conditions. For the case of the standard specimens, fractography on the fracture surface could help identifying the fracture origins corresponding to the three bending configurations. Unfortunately, the specimens broke away into pieces, which make it also difficult to identify and survey the fracture surface. Therefore, the fracture origins were not able to be identified in this study. The fracture strengths of the standard specimens loaded in the three different bending configurations are plotted in Fig. 5.6, while those of the notched

specimens are shown in Fig. 5.7. Note that the fracture strengths were evaluated here taking into account the taper of etched surfaces in the FE analysis. The cumulative fracture probabilities $F$ were calculated for each type of specimens and bending configuration, as $F = i/(I+1)$ where $i$ is the ranked number of the data and $I$ is the number of tested specimens of each category. Here the data were ranked from the weakest to the strongest specimen.

## 5.4. Statistical analysis

### *5.4.1. Weibull analysis of the fracture strengths*

As a brittle material, silicon shows a wide scatter in strength. Weibull statistics is commonly applied to describe such strength distributions [8,84]. Based on the weakest link assumption, the cumulative fracture probability $F$ of the entire etched surface of a specimen with non-uniform stress distribution is generally defined as presented in the previous chapters [95,96], and rewritten here

$$F = 1 - \exp\left[ -\int_A \left( \frac{\sigma_a}{\sigma_0} \right)^m \frac{dA}{A_0} \right], \tag{5.1}$$

where $m$ is the Weibull modulus representing data scatter, $\sigma_0$ is the scale parameter related to the average strength of a unit area $A_0$, and $\sigma_a$ is the local applied stress. The unit area $A_0$ is set as 1 mm$^2$ in this study. The symbol $A$ indicates the area of the entire etched surface of the specimens. Equation (5.1) is rewritten in the discretized form for numerical calculation as

$$F = 1 - \exp\left[ -\sum_e \left( \frac{A_e}{A_0} \right) \left( \frac{\sigma_e}{\sigma_0} \right)^m \right], \tag{5.2}$$

where $A_e$ and $\sigma_e$ denote the areas and the average stress values, respectively, of the surface elements covering the etched specimen surface subjected to tensile stress, from which fracture is expected to originate. The values of $A_e$ and $\sigma_e$ were obtained from the FE analysis. Assuming linear elastic deformation, the stress $\sigma_e$ of each element is related to the maximum stress $\sigma$ in the specimen by the ratio $k_e = \sigma_e/\sigma$. Equation (5.2) is then rewritten as a function of the variable $\sigma$ by

$$F = 1 - \exp\left[ -\sum_{e} \left( \frac{A_e}{A_0} \right) \left( \frac{\sigma}{\sigma_0} \right)^m k_e^m \right]. \quad (5.3)$$

If the damage distribution on the etched surface is homogeneous, the parameters $m$ and $\sigma_0$ are constants. Based on these simple assumptions, Eq. (5.3) was fitted to the experimental data of the standard specimens as shown in Fig. 5.6 with the curvilinear lines. The fitting procedure was performed with the least square method, i.e., the sum of squared deviations between the values of $F$ of the experimental data and the values calculated by Eq. (5.3) was minimized. The optimum values of the parameters $m$ and $\sigma_0$ are listed in Table 5.1 together with their 90% confidence bounds estimated by likelihood ratio test [8,88].

According to the results in Chapter III [102], it is possible to think that the fracture strength of the notched specimens can be predicted by using Eq. (5.3) with the parameters $m$ and $\sigma_0$ obtained from the standard specimens. The method has already been applied to predict the strength of polysilicon thin films, where the damage distribution along etching direction on the etched surface could be assumed to be homogeneous and the inclination of the etched surface could be ignored in view of the small specimen thickness. However, as mentioned in Section 1, the inclination of the etched surface and variations of the damage distribution may result in questionable strength prediction for thicker specimens [12,13]. In order to assess whether the previous method [102] is able to predict fracture strength of the notched specimens in this study, predictions were first made without taking the inclination of the etched surface and the possible damage inhomogeneity into account.

The stress distributions of all the specimens were thus first calculated by FE modeling with etched surfaces implemented to be vertical. In this case, the values of $m$ and $\sigma_0$ of the standard specimens fractured in bending configuration A were estimated as 3.448 and 0.112 GPa, respectively. By using these values, the maximum stress values $\sigma$ on the notched specimens and their predicted distributions were obtained. They are plotted in Fig. 5.8 as the symbols and curvilinear lines, respectively. The discrepancy between the predictions and experimental data is evident. In other words, the prediction failed. Besides, the maximum stresses on the tested specimens in Fig. 5.8 are smaller than those in Fig. 5.7 where the taper of the etched surface was included in the FE models. This means that the maximum stress

without wall inclination taken into account did not present the true fracture strength of the specimens.

In the next step, the prediction was made by calculating the stress distribution on the specimens with the inclination of the etched surface included in FE models but the damage still assumed to be homogeneous. By using Eq. (5.3) and the values of $m$ and $\sigma_0$ in Table 5.1 estimated from bending configuration A, the fracture strength

**Table 5.1.** Estimated values of $m$ and $\sigma_0$ of the standard specimens with different bending configurations in the four-point bending tests.

| Bending configuration | A | B | C |
|---|---|---|---|
| Number of data | 8 | 7 | 7 |
| $m$ | 3.448 | 3.400 | 4.062 |
| 90% confidence bound of m | 2.675~6.218 | 2.126~4.920 | 2.891~6.787 |
| $\sigma_0$ [GPa] | 0.137 | 0.079 | 0.100 |
| 90% confidence bound of $\sigma_0$ [GPa] | 0.109~0.154 | 0.069~0.101 | 0.091~0.116 |

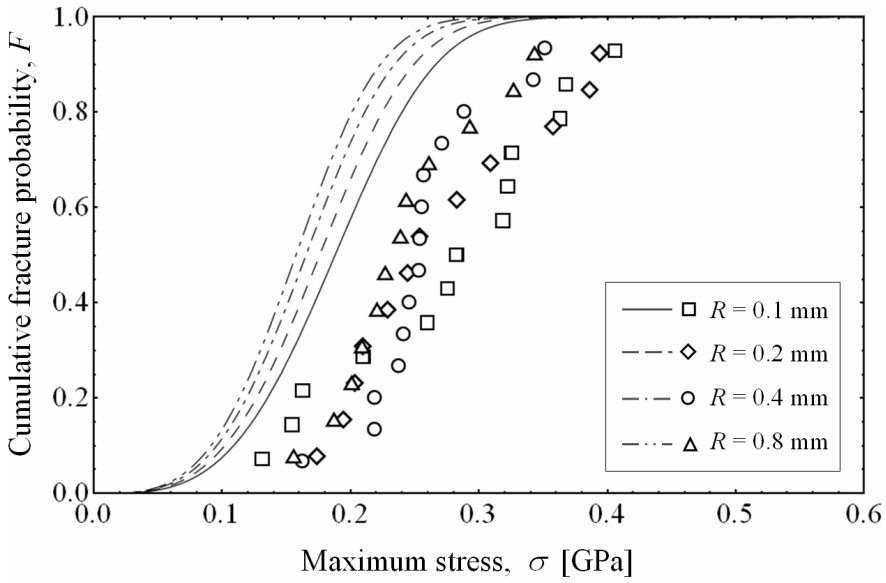


**Fig. 5.8** Fracture strength of the notched specimens when the inclination of the etched surfaces is not taken into account in the calculation and the damage distribution is assumed as homogeneous.

distributions of the notched specimens were calculated and plotted in Fig. 5.7 as the gray curvilinear lines together with the actual experimental data. The discrepancy between the predictions and experimental data clearly shows. Again the fracture strength prediction for the notched specimens still fails. The only assumption that is still being made is that the damage is homogeneous. The next section is dedicated to relaxing this assumption and obtaining consistent strength predictions for all samples.

### *5.4.2. Advanced method of strength prediction with inhomogeneous local strength*

Both the damage distribution and the inclination on the etched surface are included in the following calculations. As evidenced by Fig. 5.2, the damage distribution changed as a function of the perpendicular coordinate $\xi$ on the etched surface. Therefore, the parameters $m$ and $\sigma_0$ are taken be the functions of $\xi$, and denoted as $m(\xi)$ and $\sigma_0(\xi)$. They are assumed here to be second-order polynomials

$$\begin{aligned} m(\xi) &= m_0 + m_1\xi + m_2\xi^2, \\ \sigma_0(\xi) &= \sigma_{00} + \sigma_{01}\xi + \sigma_{02}\xi^2, \end{aligned} \tag{5.4}$$

whose coefficients $m_0$, $m_1$, $m_2$, $\sigma_{00}$, $\sigma_{01}$ and $\sigma_{02}$ will be estimated from the three experimental data sets of the standard specimens. By replacing $m$ and $\sigma_0$ in Eq. (5.3) with $m(\xi)$ and $\sigma_0(\xi)$ in Eq. (5.4), the cumulative fracture probability $F$ of the entire etched surface is fully written as

$$F = 1 - \exp\left[ -\sum_e \left( \frac{A_e}{A_0} \right) \left( \frac{\sigma}{\sigma_{00} + \sigma_{01}\xi + \sigma_{02}\xi^2} \right)^{m_0 + m_1\xi + m_2\xi^2} k_e{}^{m_0 + m_1\xi + m_2\xi^2} \right]. \tag{5.5}$$

Values of the parameters $m_0$, $m_1$, $m_2$, $\sigma_{00}$, $\sigma_{01}$ and $\sigma_{02}$ were estimated by fitting Eq. (5.5) to all the experimental data of the standard specimens from the three bending configurations simultaneously. Their estimated values are shown in Table 5.2. Using these values, the cumulative fracture probability $F$ of the unit area $A_0$ was plotted in Fig. 5.9 as a function of both the fracture strength $\sigma$ and the perpendicular coordinate $\xi$. The plot shows that the local strength on the etched surface became lower and lower with increasing $\xi$. This trend is consistent with the observation in Fig. 5.2, where the damage is seen to be more and more severe along the etching direction

**Table 5.2.** Estimated values of the parameters determining the variation of $\sigma_0(\xi)$ and $m(\xi)$ along the etching direction.

| Parameter | $m_0$ | $m_1$ | $m_2$ | $\sigma_{00}$ [GPa] | $\sigma_{01}$ [GPa] | $\sigma_{02}$ [GPa] |
|---|---|---|---|---|---|---|
| Estimated value | 13.538 | −10.868 | −0.666 | 0.074 | −0.121 | 0.053 |

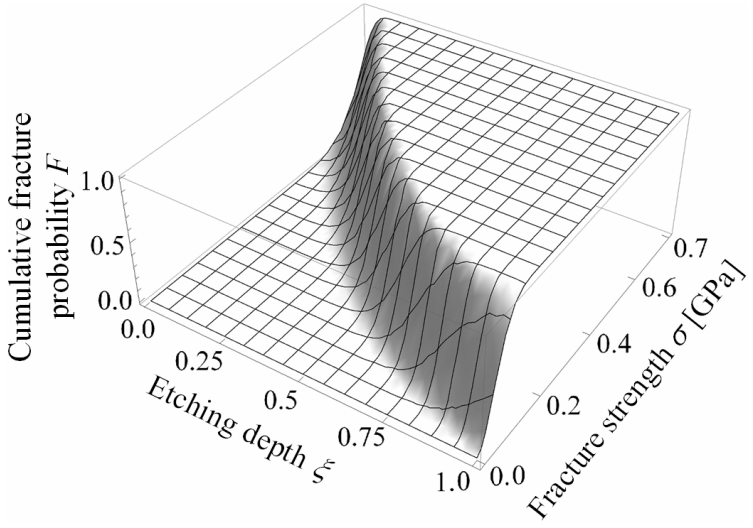


**Fig. 5.9** Estimated fracture strength distribution along the etching direction.

from the top to the bottom surface of the wafer. For the case of thicker specimens etched under the same DRIE condition, the extrapolation of the local fracture strength to deeper position may give incorrect results and should not be attempted uncritically. Whether the methodology can on the other hand be applied to structures in thinner wafers is likely worth considering in another study.

## 5.5. Strength prediction and discussion

By using the estimated parameters in Table 5.2 for Eq. (5.5), the fracture behavior of the notched specimens was estimated with the stress distribution on the etched surface given by the FE analysis. These estimations provided fracture strength predictions for the notched specimens. The results are plotted in Fig. 5.7 as the black curvilinear lines. They are much closer to the experimental data than the grey curves based on the homogeneous damage assumptions.

In order to see how close the predictions are to the experimental data, the probability density functions (PDFs) of the fracture strength distributions are estimated. The PDF is the derivative of the cumulative distribution function (CDF) of the fracture probability. For the case of the prediction, since the fracture strength is calculated by Eq. (5.5), the CDF is defined by Eq. (5.5). For the case of the experimental results, because the data are being dealt here with points, they were replaced by continuous distributions, namely best fitting Weibull distributions. Since the experimental data of the notched specimens were obtained with only the bending configuration A, there is insufficient information to evaluate the continuous distributions using Eq. (5.5). For this reason, the CDFs of the experimental results were taken as those defined by Eq. (5.3). By fitting Eq. (5.3) to the experimental data of the notched specimens, the estimated values of the parameters $m$ and $\sigma_0$ and 90% confidence bounds were obtained as listed in Table 5.3. Fig. 5.10 presents a comparison of the PDFs of the predictions and the experimental results with the average fracture strengths shown by the symbols and 90% distribution ranges indicated by the error bars. The 90% confidence bound of the average strength of the experimental data was also presented in Fig. 5.10. Since the predicted average fracture strengths lay in the 90% confidence bound of the average strength of the experimental data, the average fracture strengths agree rather well among predictions and experimental results. However, their scatters differ, except for the case of the specimens with $R$ = 0.8 mm. It is difficult to conclude whether the predicted distributions are consistent with the experimental results.

The consistency between the predicted distributions and the experimental results can be checked by applying the Kolmogorov-Smirnov test [110,111] under the hypotheses defined as

$$H_0: F_{\text{pre}} = F_{\text{exp}},\ H_1: F_{\text{pre}} \neq F_{\text{exp}} \tag{5.6}$$

where $F_{\text{pre}}$ and $F_{\text{exp}}$ denote the CDFs of the prediction and experimental results, respectively. The Kolmogorov-Smirnov test statistic $D$ is the maximum deviation between $F_{\text{pre}}$ and $F_{\text{exp}}$ as

$$D = \max_{0 \le \sigma < +\infty} \left| F_{\text{pre}}(\sigma) - F_{\text{exp}}(\sigma) \right|. \tag{5.7}$$

The decision is made by the rule

**Table 5.3.** Estimated values of $m$ and $\sigma_0$ used for the PDFs of the notched specimens.

| Notch tip radius $R$ [mm] | 0.1 | 0.2 | 0.4 | 0.8 |
|---|---|---|---|---|
| Number of data | 13 | 12 | 14 | 12 |
| $m$ | 3.057 | 3.156 | 8.816 | 4.259 |
| 90% confidence bound of $m$ | 2.593~3.751 | 2.691~3.864 | 5.698~9.369 | 3.537~5.172 |
| $\sigma_0$ [GPa] | 0.153 | 0.160 | 0.211 | 0.172 |
| 90% confidence bound of $\sigma_0$ [GPa] | 0.138~0.181 | 0.144~0.192 | 0.195~0.224 | 0.158~0.198 |

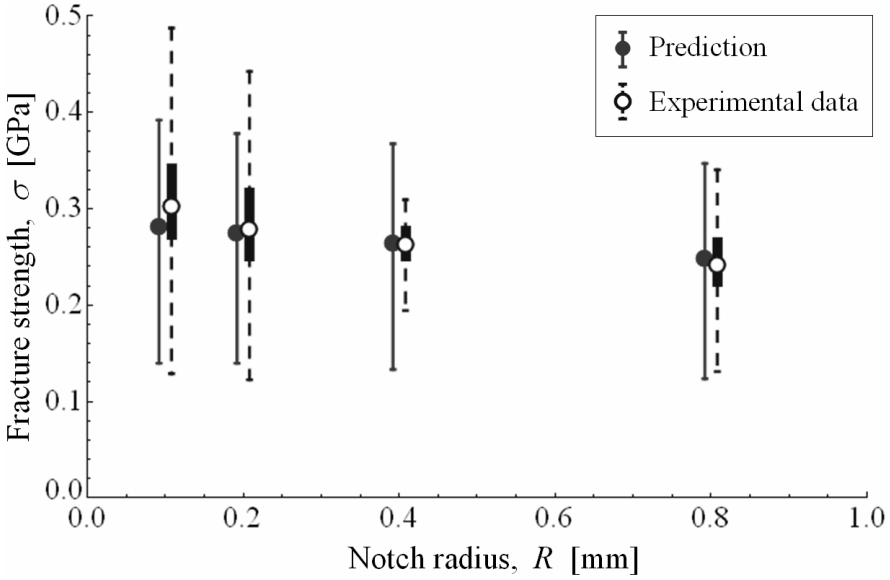


**Fig. 5.10** Comparison of the average strength and 90% distribution range of the prediction and experimental data of the notched specimens. The error bars show the 90% ranges in the scatter of the strength distributions. The solid rectangles show 90% confidence bound of the average strength of the experimental data.

$$\begin{aligned} H_0: &\quad \text{If} \quad D \le D_\alpha, \\ H_1: &\quad \text{If} \quad D > D_\alpha, \end{aligned} \tag{5.8}$$

where $D_\alpha$ is the critical value for the test at significance $\alpha$ and is obtained from the appropriate table in text books [110]. The values of $D$ and $D_\alpha$ with $\alpha$=0.05 were obtained for the distributions of the notched specimens as shown in Table 5.4. Since $D$ was smaller than $D_\alpha$ for all the notched specimens, the hypothesis $H_0$ is accepted, i.e.,

**Table 5.4.** Obtained values of $D$ and $D_\alpha$ with $\alpha$=0.05 in Kolmogorov-Smirnov test

| Notch tip radius $R$ [mm] | 0.1 | 0.2 | 0.4 | 0.8 |
|---|---|---|---|---|
| $D$ | 0.232 | 0.180 | 0.174 | 0.120 |
| $D_\alpha$ | 0.361 | 0.375 | 0.349 | 0.375 |

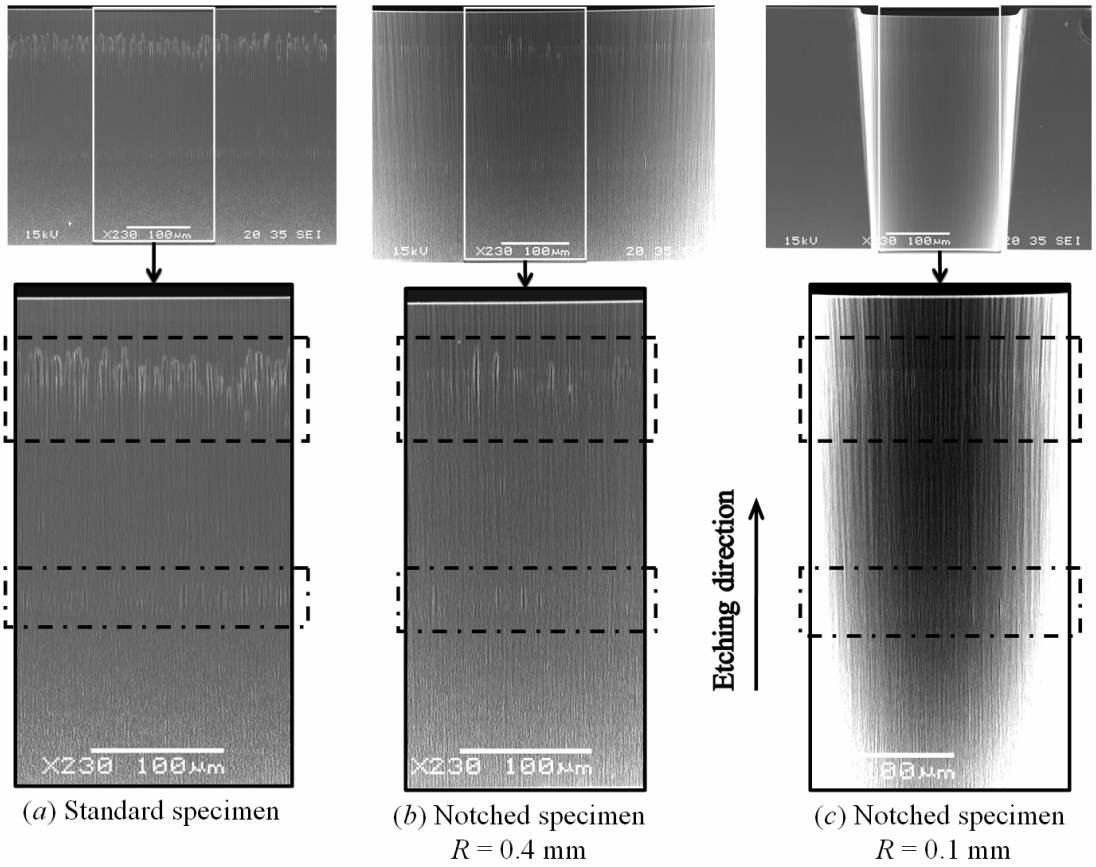


**Fig. 5.11** Scanning electron micrographs of the etched surfaces (*a*) on the standard specimen and (*b*, *c*) on the notch of the notched specimens with (*b*) $R$ = 0.4 mm and (*c*) $R$ = 0.1 mm.

the predicted distributions are consistent with the experimental results. The results of comparison of the average fracture strengths and the Kolmogorov-Smirnov test evidence that the fracture strength of the notched specimens was successfully predicted.

Figure 5.10 also shows that the strength of the actual specimens was slightly higher than the prediction when the notch tip radius is small. This behavior can be

explained by the state of damage on the specimens. Figure 5.11 presents the etched surfaces on a standard specimen and at the tips of the notches of specimens with $R = 0.4$ mm and $R = 0.1$ mm. The difference of the damage distributions are shown clearly in the regions indicated by the dashed rectangles. It is obvious that the etching damage on the notch of the specimen with $R = 0.4$ mm differs little from that on the standard specimen, while the damage on the specimen with $R = 0.1$ mm appears to be less pronounced. The lower roughness of the etched surface on that latter specimen suggests that the fracture strength of this specimen type should be stronger than the prediction. Besides that, the scatter of the strength distribution of the specimen with $R = 0.1$ mm was larger than that of the specimen with $R = 0.4$ mm while the roughness of the etched surface of the specimen with $R = 0.1$ mm was lower than that of the specimen with $R = 0.4$ mm. This is consistent with the reported correlation between etched surface roughness and strength that specimens with better surface quality have a wider distribution in strength [103]. The observation suggests that the etching conditions changed in extremely narrow trenches as compared to the standard trench. Such geometry related effects are well-known in deep reactive ion etching [105,106]. Therefore, it should be noted that the strength prediction method yields accurate results as long as the local etching conditions on the walls of complex specimens remain the same as on the straight walls of the reference specimens.

These results also suggested that considerable changes in the width of trenches separating the etched walls would lead to the change of defect distribution on the etched surface along the trenches. Therefore a design rule can be drawn that the width of trenches should be constant to ensure identical distribution of inhomogeneous etching damage and thus to enable accurate prediction of strength for different curvatures. In other words, it is recommended to implement a standard trench width in the design guideline so that the same inhomogeneous defect distribution as on the flat surface is obtained.

## 5.6. Conclusion

A method to predict the static strength of thick structures patterned into arbitrary shapes with non-uniform damage distribution on the etched surface was proposed. In this method, not only the stress distribution on the etched surface of the

structures but also the vertical damage distribution on the etched surface induced by the etching process was taken into account. By using the parameters estimated from the specimens without a notch, the strength of four different notched specimen types was predicted and was compared to their experimental data. The results show that the predicted strength distributions and the corresponding strength distributions of the experimental data do not differ markedly. In contrast, the predictions omitting the damage distribution and the inclination of the etched surface were unsuccessful. It means that both these features are necessary to be taken into account. In conclusion, the strength of arbitrarily-shaped MEMS structures can be predicted on the basis of (i) the stress distribution of the structures calculated with their real shape and (ii) the damage distribution and Weibull parameters on the etched surfaces estimated from simply shaped reference specimens.

# Chapter VI

# Conclusions

## 6.1. Summary of findings

### *6.1.1. Static strength*

Weibull distribution was extended to evaluate the static strength distribution of polysilicon thin films patterned by etching into arbitrary shapes. It was applied to three groups of the polysilicon thin film specimens with 1 μm thickness, where the three groups were fabricated under different etching conditions which led to the difference of their strength. Different shapes of specimens were prepared in each group. The results show that the static strength of the specimens can be described on the basis of local characteristics determined by using the same set of parameters in Weibull distribution despite the different stress distribution. This means that the local characteristics of etching damage were independent also of the shapes and the stress distributions.

Weibull distribution was then also extended to predicting the strength of thick structures patterned into arbitrary shapes by deep reactive ion etching of silicon wafer. This extension was based on the inhomogeneous defect distribution on the etched surfaces, where the two parameters in Weibull distribution were defined as functions of the etching depth representing the inhomogeneity of the damage on the etched surface in the etching direction. The results showed that the fracture strength of arbitrarily-shaped structures can be predicted with a statistical difference on the basis of the information obtained from a number of specimens with a reference shape, by taking into account the characteristics of etched surface, i.e., the inhomogeneous damage.

Therefore, these theories enable prediction for fracture strength and thus designing new silicon structures on the basis of the information obtained from a set of reference specimens.

### *6.1.2. Fatigue behavior*

The fatigue process determining the lifetime of polysilicon thin films was modeled with the well-known Paris law as the fatigue crack extension process from the initial defects, whose equivalent crack lengths were evaluated from the initial strength distribution described by the Weibull distribution. It was also extended to

evaluate fatigue behaviors of specimens patterned into arbitrary shapes. The parameters in Paris' law were fit to the results of tensile fatigue tests with constant stress amplitudes performed on five groups of polysilicon thin film specimens patterned using different etching conditions leading to different etching damage. The specimens were designed with different shapes of notches in order to have different stress distributions. The results support a possibility that the equivalent extension behavior of cracks is independent of etching condition, also of the shapes and the stress distributions. Therefore the fatigue lifetimes can be practically predicted from their strength distributions by using the same values of the parameters in Paris' law.

The stress distributions on the specimens were also found to have an important role in estimation of the strength and especially the fatigue behaviors of silicon structures. The unexpected change in stress distribution of the polysilicon thin film specimens, which was found to be induced by the overetching of the gap on the tensile test structures, led to the statistical characteristics of the data to be consequently distorted. Therefore, the specimens should be used for the characterization of fracture strength and fatigue lifetime only with utmost care and definitely only on the basis of a very careful analysis of their geometry including their support regions.

For the case of very long fatigue lifetime, by the way, experiment may have to be stopped before failure when the number of cycles exceeds an affordable time limit. To overcome this hurdle, a new experimental method was proposed in order to estimate the fatigue behavior of polysilicon thin films by using cyclic loading with gradually increasing stress amplitude. The results show that the parameter values are the same as those obtained from the fatigue tests with constant stress amplitude, and that the new experimental method can be used to predict the fatigue lifetime in a more efficient manner.

### *6.1.3. General*

This thesis performed the statistical characterization of the strength and fatigue lifetime for silicon and polysilicon structures in MEMS. The results supply fundamental knowledge of fracture strength and fatigue behaviors of silicon to apply for designing MEMS structures.

With the findings above, the fracture strength and fatigue lifetime of silicon structures in MEMS becomes predictable, and therefore they enable designing silicon MEMS structures with a specified level of mechanical reliability. This will help to save the time and expenses in the development of MEMS structures.

## 6.2. Applications

### *6.2.1. Strength and fatigue lifetime prediction*

Prediction procedure of the fracture strength and fatigue lifetime is described briefly by the flow chart in Fig. 6.1. In this procedure, the input information is the MEMS structures with different shapes. The mission is to estimate their strength and fatigue lifetime. To execute this mission, we can not do the static and fatigue tests for all the types of those MEMS structures, because it will take time and consume a large number of structures for the tests. Instead, a number of structures with the same shape are selected as the specimens for the static and fatigue tests. If those structures are too complicated for the tests, a set of specimens suitably designed for the tests could be prepared by the same fabrication conditions of those structures. The static and fatigue

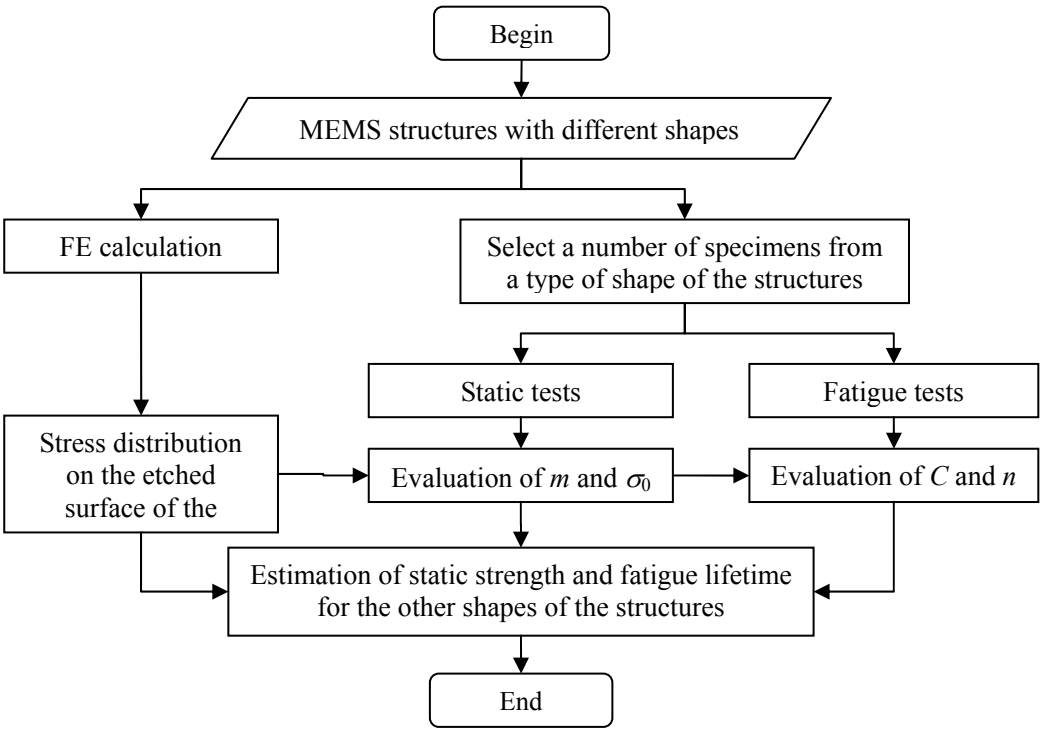


**Fig. 6.1** Procedure of static strength and fatigue lifetime predictions

test data and the stress distribution on the etched surface of those specimens obtained from FE calculation will be used to evaluate the parameters $m$ and $\sigma_0$ in Weibull distribution, $n$ and $C$ in Paris' law. By using those values of the parameters and the stress distribution obtained from FE calculation for the others shapes of those MEMS structures, their static strength and fatigue lifetime distributions will be estimated by using Eqs. (3.3) and (3.12), respectively. It means that the static strength and fatigue lifetime of all those MEMS structures would be predicted. In this procedure, the fatigue tests could be the normal fatigue test or the ramping fatigue test.

### *6.2.2. Designing MEMS structures*

By extending the above procedure, a design process of MEMS structures is described by the flow chart in Fig. 6.2. In this procedure, the mission is that designing

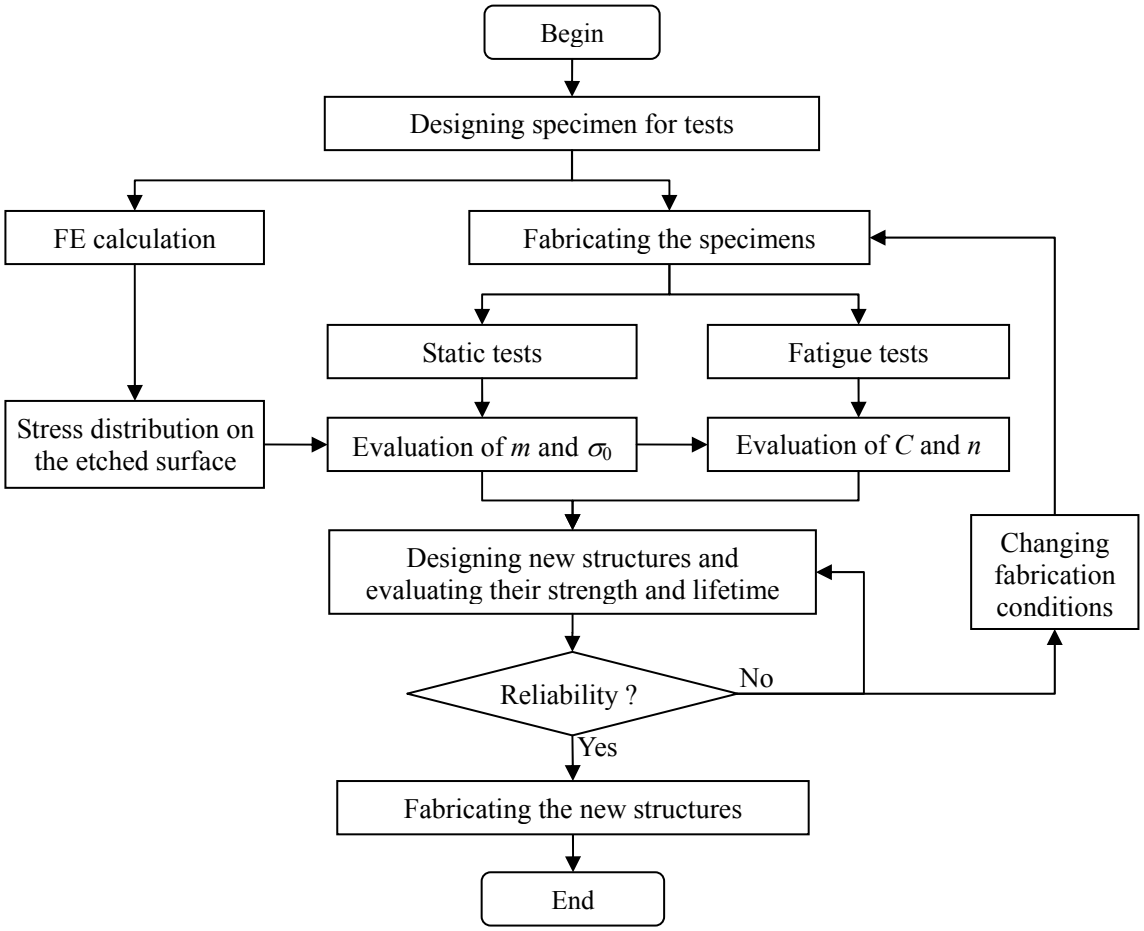


**Fig. 6.2** Procedure for designing MEMS structures by applying the results in this thesis

MEMS structures with the intended level of reliability. For example, it might be that the structures should be designed for 90% of them to break under a static load or survive after a number of cycles of cyclic loading. Firstly, specimens for the static and fatigue tests will be designed and fabricated. The stress distribution on this specimen is also calculated by FEM. The specimens are then tested with the static and fatigue tests in order to evaluate the parameters $m$ and $\sigma_0$ in Weibull distribution, and $n$ and $C$ in Paris' law. By using this information, new structures will be designed and their strength and fatigue lifetime can be evaluated. If the reliability of the new structures is satisfied, they will be fabricated. Otherwise, they will be redesigned and checked again. If the reliability of the new structures can not be satisfied by that way, fabrication conditions can be changed. This way, the specimens will be newly fabricated for the new tests, and the design process is repeated.

## 6.3. Future works

This thesis supplied the fundamental understandings in the statistical characterization of the strength and fatigue lifetime for silicon and polysilicon structures in MEMS. However, the theory of evaluation of fatigue lifetime was examined with only 1-μm-thick specimens tested in one environment conditions and with load ratio $R = 0$. Besides, fatigue mechanism of silicon is still unclear and there are many factors affecting the fatigue behavior as discussed in Chapter I. Therefore, further studies are necessary for understanding further the effect of those factors on the theory here. The factors, which should be surveyed to see how the parameters $C$ and $n$ in Paris' law change, are listed as follows

- Specimen thickness
- Environment: humidity, temperature
- Cyclic loading properties: frequency, load ratio.

When their effects are understood, the overview of fatigue behavior of silicon can be drawn, and therefore the parameters $C$ and $n$ can be interpolated to predict fatigue lifetime of arbitrary structures operating under different conditions of load and environment.

For the case of thick structures, where damage distribution in etching direction

is inhomogeneous, a theory to evaluate their fatigue lifetime can be in principle applied by extending the theory in this thesis but was not confirmed. Since the static strength of this case was estimated and fatigue process could be modeled with Paris' law on the basis of the initial strength distribution, fatigue lifetime of the thick structures is hopefully predictable. However, a further study to examine this case is necessary.

# Appendix 1

# Fractographic Analysis for Polysilicon Thin Films

## A1.1. Introduction

Fractography is the study of fracture surface of materials [113]. It is used to investigate the fracture histories of structures. It should help to identify the initial crack as well as fatigue crack for polysilicon thin films in this thesis in order to support the estimation results. However, when using those parallel-sided specimens, the detailed observation of fracture surfaces was not always easy because the sample frequently shatter into pieces. By using notched specimens presented in Chapter III, this problem is overcome by notches to confine the location of fracture and preserve the specimens after fracture. The fracture surfaces are observed in this appendix by a scanning electron microscope (SEM) to carry out a fractographic analysis, trying to identify initial and fatigue cracks on those surfaces. The initial crack length is evaluated from static strength obtained in Chapter III. The fatigue crack extension process is estimated by using Paris' law on the basis of the parameters evaluated from the static and fatigue test data. The calculated crack lengths are then compared to the crack lengths measured on the fracture surfaces.

## A1.2. Overview of fracture site

By using the notched specimens with the stress concentration factor of 10, i.e., the specimens of Type $C_{10}$ presented in Chapter III, the notches confined the location of fracture and preserve the specimens after fracture. Therefore, the fracture surfaces could be observed in a scanning electron microscope (SEM) to carry out a fractographic analysis. An overview of a crack that started from the notch root, taken by SEM after the test, is shown in Fig. A1.1. Both surfaces of the crack are successfully preserved after the test. The implementation of a single notch in a specimen helps us to identify the origin of the crack.

## A1.3. Static fracture

The crack surfaces of the two specimens of Type $C_{10}$ tested with the static experiments were observed in detail by SEM as shown in Fig. A1.2. They show smooth regions indicated by the solid black curves. They appear at the notch root from where the crack was expected to originate. Their shape is semi-circular. The

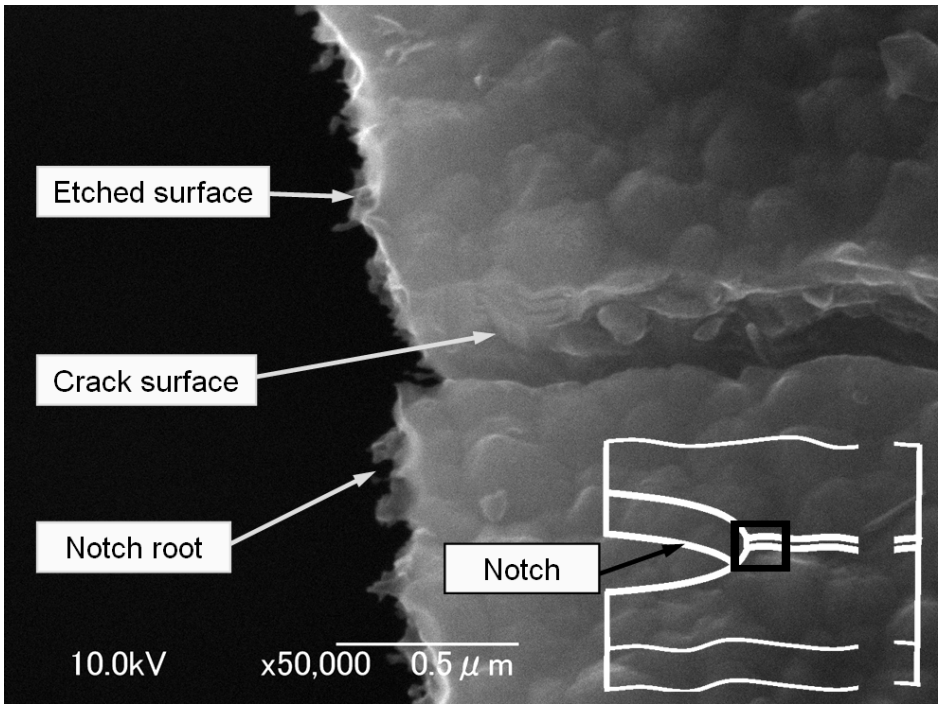


**Fig. A1.1** SEM picture of a crack at the notch root of a tested specimen.

region beyond the boundary of the smooth region is observed to be rough, which corresponds to catastrophic fracture. The aspect of these regions is consistent with the initial crack observed by others [32]. These regions are assumed to be the initial cracks. The initial crack length measured here is in the range from 50 nm to 110 nm.

On the other hand, the initial crack length can be evaluated from the static strength as $a_0 = (K_{Ic}/\beta\sigma\pi^{1/2})^2$. The cumulative probability $F$ of the initial crack length is obtained by rewriting Eq. (3.3) as

$$F = 1 - \exp\left[-\left(\frac{a_0}{a_{\sigma 0}}\right)^{-m/2} \sum_e \gamma k_e^m\right], \tag{A1.1}$$

where $a_0$ and $a_{\sigma 0}$ are the initial crack length of a specimen and the average initial crack length, respectively. The crack length $a_{\sigma 0}$ is calculated from $\sigma_0$ as $a_{\sigma 0} = (K_{Ic}/\beta\sigma_0\pi^{1/2})^2$. By applying the estimated values of the parameters $m$ and $\sigma_0$ of the Type $C_{10}$ specimen shown in Table 3.1, the distribution of $a_0$ was calculated and plotted in Fig. A1.3. The solid and dashed curves show the cumulative probability and probability density distributions of the initial crack length fitted to the experimental results. The symbols present the calculated crack length of the tested specimens

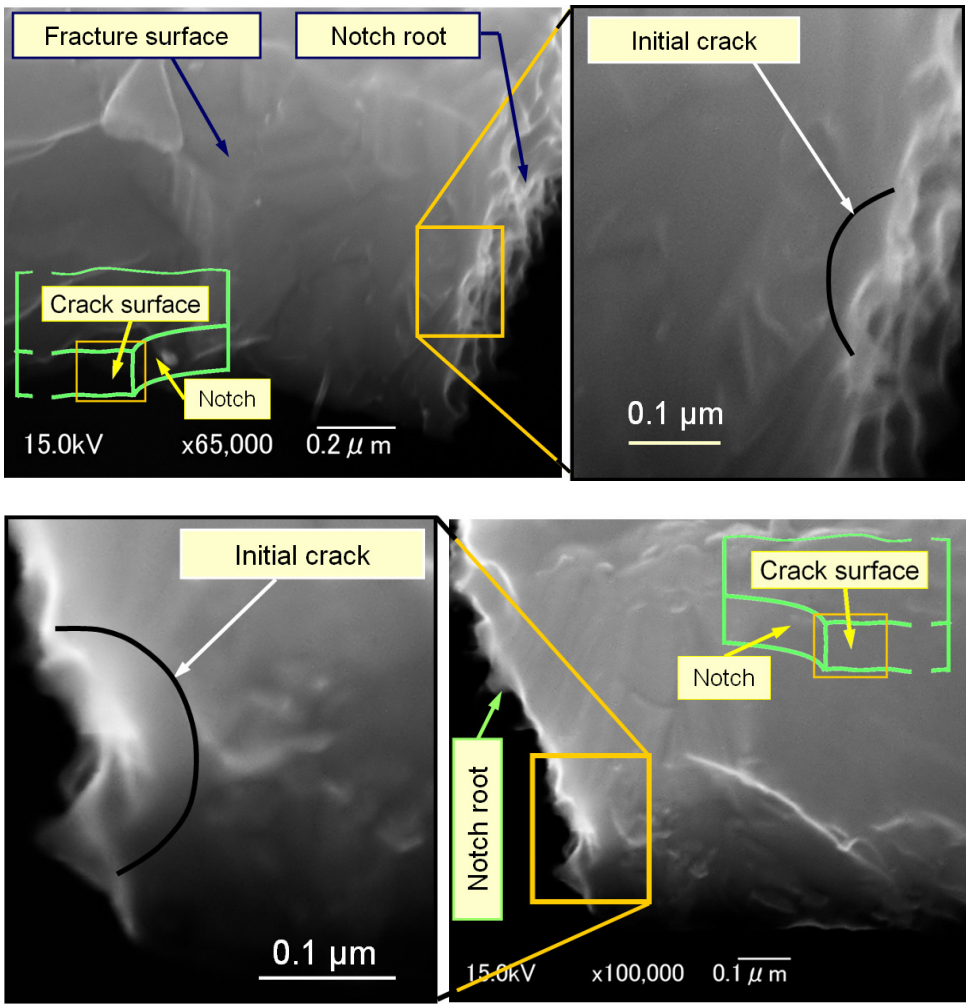


**Fig. A1.2** SEM pictures of crack surfaces of the specimens tested with the static experiments.

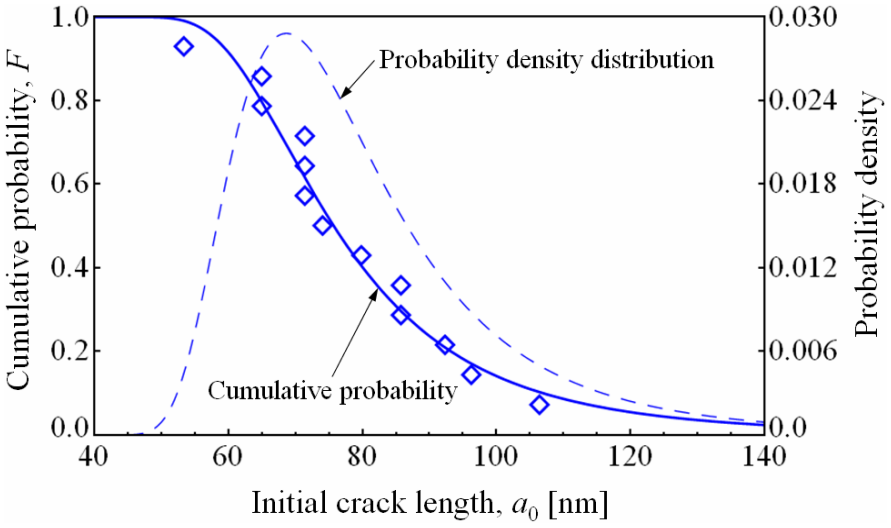


**Fig. A1.3** Initial crack length distribution.

obtained from the static experiments of Type $C_{10}$. The calculated distribution shows that 90% of the initial cracks have lengths in a range from 57.9 nm to 122.0 nm. This range is consistent with the initial crack length of the specimens documented in Fig. A1.2.

## A1.4. Fatigue fracture

The crack surfaces of two specimens of Type $C_{10}$ tested with the fatigue experiments were also observed in detail by SEM as shown in Fig. A1.4. Based on their different roughnesses, the crack surfaces were able be classified into three regions corresponding to the initial crack, fatigue crack extension and unstable fracture. The initial crack regions have the smallest roughness. It is indicated by the solid curves. These regions have shapes similar to those of the initial cracks observed in Fig. A1.2. In addition, their size lies in the range of the initial crack length discussed in the previous section. The regions of fatigue crack extension are indicated by the dashed curves. The roughness of these regions is higher than that of the initial crack region but smaller than that of the unstable fracture region. The fatigue cracks extended from the initial crack length to the critical length which was measured here to be in a range from 100 nm to 180 nm.

On the other hand, the crack length after $N$ cycles of load is formulated by modifying Eq. (3.10) as

$$a_{\mathrm{N}} = \left[ {a_0}^{(2-n)/2} + \frac{C(2-n)}{2} \left( \frac{\beta\sigma\sqrt{\pi}}{K_{\mathrm{Ic}}} \right)^n N \right]^{2/(2-n)} . \qquad \text{(A1.1)}$$

This equation expresses the extension of initial crack as a function of the applied stress amplitude $\sigma$ and number of load cycles $N$. By using Eq. (A1.1) with the estimated values of the parameters $C$ and $n$ of Type $C_{10}$ shown in Table 3.2, the progressive crack length extension during the fatigue process is plotted in Fig. A1.5. In this case, as an example, the applied stress was at 80% of the average static strength. The crack length extension process was plotted starting from the initial crack lengths corresponding to $F$ values of 0.1, 0.5 and 0.9. They show that the crack extension becomes prominent after a certain number of cycles and then increases quickly to the critical crack, which leads to the relative roughness of the fatigue crack

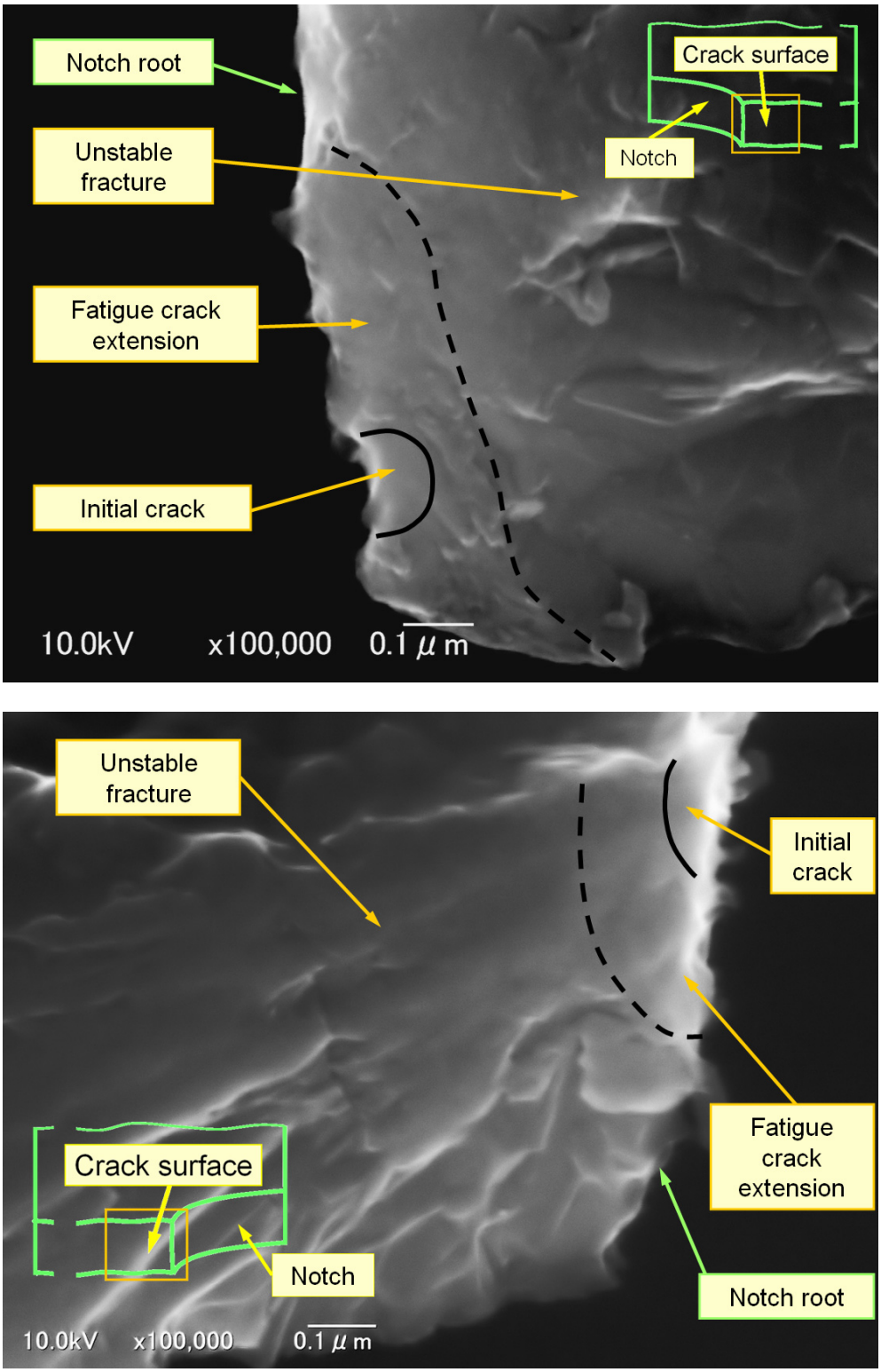


**Fig. A1.4** SEM pictures of fatigue crack surfaces of the specimens broken after $10^7$ cycles.

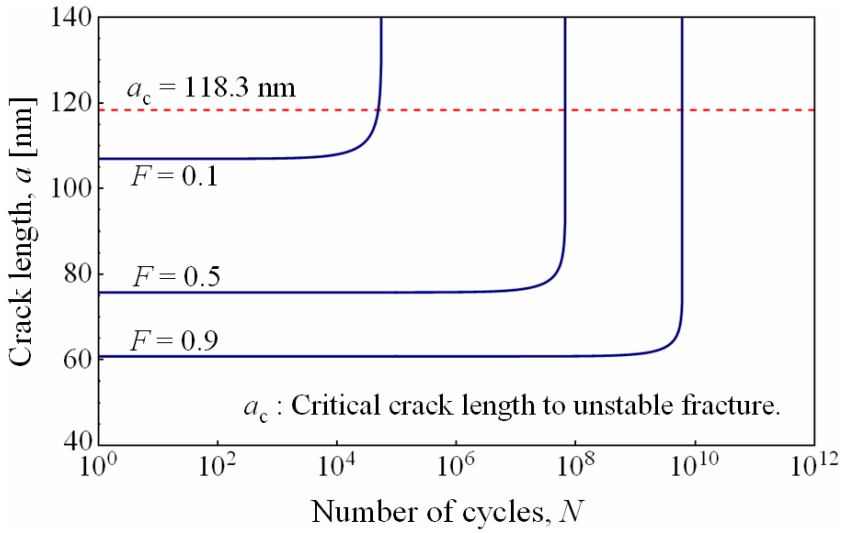


**Fig. A1.5** Crack extension versus fatigue lifetime with applied stress amplitude at 80% of average static strength.

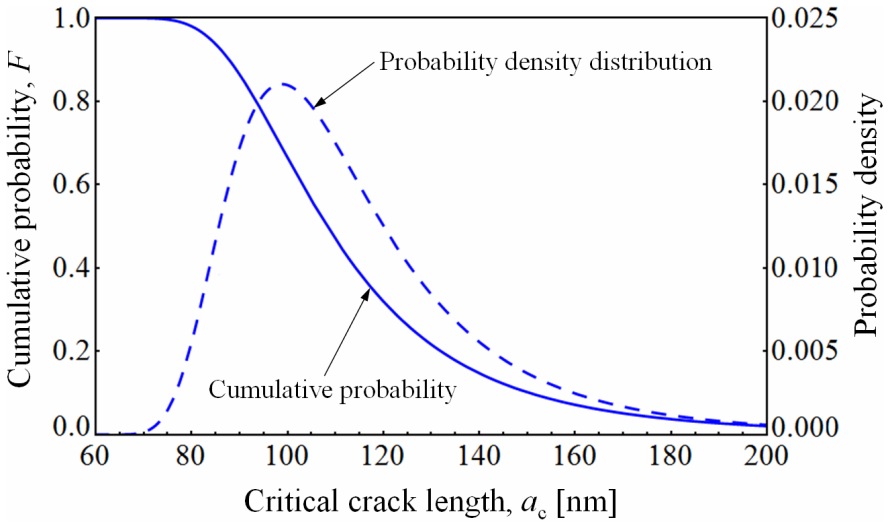


**Fig. A1.6** Critical crack length distribution of specimens broken at $10^7$ cycles.

region. The slow extension of the crack length in the certain number of cycles could be explained as the time needed to accumulate the damage induced by dislocations. When sufficient damage has been accumulated, the crack grows quickly to critical crack length. When the crack length extends beyond the critical crack length, unstable fracture occurs. The critical crack length $a_c$ was calculated with the stress amplitude range applied to the specimens of Type $C_{10}$ in the fatigue tests, i.e., from 2.39 GPa to 3.06 GPa, to be in a range from 81.6 nm to 133.8 nm. Besides that, since the

observation was performed on the specimens broken at $10^7$ cycles, critical crack length distribution for this case was also calculated as shown in Fig. A1.6. It shows that 90% of the critical cracks have lengths in a range from 83.9 nm to 170.7 nm. This range was in a good agreement with the measured critical length, i.e., from 100 nm to 180 nm. The traces of such large cracks found on the fracture surfaces are indeed far longer than the thickness of oxide layer, where the thickness of native oxide layer is usually known as thin as 2 nm or 3 nm. Even in the case of the thickness of thickened oxidation layer up to 50 nm [32], the crack lengths here are still far longer than the oxide thickness. It suggests that the fatigue crack process extended into the silicon itself.

## A1.5. Conclusion

The crack surfaces of the polysilicon thin film specimens with notches tested with monotonically increasing and cyclic loads were observed by SEM. By performing fractographic analysis, the initial cracks and the fatigue cracks extended to a critical length were speculated as the regions with different roughnesses on the crack surfaces. The fractography were supported by the initial crack length and critical crack length estimated with the optimum values of the parameters in Weibull distribution and Paris' law. The results suggest that the crack lengths were far longer than a reasonable oxide layer thickness, and therefore the fatigue cracks might extend into the silicon itself. They support the use of Paris' law for the theory of lifetime estimation in this thesis.

# Appendix 2

# EBIC Observation of Defect Growth Inside Silicon Under Fatigue Loading

## A2.1. Introduction

Fatigue mechanism of silicon is not yet clear enough and is just speculated from the results of fatigue tests without direct evidences. As introduced in Chapter I, although dislocations have not yet been observed directly during fatigue process, they could be a candidate to explain the fatigue mechanism of silicon. In order to support the theory on evaluation of fatigue lifetime estimated in this thesis, which was on the basis of Paris' law, electron beam induced current (EBIC) observation [113,114] is used to see whether the defects such as dislocations grow inside silicon under fatigue loading. EBIC measures the current generated by the electron beam through a junction potential near the surface. Therefore it was expected to figure out defects in silicon in terms of contrast change on its image. Since it is also expected [67] that compressive stress accumulates the damage more efficiently, the observation in this study is performed with single crystalline silicon specimen tested with cyclic compressive stress.

## A2.2. Specimen and experimental setup

Figure A2.1 shows the design of specimen used in EBIC observation experiment. It was designed with a small test section in the upper part as a horizontal beam which is supported at both the ends by the two vertical arms connected to the base plate in the lower part. Specimens were fabricated out of a n- type single crystal silicon wafer (thickness 380 μm, dopant Sb, conductivity 0.1 Ωcm) by applying a deep reactive ion etching (DRIE) process. The etched side surface has an inclination of 3 degrees, because of the characteristics of DRIE, which was mentioned in the previous chapters.

Boron was ion-implanted on the upper etched surface of the test section to compose a p+ layer, with the accelerating voltage of 5kV and dosage of $1.0\times10^{15}$ $cm^{-2}$. The junction underneath the p+ layer was utilized for the EBIC observation to explore the damage. For an ohmic contact to the n- type area, Au-0.5%Sb was deposited on the lower part of the specimen. The specimen was then annealed for 5 minutes in nitrogen at 900˚C for the activation of dopants. Finally, two notches with 15 μm tip radius were created with a dicing saw, which were tilted by +45 and -45 degrees to the surface.

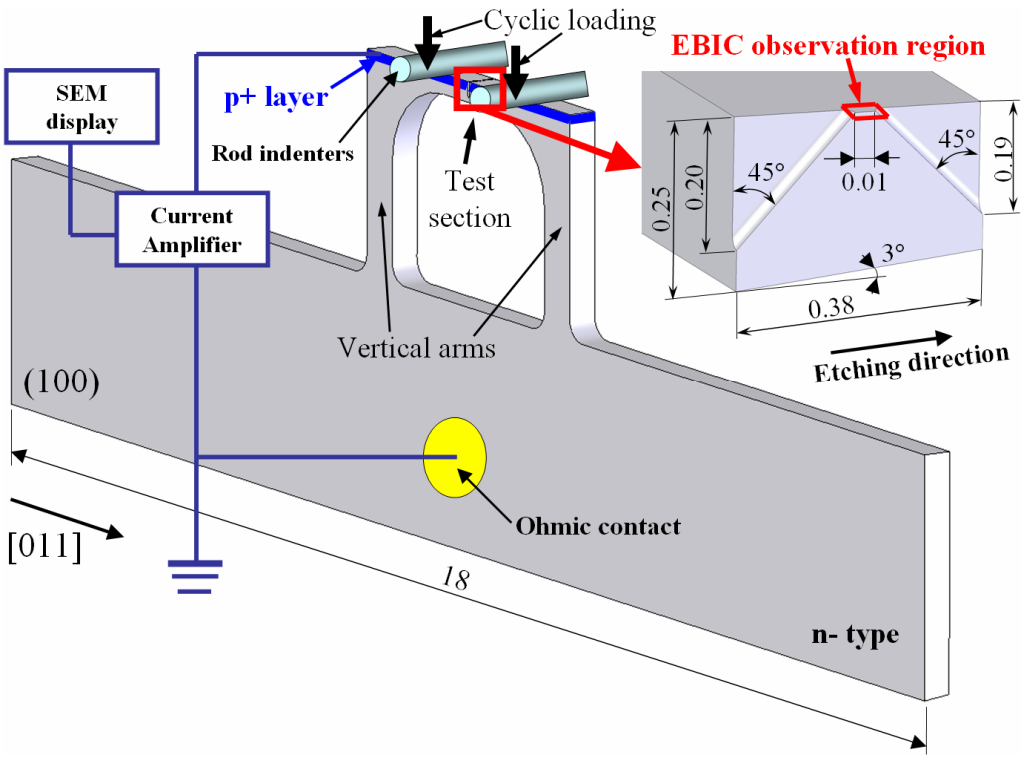


**Fig. A2.1** Specimen.

The experimental setup was designed as shown in Fig. A2.2. An environmental scanning electron microscope (ESEM) shown in Fig. A2.2(a) was used to perform EBIC observation. Specimen was kept by a state mounted on the holder inside the chamber of the ESEM as shown in Fig. A2.2(b). A piezo-positioner actuator (PI P-841.20, travel: 30 μm, resolution: 0.6 nm) was used to drive the setup. The applied load was measured by a load-cell LUR-A-100NSA1 manufactured by Kyowa Electronic Instruments Co., LTD. with a rated capacity 100 N. They were controlled by the equipments from outside of the chamber as shown in Fig. A2.2(a). The horizontal actuation given by the actuator was converted into the vertical stroke of loading rods via an elastic torsion spring indicated in Fig. A2.2(c). These rods pushed downward the upper surface of the test section at the two points indicated in Fig. A2.1 because of the inclination of the etched surface. The specimen was fixed to stand up vertically as shown in Fig. A2.2(d). By this way, the upper etched surface of the test section was facing to the electron beam while being subjected to a compressive stress.

The stress distribution on the EBIC observation region was analyzed by FEM. In design, maximum compressive stress on the EBIC observation region was 75.6 MPa when the load applied to the specimen was 1 N. The distance between the two

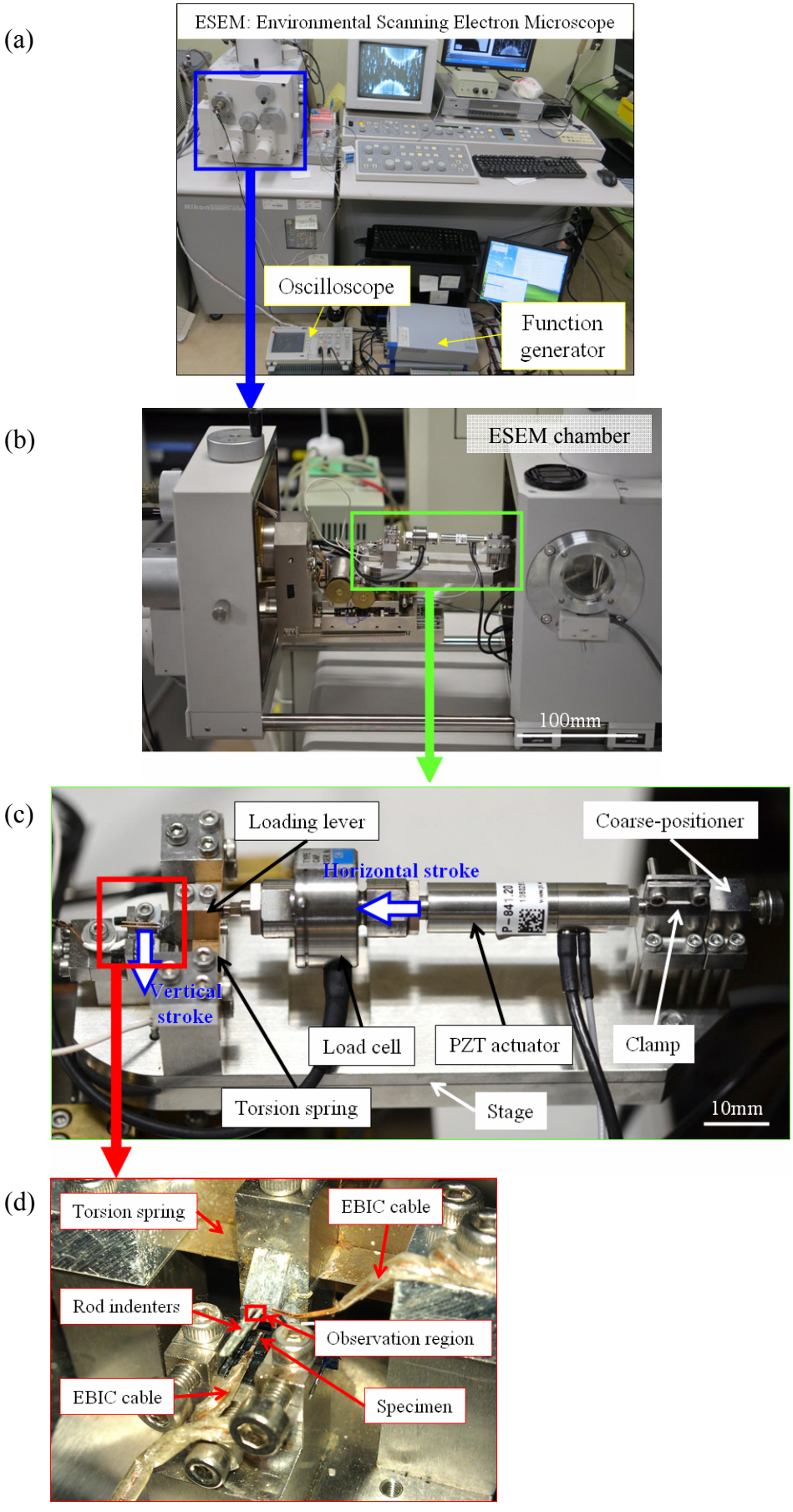


**Fig. A2.2** Experimental setup for fatigue test in ESEM.

notches was designed as 0.01 mm, but it was not able to be fabricated exactly. Therefore, FE analysis was performed individually for each specimen with the actual size of notches measured after creating the notches in order to obtain the exact value of the applied stress.

**A2.3. Results and discussion**

In this study, two specimens were tested by applying the cyclic loading with frequency of 50 Hz. The fatigue tests were occasionally interrupted to obtain EBIC images with an acceleration voltage of 30 kV.

For the first specimen (specimen #1), fatigue test was performed in the environment with gas pressure of 560 Pa. Its SEM picture before the fatigue tests is shown in Fig. A2.3(a). Firstly, the maximum compressive stress applied to the EBIC observation of the specimen was 0.62 GPa. EBIC pictures shown in Fig. A2.3(b) were taken during this test at gas pressure inside the ESEM chamber of 80 Pa. There was no noticeable change in the EBIC pictures from before the fatigue test (0 cycles) to after $5\times10^5$ cycles as shown in Fig. A2.3(b). By increasing the maximum compressive stress to 0.89 GPa, the EBIC pictures were obtained as shown in Fig. A2.3(c). These EBIC pictures were taken at gas pressure inside the ESEM chamber of 40 Pa. The change in the EBIC pictures was clearly observed. After these fatigue tests, the specimen was etched by using 10%HF solution in 10 minutes, whose etch rate against thermal oxide is estimated to be 23 nm/min [115]. Therefore it should remove all the silicon oxide layer, even if it would be so thick as 100 nm as presented in the other reports [29,33], locally exists at areas with stress concentration. If there would have been a locally grown silicon oxide layer on the surface to reduce EBIC, the image after HF treatment should have returned to the original image before fatigue loading. Figure A2.3(d) shows the SEM and EBIC pictures of this specimen after etching. There was no marked difference between the EBIC images before and after HF treatment. Therefore, the changes in EBIC images were not due to the growth of surface oxide layer but growth of defects inside silicon.

For the second specimen (specimen #2), fatigue test was performed in the environment with gas pressure of 40 Pa. The maximum compressive stress was 0.82 GPa. Its SEM and EBIC pictures were obtained as shown in Fig. A2.4. Gas pressure when taking those pictures was 40 Pa. The change in the EBIC pictures was also

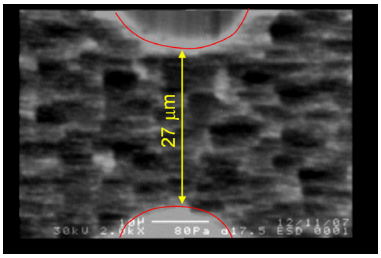


(a) SEM

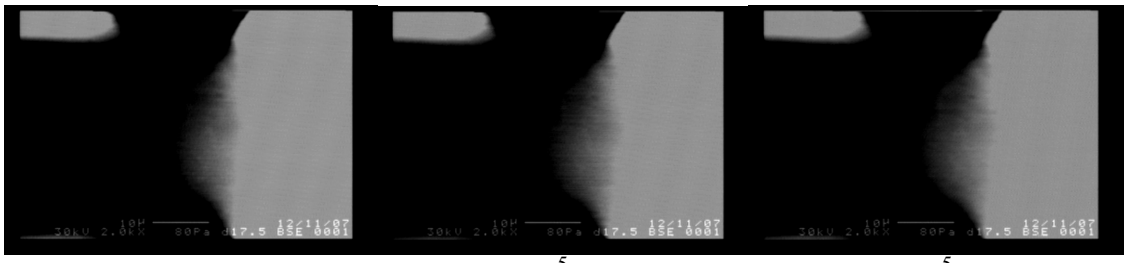

0 cycles $2\times10^5$ cycles $5\times10^5$ cycles

(b)

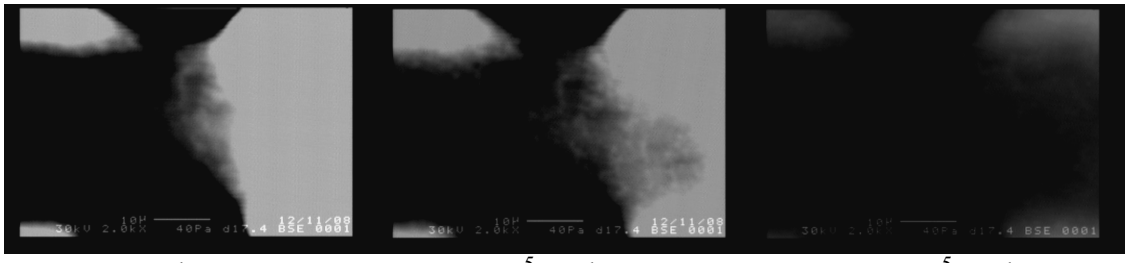

0 cycles $10^5$ cycles $2\times10^5$ cycles

(c)

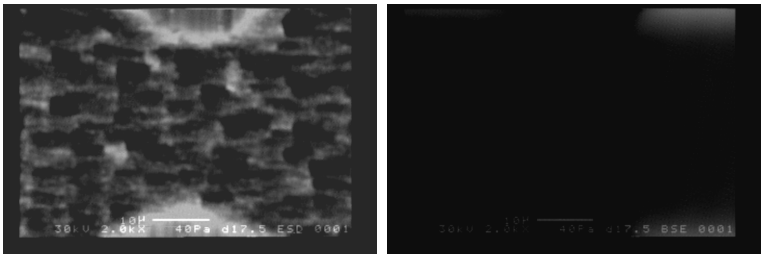

SEM EBIC

(d)

**Fig. A2.3** Observation results of Specimen #1 with (a) SEM picture before the test, (b,c) EBIC pictures the during fatigue loading process when the applied compressive stress was (b) 0.62 GPa and (c) 0.89 GPa, and (d) after HF treatment.

observed as the dark region gradually widening with the increment of number of cycles.

## A2.4. Conclusion

Direct images of damage growth process in silicon under cyclic compressive

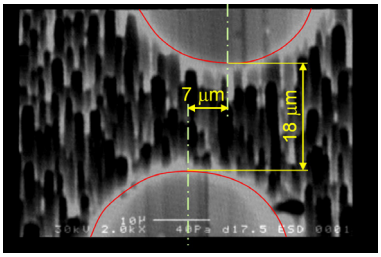


SEM

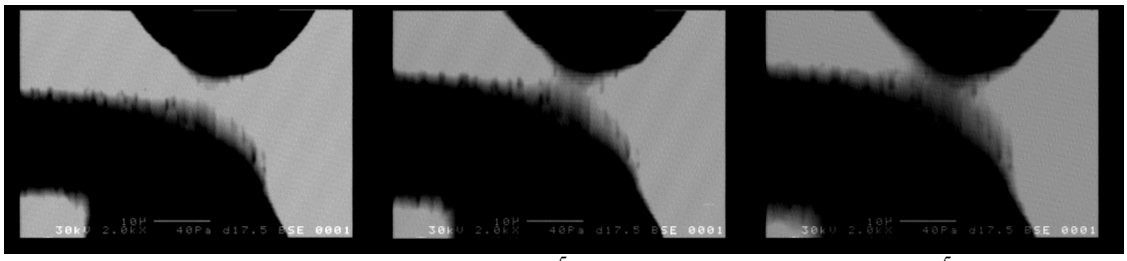

0 cycles $2\times10^5$ cycles $5\times10^5$ cycles

**Fig. A2.4** Observation results during fatigue loading process of Specimen #2 when the applied compressive stress was 0.82 GPa.

stress were successfully obtained with EBIC. The damage, which caused the local contrast changes at the notch tip in the specimen, was not the thickened surface oxide layer but the evolution of intrinsic defects being likely dislocations inside the crystal of silicon. Therefore, it supports the theory on evaluation of fatigue lifetime estimated in this thesis, which was on the basis of Paris' law.

# References

[1] F. Hiroyuki, Microactuators and Micromachines, *Proceedings of the IEEE*, Vol. 86 (1998) 1721-1732.

[2] M. J. Madou, *Fundamentals of Microfabrication - The Science of Miniaturization 2nd edn*, (2002), Boca Raton, FL: CRC Press

[3] Fonash, S.J., Plasma Processing Damage in Etching and Deposition, *IBM Journal of Research and Development*, Vol. 43 (1999), pp. 103-107.

[4] Chen, Q., Yao, D., Kim, C. and Carman, G. P., Investigating the Influence of Fabrication Process and Crystal Orientation on Shear Strength of Silicon Micro-Components, *Journal of Materials Science*, Vol. 56 (2000), pp. 5465-5474.

[5] T. Tsuchiya, O. Tabata, J. Sakata and Y. Taga, Specimen size effect on tensile strength of surface micromachined polycrystalline silicon thin films, *J. Microelectromech. Syst.*, Vol. 7 (1998) 106-113

[6] O. M. Jadaan, N. N. Nemeth, J. Bagdahn and W. N. Sharpe, Probabilistic Weibull behavior and mechanical properties of MEMS brittle materials, *J. Mater. Sci.*, Vol. 38 (2003) 4087–4113

[7] D. H. Alsem, O. N. Pierron, E. A. Stach, C. L. Muhlstein and R. O. Ritchie, Mechanisms for fatigue of micron-scale silicon structural films, *Advanced Engineering Materials*, Vol. 9 (2007) 15-30

[8] W. Weibull, A statistical distribution function of wide applicability, *J. Appl. Mech*. Vol. 18 (1951) 293-7

[9] J. Bagdahn, W. N. Sharpe and O. Jadaan, Fracture strength of polysilicon at stress concentrations, *J. Microelectromech. Syst.,* Vol. 12 (2003) 302–312

[10] A . McCarty and I. Chasiotis, Description of brittle failure of non-uniform MEMS geometries, *Thin Solid Films* Vol. 515 (2007) 3267–3276

[11] R. Boroch, J. Wiaranowski, R. Mueller-Fiedler, M. Ebert and J. Bagdahn, Characterization of strength properties of thin polycrystalline silicon films for MEMS applications, *Fatigue Fract. Eng. Mater. Struct.,* Vol. 30 (2007) 2–12

[12] N. N. Nemeth, L. J. Evans, O. M. Jadaan, W. N. Sharpe, G. Beheim and M. Trapp, Fabrication and probabilistic fracture strength prediction of high-aspect-ratio single crystal silicon carbide microspecimens with stress concentration, *Thin Solid Films,* Vol. 515 (2007) 3283–3290

[13] A. M. Fitzgerald, D. M. Pierce, B. M. Huigens and C. D. White, A general methodology to predict the reliability of single-crystal silicon MEMS devices, *J. Microelectromech. Syst.,* Vol. 18 (2009) 962-970

[14] J. A. Connally, S. B. Brown, Slow Crack Growth in Single-Crystal Silicon, *Science*, Vol. 256 (1992) 1537-1539.

[15] H. Kahn, R. Ballarini, R. L. Mullen, A. H. Heuer, Electrostatically actuated failure of microfabricated polysilicon fracture mechanics specimen, *Proc. R. Soc. Lond*. A, Vol. 455 (1999) 3807–23.

[16] C. L. Muhlstein, S. B. Brown, R. O. Ritchie, High-Cycle Fatigue of single-crystal silicon thin films, *J. Microelectromech. Syst.*, Vol. 10 (2001) 593-600.

[17] W. N. Sharpe Jr, J. Bagdahn, Fatigue Testing of Polysilicon - a Review, *Mech. Mater.*, Vol. 36 (2004) 3-11.

[18] F. Ericson and J. A. Schweitz, Micromechanical fracture strength of silicon, *J. Appl. Phys.*, Vol. 68 (1990) 5840-5844.

[19] C. J. Wilson, A. Ormeggi and M. Narbutovskih, Fracture testing of silicon microcantilever beams, *J. Appl. Phys.*, Vol. 79 (1996) 2386–2393.

[20] S. Greek, F. Ericson, S. Johansson, M. Furtsch and A. Rump, Mechanical characterization of thick polysilicon films Young's modulus and fracture strength evaluated with microstructures, *J. Micromech. Microeng.*, Vol. 9 (1999) 245–251.

[21] T. Yi, L. Li and C. J. Kim, Microscale material testing of single crystalline silicon: process effects on surface morphology and tensile strength, *Sens. Actuators A: Physical*, Vol. 83 (2000) 172-178.

[22] A. M. Fitzgerald, R. H. Dauskardt and T. W. Kenny, Fracture toughness and crack growth phenomena of plasma-etched single crystal silicon *Sens, Actuators A: Physical*, Vol. 83 (2000) 194-199

[23] H. Kahn, N. Tayebi, R. Ballarini, R. L. Mullen and A. H. Heuer, Fracture toughness of polysilicon MEMS devices, *Sens. Actuators A: Physical*, Vol. 82 (2000) 274-280

[24] S. Sundararajan and B. Bhushan, Development of AFM-based techniques to measure mechanical properties of nanoscale structure, *Sens. Actuators A: Physical*, Vol. 101 (2002) 338-351

[25] X. Li, T. Kasai, S. Nakao, H. Tanaka, T. Ando, M. Shikida and K. Sato, Measurement for fracture toughness of single crystal silicon film with tensile test, *Sens. Actuators A: Physical*, Vol. 119 (2005) 229-235

[26] S. Izumi, C. W. Ping, M. Yamaguchi, S. Sakai, A. Suzuki and Y. Ueda, Strength analysis of MEMS micromirror devices - Effects of loading mode and etching damage, *Key Engineering Materials*, Vol. 297-300 (2005) 527-532

[27] H. Kahn, L. Chen, R. Ballarini and A. H. Heuer, Mechanical fatigue of polysilicon: Effects of mean stress and stress amplitude, *Acta Materialia*, Vol. 54 (2006) 667-678.

[28] C. L. Muhlstein, S. B. Brown, R. O. Ritchie, High-cycle fatigue and durability of polycristalline silicon thin films in ambient air, *Sensors and Actuators* A, Vol. 94 (2001) 177-188.

[29] C.L. Muhlstein, E.A. Stach, R.O. Ritchie, A reaction-layer mechanism for the delayed failure of micron-scale polycrystalline silicon structural films subjected to high-cycle fatigue loading, *Acta Materialia*, Vol. 50 (2002) 3579–3595.

[30] G. Langfelder, A. Longoni, F. Zaraga, A. Corigliano, A. Ghisi, A. Merassi, A new on-chip test structure for real time fatigue analysis in polysilicon MEMS, *Microelectronics Reliability*, Vol. 49 (2009) 120–126.

[31] D. H. Alsem, C. L. Muhlstein, E. A. Stach and R. O. Ritchie, Further considerations on the high-cycle fatigue of micron-scale polycristalline silicon, *Scripta Materialia*, Vol. 59 (2008) 931-935.

[32] M. Budnitzki and O. N. Pierron, Highly localized surface oxide thickening on polycristalline silicon thin films during cyclic loading in humid environment, *Acta Materialia*, Vol. 57 (2009) 2944-2955.

[33] D. H. Alsem, R. Timmerman, B. L. Boyce, E. A. Stach, J. Th. M. De Hosson, R.

O. Ritchie, Very high-cycle fatigue failure in micron-scale polycrystalline silicon films: Effects of environment and surface oxide thickness, *Journal of Applied Physics*, Vol. 101 (2007) 013515.

[34] E. K. Baumert, P. O. Theillet and O. N. Pierron, Investigation of the low-cycle fatigue mechanism for micron-scale monocrystalline silicon films, *Acta Materialia*, Vol. 58 (2010) 2854-2863.

[35] J. Bagdahn and W. N. Sharpe Jr, Fatigue of polycrystalline silicon under long-term cyclic loading, *Sensors Actuators* A, Vol. 103 (2003) 9–15.

[36] P. O. Theillet, O. N. Pierron, Fatigue rates of monocrystalline silicon thin films in harsh environments: Influence of stress amplitude, relative humidity, and temperature, *Applied physics letters*, Vol. 94 (2009) 181915.

[37] H. Kahn, A. Avishai, R. Ballarini, and A. H. Heuer, Surface oxide effects on failure of polysilicon MEMS after cyclic and monotonic loading, *Scripta Materialia*, Vol. 59 (2008) 912-915.

[38] H. Kahn, R. Ballarini, J. J. Bellante, A. H. Heuer, Fatigue Failure in Polysilicon Not Due to Simple Stress Corrosion Cracking, *Science*, Vol. 298 (2002) 1215-1218.

[39] G. Langfelder, A. Longoni and F. Zaraga, Monitoring fatigue damage growth in polysilicon microstructures under different loading conditions, *Sensors and Actuators* A, Vol. 159 (2010) 233-240.

[40] H. Kahn, R. Ballarini, A.H. Heuer, Dynamic fatigue of silicon, *Current Opinion in Solid State and Materials Science*, Vol. 8 (2004) 71–76.

[41] A. G. Evans and E. R Fuller, Crack propagation in ceramic materials under cyclic loading conditions, *Metallurgical Transactions*, Vol. 5 (1974) 27-33.

[42] R. O. Ritchie, Mechanisms of fatigue-crack propagation in ductile and brittle solids, *International Journal of Fracture*, Vol. 100 (1999) 55–83.

[43] F. Seitz, The Plasticity of Silicon and Germanium, *Physical Review* 88 (1952) 722-724.

[44] C. J. Gallagher, Plastic Deformation of Germanium and Silicon, *Physical Review* 88 (1952) 721-722.

[45] M. Brede, P. Haasen, The brittle-to-ductile transition in doped silicon as a

model substance, *Acta Metallurgica*, vol. 36, 8 (1988) 2003−2018

[46] M. J. Hill and D. J. Rowcliffe, Deformation of Silicon at Low Temperatures, *Journal of Materials Science*, Vol. 9 (1974) 1569-1576

[47] C. Stjohn, Brittle-To-Ductile Transition in Pre-Cleaved Silicon Single-Crystals, *Philosophical Magazine*, Vol. 32 (1975) 1193-1212

[48] Y. H. Chiao and D. R. Clarke, Direct Observation of Dislocation Emission from Crack Tips in Silicon at High-Temperatures, *Acta Metallurgica*, Vol. 37 (1989) 203-219

[49] J. R. Rice, Dislocation Nucleation from a Crack Tip – An Analysis Based on the Peierls Concept, *Journal of the Mechanics and Physics of Solids*, Vol. 40 (1992) 239-271

[50] S. G. Roberts, A. S. Booth and P. B. Hirsch, Dislocation Activity and Brittle-Ductile Transitions in Single Crystals, *Materials Science And Engineering A-Structural Materials Properties Microstructure And Processing*, Vol. 176 (1993) 91-98

[51] A. George and G. Michot, Dislocation Loops at Crack Tips – Nucleation and Growth – An Experimental Study in Silicon, *Materials Science And Engineering A-Structural Materials Properties Microstructure And Processing*, Vol. 164 (1993) 118-134

[52] Y. B. Xin and K. J. Hsia, A Technique to Generate Straight Through Thickness Surface Cracks and Its Application to Studying Dislocation Nucleation in Si, *Acta Materialia*, Vol. 44 (1996) 845-853

[53] P. B. Hirsch and S. G. Roberts, Comment on the Brittle-To-Ductile Transition: A Cooperative Dislocation Generation Instability; Dislocation Dynamics and the Strain-rate Dependence of the Transition Temperature, *Acta Materialia*, Vol. 44 (1996) 2361-2371

[54] G. Xu, A. S. Argon and M. Ortiz, Critical Configurations for Dislocation Nucleation from Crack Tips, *Philosophical Magazine a-Physics of Condensed Matter Structure Defects and Mechanical Properties*, Vol. 75 (1997) 341-367

[55] K. Sumino, Deformation Behavior of Silicon, *Metallurgical and Materials Transactions A*, Vol. 30A (1999) 1465-1479

[56] A. S. Argon, Mechanics and physics of brittle to ductile transitions in fracture, *Journal of Engineering Materials and Technology-Transactions of the ASME*, Vol. 123 (2001) 1-11

[57] B. J. Gally and A. S. Argon, Brittle-to-ductile Transitions in the Fracture of Silicon Single Crystals by Dynamic Crack Arrest, *Philosophical Magazine a-Physics of Condensed Matter Structure Defects and Mechanical Properties*, Vol. 81 (2001) 699-740

[58] M. Tanaka, T. Fukui, T. Yamagata, T. Morikawa, K. Higashida and R. Onodera, TEM/AFM Observation of Crack Tip Plasticity in Silicon Single Crystals, *Materials Transactions*, Vol. 42 (2001) 1839-1842

[59] T. Namazu, Y. Isono, T. Tanaka, Plastic deformation of nanometric single crystal silicon wire in AFM bending test at intermediate tempereratures, *J. Microelectromech. Syst*., Vol. 11 (2002) 125-135.

[60] X. Han, K. Zheng, Y. Zhang, X. Zhang, Z. Zhang and Z. L. Wang, Low-Temperature in Situ Large-Strain Plasticity of Silicon Nanowires, *Advanced Materials*, Vol 19 (2007) 2112-2118

[61] F. Ostlund, K. R. Malyska, K. Leifer, L. M. Hale, Y. Tang, R. Ballarini, W. W. Gerberich, J. Michler, Brittle-to-Ductile Transition in Uniaxial Compression of Silicon Pillars at Room Temperature, *Microelectronics Reliability*, Vol. 19 (2009) 2439–2444.

[62] S. Yoneoka, Y. Qiao Qu, S. Wang, M. W. Messana, A. B. Graham, J. Salvia, B. Kim, R. Melamud, G. Bahl and T. W. Kenny, High-Cyclic Fatigue Experiments of Single Crystal Silicon in an Oxygen-Free Environment, *Proceedings of the IEEE 23rd International Conference on Micro Electro Mechanical Systems (MEMS)* (2010) 224-227.

[63] S. Nakao, T. Ando, M. Shikida, K. Sato, Effect of Temperature Toughness in a Single-Crystal-Silicon Film and Transition in its Fracture Mode, *Journal of Micromechanics and Microengineering*, Vol. 18 (2008) 015026

[64] S. Nakao, T. Ando, S. Arai, N. Saito, K. Sato, Variation in Dislocation Pattern Observed in SCS Films Fractured by Tensile Test: Effects of Film Thickness and Testing Temperature, *Proceedings of the MRS 2008,* Vol. 1052 (2008)

DD03-21

[65] T. Ando, T. Takumi, S. Nozue, K. Sato, Fracture Toughness of Si Thin Film at Very Low Temperatures by Tensile Test, *Proceedings of the IEEE 24th International Conference on Micro Electro Mechanical Systems (MEMS)* (2011) 436-439.

[66] J.D. Nowak, A.R. Beaber, O. Ugurlu, S. L. Girshick, W.W. Gerberich, Small size strength dependence on dislocation nucleation, *Scripta Materialia*, Vol. 62-11 (2010) 819–822.

[67] K. Shima, S. Izumi, S. Sakai, Reaction pathway analysis for dislocation nucleation from a sharp corner in silicon: Glide set versus shuffle set, *Journal of Applied Physics*, Vol. 108 (2010) 063504.

[68] S. Kamiya, Y. Ikeda, M. Ishikawa, H. Izumi, J. Gaspar, O. Paul, Finite fatigue lifetime of silicon under inert environment, *Proceedings of the IEEE 24th International Conference on Micro Electro Mechanical Systems (MEMS)* (2011) 432-435.

[69] N. I. Kato, A. Nishikawa, H. Saka, Dislocations in Si generated by fatigue at room temperature, *Materials Science in Semiconductor Processing*, Vol. 4 (2001) 113–115.

[70] P. Paris and F. Erdogan, A critical analysis of crack propagation laws, *Journal of Basic Engineering, Transactions of the American Society of Mechanical Engineers* (1963) 528-534.

[71] T. C. Lindley, C. E. Richards and R. O. Ritchie, Mechanics and mechanisms of fatigue crack growth in metals: a review, *Metallurgia and Metal Forming* (1976) 268-280.

[72] S. Suresh, *Fatigue of Materials 2nd edition* (1998) Cambridge University Press, Cambridge, England.

[73] S. Li, L. Sun, W. Jia, Z. Wang, The Paris law in metals and ceramics, *Journal of materials science letter*, Vol. 14 (1995) 1493-1495.

[74] Y. Yamaji, K. Sugano, O. Tabata, T. Tsuchiya, Tensile-mode fatigue tests and fatigue life predictions of single crystal silicon in humidity controlled environments, *Proc. 20th IEEE MEMS Conf.* (2007) 267-270.

[75] S. Kamiya, S. Amaki, T. Kawai, N. Honda, P. Ruther, J. Gaspar, O. Paul, Seamless interpretation of the strength and fatigue lifetime of polycritalline silicon thin films, *J. Micromech. Micoeng.*, Vol. 18 (2008) 095023.

[76] T. Kawai, S. Amaki, J. Gaspar, P. Ruther, O. Paul, S. Kamiya, Prediction of Fatigue Lifetime Based on Static Strength and Crack Extension Law, *Proceedings of the IEEE 21st International Conference on Micro Electro Mechanical Systems (MEMS)*. (2008) 431-434.

[77] S. S. Wilks, *Mathematical statistics*, Princeton University Press, Princeton, New Jersey, 1947.

[78] M. Kendall, A. Stuart, *The advanced theory of statistics*, Vol. 2 : Inference and relationship, Fourth edition, Charles Griffin & company limited, England, 1979.

[79] D. Cousineau, S. Brown and A. Heathcote, Fitting distributions using maximum likelihood : Methods and Packages, *Behavior Research, Methods, Instruments & Computer*, Vol. 36 (2004) 277-290.

[80] S. Kamiya, J. H. Kuypers, A. Trautmann, P. Ruther and O. Paul, Process temperature dependent mechanical properties of polysilicon measured using a novel tensile test structure, *J. Micorelectromech. Syst.*, Vol. 16 (2007) 202-12.

[81] T. Tsuchiya, Y. Yamaji, K. Sugano and O. Tabata, Tensile and Tensile-Mode Fatigue Testing of Microscale Specimens in Constant Humidity Environment, *Experimental Mechanics*, Vol. 50 (2010) 509–516.

[82] D. Broek, *Elementary Engineering Fracture Mechanics* (Dordrecht: Kluwer), 1986.

[83] Y. Kubodera, S. Izumi, S. Sakai, H. Miyajima, K. Murakami, T. Isokawa, Influence of distribution of etching damage on brittle strength of single crystal silicon, *The Society of Material Science Japan, Material*, Vol. 59-10 (2007) 920-925.

[84] R. W. Davidge, *Mechanical Behavior of Ceramics*, Cambridge: Cambridge University Press, 1979.

[85] A. B. El-Shabasy, J. J. Lewandowski, Effects of load ratio, *R*, and test temperature on fatigue crack growth of fully pearlitic eutectoid steel (fatigue crack growth of pearlitic steel), *International Journal of Fatigue*, Vol. 26

(2004) 305–309.

[86] T. Ikehara and T. Tsuchiya, High-cycle fatigue of micromachined single crystal silicon measured using a parallel fatigue test system, *IEICE Electron, Express*, Vol. 4 (2007) 288-93.

[87] F.R. Stonesifer, Effect of grain size and temperature on fatigue crack propagation in A533 B steel, *Engineering Fracture Mechanics*, Vol. 10 (1978) 305-314.

[88] Kovacova Monika, Reliability likelihood ratio confidence bounds, *Journal of Applied Mathematics*, Vol. 2, No. 2 (2009) 217-226.

[89] S. S. Wilks, The large-sample distribution of the likelihood ratio for testing composite hypotheses, *The annals of Mathematical Statistics*, Vol. 9, No. 1 (1938) 60-62.

[90] D. Cousineau, Fitting the three-parameter weibull distribution: review and evaluation of existing and new methods, *IEEE Dielectrics and Electrical Insulation Society*, Vol. 16 (2009) 281-288.

[91] I. Chasiotis, S. W. Cho, K. Jonnalagadda, Fracture Toughness and Subcritical Crack Growth in Polycrystalline Silicon, *Transactions of the ASME*, Vol. 73 (2006) 714-722.

[92] V. L. Huy, J. Gaspar, O. Paul and S. Kamiya, Statistical Characterization of Fatigue Lifetime of Polysilicon Thin Films, *Sensors and Actuators A: Physical*, Vol. 179 (2012) 251-262.

[93] O. N. Pierron and C. L. Muhlstein, The Critical Role of Environment in Fatigue Damage Accumulation in Deep-Reactive Ion-Etched Single-Crystal Silicon Structural Films, *Journal of Microelectromechanical Systems*, Vol. 15, No. 1 (2006) 111-119.

[94] S. Nakao, T. Ando, M. Shikida and K. Sata, Effect of Temperature on Fracture Toughness in a Single-Crystal-Silicon Film and Transition in its Fracture Mode, *Journal of Micromechanics and Microengineering*, Vol. 18 (2008) 015026.

[95] W. Weibull, *A Statistical Theory of The Strength of Materials*, Generalstabens Litografiska Anstalts Förlag, 1939.

[96] M. Ciavarella, L. Afferrante and E. Valenza, Effect of Interaction Between Collinear Cracks on the Strength Distribution of Brittle Materials, *Proceedings of the 11th International Conference on Fracture* (2005) 5827.

[97] S. Mantha, R. Thisted, J. Foss, J. E. Ellis and M. F. Roizen, A Proposal to Use Confidence Intervals for Visual Analog Scale Data for Pain Measurement to Determine Clinical Significance, *Anesth Analg*, Vol. 77 (1993) 1041-1047.

[98] D. J. Saville, Basic Statistics and the Inconsistency of Multiple Comparison Procedures, *Canadian Journal of Experimental Psychology*, Vol. 57, No. 3 (2003) 167-175.

[99] B. Dawson and R. G. Trapp, *Basic & Clinical Biostatistics*, The McGraw-Hill Companies, Inc., 2004.

[100] C. L. Muhlstein, E. A. Stach, R. O. Ritchie, Mechanism of fatigue in micron-scale films of polycrystalline silicon for microelectromechanical systems, *Applied Physics Letters*, Vol. 80 (2002) 1532-1534.

[101] S. Kamiya, Y. Ikeda, J. Gaspar, O. Paul, Effect of humidity and temperature on the fatigue behavior of polysilicon thin film, *Sensors and Actuators A: Physical*, Vol. 170 (2011) 187-195.

[102] V. L. Huy, S. Kamiya, J. Gaspar, O. Paul, Statistical Characterization of Fracture Strength and Fatigue Lifetime of Polysilicon Thin Films with Different Stress Concentration Fields, *Journal of Solid Mechanics and Materials Engineering*, Vol. 6, No. 11 (2012) 1013-1029.

[103] K. S. Chen, A. A. Ayon, X. Zhang and S. M. Spearing, Effect of Process Parameters on the Surface Morphology and Mechanical Performance of Silicon Structures After Deep Reactive Ion Etching (DRIE), *J. Microelectromech. Syst.*, Vol. 11 (2002) 264-275

[104] G. D. Quinn, W. N. Sharpe Jr, G. M. Beheim, N. N. Nemeth and O. Jadaan, Fracture Origins in Miniature Silicon Carbide Structures, *Key Engineering Materials*, Vol. 290 (2005) 62-69.

[105] J. Karttunen, J. Kiihamäki and S. Franssila, Loading effects in deep silicon etching, *Proceedings of SPIE 2000*, Vol. 4174 (2000) 90–97.

[106] S. Franssila, *Introduction to Microfabrication,* John Wiley & Sons, 2010.

[107] W. N. Sharpe Jr, G. M. Beheim, L. J. Evans, N. N. Nemeth and O. M. Jadaan, Fracture Strength of Single-Crystal Silicon Carbide Microspecimens at 24 °C and 1000 °C, *J. Microelectromech. Syst.*, Vol. 17 (2008) 244-254.

[108] X. Li, T. Kasai, S. Nakao, T. Ando, M. Shikida, K. Sato and H. Tanaka, Anisotropy in Fracture of Single Crystal Silicon Film Characterized under Uniaxial Tensile Condition, *Sens. Actuators A: Physical*, Vol. 117 (2005) 143-150.

[109] K. S. Chen, S. M. Spearing and N. N. Nemeth, Structural Design of a Silicon Micro-Turbo-Generator, *AIAA Journal*, Vol. 39 (2001) 720-728.

[110] A. G. Frodesen, O. Skjeggestad and H. Tofte, *Probability and Statistics in Particle Physics*, Universitetsforlaget, 1979.

[111] W. T. Eadie and F. James, *Statistical Methods in Experimental Physics*, World Scientific Publishing Co. Pte. Ltd., 2006.

[112] R. J. Parrington, Fractography of Metals and Plastics, *Practical Failure Analysis*, Vol. 25 (2002) 16-44.

[113] C. Parish,D. Batchelor, C. Progl and P. Russell, Tutorial: Electron Beam-Induced Current in the Scanning Electron Microscope, *Microscopy and Analysis*, Vol. 21 (2007) 11-13.

[114] M. Werner, C. Hagendorf, O. Breitenstein, F. Altmann and J. Bagdahn, High-Resolution Electron-Beam Induced Current Imaging of the p-n Junction in Crystalline Silicon on Glass (CSG) Solar Cells, *23rd European Photovoltaic Solar Energy Conference* (2008) 2217-2220.

[115] K. R. Williams, K. Gupta, Etch Rates for Micromachining Processing-Part II, *Journal of Micrelectromechanical Systems*, Vol. 12 (2010) 761-778.

# Acknowledgements

Firstly, I would like to express the deep gratitude to my supervisor, Prof. Shoji Kamiya. I would also like to express my sincere thanks to Prof. Oliver Paul and Dr. Joao Gaspar of University of Freiburg for their action to specimen processing and variable suggestions, and to Ministry of Education, Culture, Sports, Science and Technology of Japan for supporting my life during studying in Japan. Finally, I would like to appreciate all members of Kamiya laboratory, especially to the professor assistants Dr. Hayato Izumi, Dr. Nobuyuki Shishido, the secretary Matsuda Mai of Kamiya' laboratory, the technical staff Sugiyama Hiroko and the graduated master students Taku Kawai, Yusuke Ikeda, Kei Nagayoshi and Ryutaro Hirai, for their useful advice and kind assistance in my work.